



## 저작자표시-비영리-변경금지 2.0 대한민국

이용자는 아래의 조건을 따르는 경우에 한하여 자유롭게

- 이 저작물을 복제, 배포, 전송, 전시, 공연 및 방송할 수 있습니다.

다음과 같은 조건을 따라야 합니다:



저작자표시. 귀하는 원저작자를 표시하여야 합니다.



비영리. 귀하는 이 저작물을 영리 목적으로 이용할 수 없습니다.



변경금지. 귀하는 이 저작물을 개작, 변형 또는 가공할 수 없습니다.

- 귀하는, 이 저작물의 재이용이나 배포의 경우, 이 저작물에 적용된 이용허락조건을 명확하게 나타내어야 합니다.
- 저작권자로부터 별도의 허가를 받으면 이러한 조건들은 적용되지 않습니다.

저작권법에 따른 이용자의 권리는 위의 내용에 의하여 영향을 받지 않습니다.

이것은 [이용허락규약\(Legal Code\)](#)을 이해하기 쉽게 요약한 것입니다.

[Disclaimer](#)

**Ph.D. Dissertation of Engineering**

**Overturning and mixing at the salt  
tip under the effects of the several  
estuarine channel geometries**

다양한 하구 지형 영향에 따른 salt tip에서의  
역전과 혼합에 대한 연구

**February 2021**

The Graduate School of Seoul National University  
Department of Civil and Environmental Engineering  
Hydro-engineering Major

**Nguyen Ngoc Minh**

# **Overturning and mixing at the salt tip under the effects of the several estuarine channel geometries**

**Advisor: Professor Jin Hwan Hwang**

Submitting a Ph.D. Dissertation of Engineering

February 2021

The Graduate School of Seoul National University  
Department of Civil and Environmental Engineering  
Hydro-engineering Major

Nguyen Ngoc Minh

Confirming the Ph.D. Dissertation written by  
Nguyen Ngoc Minh

February 2021

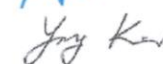
Chair Professor Yong Sung Park

Vice Chair Professor Jin Hwan Hwang

Examiner Professor Ho Kyung Ha

Examiner Professor Jungkyu Ahn

Examiner Professor Yong Hoon Kim



## **Abstract**

Density currents and high sediment concentration are frequently observed where the bottom slope or the contraction gradually changes. Until now, however, the behaviors of density currents and sediments due to the gradual change in topography have not been studied or discussed further. In contrast, it is found that in the coastal area where the slope changes rapidly, the flow at the density front is partially reversed as an overturn by the shoaling process of the internal tidal wave, and this causes significant vertical mixing and resuspension. Especially, such overturn can be seen as the hydraulic jump of the density current, as a result of the Froude number observed in the work of Masunaga et al. (2015). Therefore, the main goal of this study is to understand the topographical effects in estuary research, and in particular, to understand the process of the overturn induced by the hydraulic jump in translation. In this regard, a study is carried out on two topography types that are the mild bottom slope and the gradual contraction.

In this study, a numerical experiment is performed on the mixing process between salt water and fresh water in the mild bottom slope region or in the gradual contraction region. Results obtained from the numerical experiment are analyzed by means of the gradient Richardson number, the kinetic dissipation rate, etc., to clarify the stratification and sedimentary transport processes. Besides, by using the momentum fluxes method and

the Froude number method, we tried to understand in more detail the effects of the gradual change in topography on the generation of the hydraulic jump.

In conclusion, it can be seen that the overturn can occur and maintain for a long time at the salt tip where the bottom slope is gentle or the width is gradually contracted. Significant vertical mixing occurs at that location, and similarity resuspension occurs significantly. When the hydraulic jump occurs from the propagating processes of the tidal flows in the shear environment under the gradual effects of the topography, the overturn and internal bore may be generated.

**Keywords:** the overturn, the salt tip, mixing, the hydraulic jump, the mild bottom slope, the gradual contraction.

Student Number: 2016-30764

# TABLE OF CONTENTS

<b>CHAPTER ONE .....</b>	<b>1</b>
<b>I. INTRODUCTION.....</b>	<b>1</b>
<b>1.1 The background of the salt tip, the overturn and the effects of the geometry .....</b>	<b>1</b>
<i>1.1.1 Overview of the structure of the salt tip .....</i>	<i>1</i>
<i>1.1.2 Overview of the flow modes for two-layer flow.....</i>	<i>2</i>
<i>1.1.3 The effects of the geometry features .....</i>	<i>2</i>
<i>1.1.4 The existence of the overturn and its effects on the sedimentary transport processes.....</i>	<i>6</i>
<b>1.2 Literature review .....</b>	<b>10</b>
<i>1.2.1 Mixing and sedimentary processes under the effects of the bottom slope.....</i>	<i>10</i>
<i>1.2.2 The effects of the upstream contraction of the width.....</i>	<i>12</i>
<b>1.3 Objective.....</b>	<b>16</b>
<b>1.4 Outline of the Thesis .....</b>	<b>17</b>
<b>CHAPTER TWO .....</b>	<b>19</b>
<b>II. METHODOLOGY .....</b>	<b>19</b>
<b>2.1 The assessment tools .....</b>	<b>19</b>
<i>2.1.1 The high kinetic dissipation rate .....</i>	<i>19</i>
<i>2.1.2 The gradient Richardson number .....</i>	<i>20</i>
<i>2.1.3 The total sediment flux .....</i>	<i>21</i>
<i>2.1.4 The total momentum flux .....</i>	<i>23</i>

2.1.5 <i>The Froude numbers</i> .....	25
<b>2.2 Numerical experiment setups .....</b>	<b>26</b>
2.2.1 <i>The governing equation</i> .....	27
2.2.2 <i>Horizontal and vertical grid</i> .....	29
<b>CHAPTER THREE .....</b>	<b>30</b>
<b>III.    THE EXPERIMENTAL DOMAIN AND THE GRID</b>	
<b>CONVERGENCE.....</b>	<b>30</b>
<b>3.1 The experimental domain .....</b>	<b>30</b>
<b>3.2 The grid convergence investigation.....</b>	<b>34</b>
3.2.1 <i>The grid convergence method</i> .....	34
3.2.2 <i>The grid information and model set-up</i> .....	35
3.2.3 <i>The convergence of the grid</i> .....	39
3.2.4 <i>Summary</i> .....	41
<b>CHAPTER FOUR .....</b>	<b>42</b>
<b>IV.    THE EXISTENCE OF THE OVERTURNS ON THE</b>	
<b>MILD SLOPE AND THEIR EFFECTS .....</b>	<b>42</b>
<b>4.1 Introduction about the existence of the overturn .....</b>	<b>42</b>
<b>4.2 Model setup and data output.....</b>	<b>43</b>
<b>4.3 The structure of the flow and the sedimentary transport processes</b>	
<b>in the upstream of the estuary with the flat bottom and the constant</b>	
<b>width (non-geometry) .....</b>	<b>45</b>
4.3.1 <i>The structure of the salt tip in two flow modes</i> .....	45
4.3.2 <i>The suspended sedimentary processes</i> .....	50

<b>4.4 The existence of the overturn in exchange flow mode on the mild slope in 2D model.....</b>	<b>52</b>
<i>4.4.1 The salt tip structure and the existence of the exchange flow .....</i>	<i>52</i>
<i>4.4.2 The existence of the overturn and the internal tidal bore on the mild slope.....</i>	<i>55</i>
<b>4.5 The existence of the overturn in exchange flow mode on the mild slope in 3D model.....</b>	<b>63</b>
<i>4.5.1 The salt tip structure and the existence of the exchange flow .....</i>	<i>63</i>
<i>4.5.2 The existence of the overturn and the internal tidal bore .....</i>	<i>65</i>
<i>4.5.3 Mixing and sedimentary transport processes.....</i>	<i>71</i>
<b>4.6 Discussion and summary.....</b>	<b>80</b>
<b>CHAPTER FIVE .....</b>	<b>85</b>
<b>V. THE EXISTENCE OF THE OVERTURN IN THE GRADUAL CONTRACTION AND THE SEDIMENTARY TRANSPORT PROCESSES .....</b>	<b>85</b>
<b>5.1 Introduction .....</b>	<b>85</b>
<b>5.2 Model set-up and data analysis.....</b>	<b>86</b>
<b>5.3 The existence of the overturn and internal bore in the contraction region.....</b>	<b>87</b>
<b>5.4 The suspended sedimentary transport processes .....</b>	<b>93</b>
<b>5.5 Discussion and summary .....</b>	<b>95</b>
<b>CHAPTER SIX.....</b>	<b>98</b>
<b>VI. THE MECHANISM OCCURRING THE OVERTURN AS THE TERMS OF THE HYDRAULIC JUMP IN THE SALT TIP UNDER THE GRAGUAL EFFECTS OF THE GEOMETRY .....</b>	<b>98</b>



<b>6.1</b>	<b>Introduction .....</b>	<b>98</b>
<b>6.2</b>	<b>The effects of the geometry on the flow around the salt tip ..</b>	<b>101</b>
<b>6.3</b>	<b>The process for the development of the hydraulic jump in the salt tip.....</b>	<b>108</b>
	<i>6.3.1 The convergence of the energy under effects of the geometry and the fresh water.....</i>	<i>108</i>
	<i>6.3.2 The existence of the hydraulic jump at the front of the salt tip .</i>	<i>113</i>
<b>6.4</b>	<b>The existence of the overturns under the effects of the tide amplitude and the river discharge .....</b>	<b>119</b>
<b>6.5</b>	<b>Summary .....</b>	<b>122</b>
	<b>CHAPTER SEVEN .....</b>	<b>126</b>
<b>VII.</b>	<b>SUMMARY AND RECOMMENDATIONS.....</b>	<b>126</b>
<b>7.1</b>	<b>Summary .....</b>	<b>126</b>
<b>7.2</b>	<b>Recommendations .....</b>	<b>129</b>
	<b>References.....</b>	<b>130</b>
	<b>ABSTRACT IN KOREAN.....</b>	<b>143</b>
	<b>ACKNOWLEDGEMENT .....</b>	<b>145</b>

## LIST OF FIGURES

<b>Fig. I-1</b> The density structure in the salt tip region.....	1
<b>Fig. I-2</b> The side view structure of the two modes of the two-layer mechanism. (a) Uni-directional flow; (b) The exchange flow .....	2
<b>Fig. I-3</b> Definition sketch for the two-layer flows with the free surface under effects of the geometry. (a) Bottom slope effect. (b) The contraction of the width effect.....	3
<b>Fig. I-4</b> An example for the two-layer flow through the geometry. (a) Side view of the uni-directional flow over the sill (Staalstrøm et al., 2014); (b) Plan view and side view for the two-layer exchange flow through a constriction (Armi and Farmer, 1986).....	4
<b>Fig. I-5</b> An sketch of the density current head as the two-layer hydraulic jump (Baines, 1995). .....	5
<b>Fig. I-6</b> The shoaling process of the internal tide on bottom slope in the Otsuchi Bay leading to the development of the internal bore shown (Masunaga et al. 2015). .....	7
<b>Fig. I-7</b> The comparisons in the bottom slope, salinity and sediment concentration between the salt tip region in the upstream of the Chesapeake Bay near the slack before from Kim et al., (2007). .....	8
<b>Fig. I-8</b> The sediment flux with the overturn at the salt tip in Geyer (1993) ...	9
<b>Fig. I-9</b> Plan view and side view of salinity concentration (psu), currents and the Composite Froude number $G$ around the constriction at 54 km distance in Hudson river. (a) The plan view of the salinity concentration and with the currents near the end of the ebb phase. (b) The side view of contours of the flow magnitude. (c) The side view of the salinity concentration and Composite Froude number $G$ .....	14
<b>Fig. I-10</b> The summary of literature review and the reasons for research. ....	15

<b>Fig. I-11</b> Thesis overview .....	18
<b>Fig. II-1</b> Diagram of the vertical structure for the salt tip zone in the present work. ....	24
<b>Fig. II-2</b> An example of the grid cell used in SUNTANS (Fringer et al., 2006) .....	29
<b>Fig. III-1</b> The sketch of the geomorphological conditions in three experiments. (a) The constant width and without the bottom slope; (b) The mild bottom slope for 2D model; (c) The mild bottom slope for 3D model; (d) Upstream contraction of the width. ....	32
<b>Fig. III-2</b> Salinity concentration measured in Kim et al., (2007) and initial salinity concentration in model runs (psu). (a) in Kim et al., (2007); (b) in the model runs.....	33
<b>Fig. III-3</b> The structure of the meshes used for grid convergence investigation. (a) The grid structure for $G_1$ ( $\Delta x = 100$ m); (b) The grid structure for $G_3$ ( $\Delta x = 60$ m); (c) The grid structure for $G_5$ ( $\Delta x = 30$ m); (d) The grid structure for $G_7$ ( $\Delta x = 10$ m). ....	37
<b>Fig. III-4</b> The illustration for the method of calculating the scalar value of $f_i^t$ (equation (3.5)). (a) For $G_1$ ( $\Delta x = 100$ m); (b) For $G_3$ ( $\Delta x = 60$ m). Red point indicates the location of the observation point $i^{th}$ . Red line shows the edge of the mesh 1 ( $G_1$ ) and blue line shows the edges of the mesh 3 ( $G_3$ ).....	38
<b>Fig. III-5</b> The number of the cells vs $RMSE_l$ for four vertical locations. (a) at 1.0 m distance from the bottom; (b) at 4.0 m distance from the bed; (c) at 8.0 m distance from the bed; (d) at 12.0 m distance from the bed. ....	39
<b>Fig. III-6</b> The number of the cells vs $E_l$ for four vertical locations. (a) at 1.0 m distance from the bottom; (b) at 4.0 m distance from the bed; (c) at 8.0 m distance from the bed; (d) at 12.0 m distance from the bed. ....	40
<b>Fig. III-7</b> The number of the cells vs $\ln(E_l)$ for four vertical locations. (a) at 1.0 m distance from the bottom; (b) at 4.0 m distance from the bed; (c) at 8.0 m distance from the bed; (d) at 12.0 m distance from the bed. ....	41

**Fig. IV-1** The tidally averaged sediment concentration, the streamwise salinity density gradient, the vertical distribution of the streamwise flow at the salt tip, gradient Richardson number for salt layer and the flow modes from the profile of the velocity magnitudes near surface and near bottom for case 1 (Non-geometry case). (a) The tidally averaged sediment concentration near the bed ( $\text{kg/m}^3$ ) for a 70 km distance from the upstream to the downstream. (b) The salinity density gradient ( $\text{psu/km}$ ) near the bed around the salt head, (c) The vertical profiles of  $u$ -velocity ( $\text{cm/s}$ ) at locations of the salt head, (d) the gradient Richardson number for salt layer, (e) the flow modes from the files of the velocities near surface and near bottom ( $\text{cm/s}$ ). The black dotted line in (d) shows the location of the flow interface.....46

**Fig. IV-2** The distribution of the two velocity components ( $u$ ,  $w$ ) and the salinity concentration in the 10 km longitudinal cross-section of the salt tip at time ( $N_1$ ), ( $N_2$ ), ( $N_3$ ) in experiment 1 (Case 1) (Non-geometry effect). The small black dotted line is the contour of 0.005 psu salinity, separating domain into two zones, the left side is freshwater zone, the right size is saltwater zone. Yellow areas show the exchange mode. ....49

**Fig. IV-3** The suspended concentration ( $C$ ) with the sediment flux vectors in a 1.0 km longitudinal cross-section of the salt tip for case 1 at time ( $N_1$ ) – ( $N_3$ ). The small black dotted line is the contour of 0.005 psu salinity, separating domain into two zones, the left side is freshwater zone, the right size is saltwater zone. The small blue dotted line show the locations of the interfacial flow layers. Time ( $N_1$ ), time ( $N_2$ ) and time ( $N_3$ ) are depicted in Fig. IV-1(e).....51

**Fig. IV-4** The tidally averaged sediment concentration, the streamwise salinity density gradient, the vertical distribution of the streamwise flow at the salt tip, gradient Richardson number for salt layer and the flow modes from the profile of the velocity magnitudes near surface and near bottom for case 2 (the bottom slope, 2D model).(a) The tidally averaged sediment concentration near the bed ( $\text{kg/m}^3$ ) for a 70 km distance from the upstream to the downstream. (b) The salinity density gradient ( $\text{psu/km}$ ) near the bed around the salt head, (c) The vertical profiles of  $u$ -velocity ( $\text{cm/s}$ ) at locations of the salt head, (d) the gradient

Richardson number for salt layer, (e) the flow modes from the file of the velocity near surface and near bottom (cm/s). The black dotted line in (d) shows the location of the flow interface. ....53

**Fig. IV-5** Distributions of the three velocity components, the distributions of the salinity concentration for the case 2 (2D model) in experiment 1 at time ( $S_1$ ), ( $S_2$ ), ( $S_3$ ) and ( $S_4$ ). Streamwise velocity ( $u$ ), vertical velocity ( $w$ ), salinity concentration ( $s$ ) in the 1.5 km longitudinal cross-section of the salt tip. The small black dotted line is the contour of 0.005 psu salinity, separating the domain into two zones, the left side of the salt tip is the freshwater zone, the other side is the saltwater zone. ....58

**Fig. IV-6** The sediment concentration, salt tip structure at time ( $S_3$ ) in 100 m distance for case 2 and the structure of the internal bore on the coastal region. (a) Distribution of sediment concentration ( $\text{kg/m}^3$ ); (b) the longitudinal current distribution (cm/s); (c) the vertical current (cm/s); (d) the salinity distribution around the salt tip and (e) the structure of the salt tip with an overturn. (g) and (h) the internal bore and vortex core on the coastal region in Masunaga et al., (2015). ....61

**Fig. IV-7** The profile of the streamwise velocity at the salt tip near the free surface and near the bottom boundary and the vertical distribution of the gradient Richardson number for salt layer in case 2 (the bottom slope, 3D model). (a) The vertical profiles of  $u$ -velocity (cm/s) at locations of the salt head, (d) the gradient Richardson number for salt layer. The black dotted line in (b) shows the location of the flow interface. ....64

**Fig. IV-8** Distributions of the three velocity components as well as distribution of the salinity concentration for the case 3 in experiment 2 (3D model) at time ( $T_1$ ), ( $T_2$ ), ( $T_3$ ). Streamwise velocity ( $u$ ), vertical velocity ( $w$ ), salinity concentration ( $s$ ) in the 1.5 km longitudinal cross-section of the salt tip and the lateral velocity vectors ( $v \times w$ ) in 500 m transverse cross-section at the salt head (second column). The small black dotted line is the contour of 0.005 psu salinity, separating the domain into two zones, the left side of the salt tip is the freshwater zone, the other side is the saltwater zone. The grey dashed line shows the

pycnocline layer. The vertical dotted blue line shows the location for the lateral cross section. ....66

**Fig. IV-9** Kinetic dissipation rate ( $\epsilon$ ), Richardson number (Ri) number and suspended concentration (C) in a 1.0 km longitudinal cross-section of the salt tip for two flow modes in two tidal phase for case 3 (3D). (a)-(c): dissipation rate ( $\log_{10}(\epsilon)$ ), (d)-(f): the Richardson number (Ri), (g)-(h): the suspended concentration (C) with the sediment flux vector. The results in uni-directional mode for ebb and flood is represented by the results at time ( $T_1$ ) and ( $T_4$ ), respectively. The results in the exchange flow mode is represented by the results at time ( $T_2$ ). The small black dotted line is the contour of 0.005 psu salinity, separating domain into two zones, the left side is freshwater zone, the right size is saltwater zone. The white color in the freshwater show for the case density is homogenous in the vertical direction. The small blue dotted line show the locations of the interfacial layer between two flow layers. ....73

**Fig. IV-10** The time series of the total sediment concentration, the integral sediment advection flux and the sediment pumping flux through the water column in the streamwise direction and lateral direction and the total sediment flux over a the tidal cycle for case 3. (a) The averaged of the depth integral sediment concentration ( $C_m$ ) in the short distance from the salt tip to downstream (about 250 m distance around the head). (b) The integral sediment advection flux (Advection<sub>x</sub>) and the integral sediment pumping flux (Pumping<sub>x</sub>) through the water column in the longitudinal direction. (c) The width averaged of the integral the sediment advection fluxes (Advection<sub>y</sub>) and sediment pumping flux (Pumping<sub>y</sub>) through the water column in lateral direction. Positive value show sediment is transport to wallward, negative value show the sediment is transport to *thalweg*. (d) The total sediment flux through the water column in both two directions lateral and streamwise directions ( $SF_x + SF_y$ ). Time (F) is the time the sediment concentration in (a) is greatest. Dotted red line show the time the concentration is greatest ( $t/T = 2.94$ ). Yellow aground show the periods of exchange flow mode found from Fig. V-4(a). ....77

**Fig. IV-11** The linear correlation between the sediment concentration and total sediment flux, the vertical turbulent diffusive flux for case 3 (3D model) for the period of slack before flood and period of flood. (a) The linear correlation between the depth integral sediment concentration ( $C_m$ ) and total sediment flux ( $SF_x + SF_y$ ), (b) The correlation between the sediment concentration ( $C_m$ ) and the vertical turbulent diffusive flux ( $C'w'$ ). .....79

**Fig. IV-12** The observation and simulation results of the sediment concentration and salinity around the salt tip the upstream of the Chesapeake Bay estuary in North et al., (2004), North & House, (2001), Sanford et al., (2001). (a) Salinity and TSS on Feb. 01 1996 observed by Sanford et al., (2001). (b) The observation results (upper figure) on May 08, 2001 which used to be compared to the computational region (lower figure) on day 352.38 on North et al., (2004). (c) The observation results in May 4-5 and 12-13 in North & House, (2001). .82

**Fig. IV-13** Schematic image of the changes of the salt head regime over a tidal cycle on the mild slope. (a) At the full ebb (the uni-directional mode for ebb), (b) At the slack before flood (in the exchange mode), (c) At the full flood (the uni-directional mode for flood) and (d) At the slack after flood (in the exchange mode). .....84

**Fig. V-1** The upstream contraction mesh used for case 4 .....86

**Fig. V-2** The profile of the streamwise-velocity near the free surface and near the bottom boundary at the salt tip, the horizontal distribution of the sediment concentration and the velocity vectors ( $u \times v$ ) from 2.0 m distance from bottom at time ( $C_1$ ) and ( $C_2$ ) for case 4 (the contraction case). (a) The profile of the streamwise velocity near the free surface and near the bottom boundary at the salt tip used to determine the exchange flow mode and uni-directional mode. (b), (c) The top view of the sediment concentration and horizontal current in 1.0 km distance around the salt tip at time ( $C_1$ ) and ( $C_2$ ). In (a), the  $u < 0$ : flood and  $u > 0$ : ebb. In (b), (c), the small white dotted line is the contour of 0.005 psu salinity as the location of the salt tip, separating the domain into two zones, the left side

of the salt tip is the freshwater zone, the other side is the saltwater zone. Yellow background in (a) show the periods of the exchange mode. ....89

**Fig. V-3** Distribution of the two velocity components and distribution of the salinity concentration. Streamwise velocity ( $u$ ), vertical velocity ( $w$ ), salinity concentration ( $s$ ) in the 1.0 km longitudinal cross-section of the salt tip for the case in experiment 2(a) (Case 3) (the contraction case) at time ( $C_1$ ) and time ( $C_2$ ). The small black dotted line is the contour of 0.005 psu salinity, separating the domain into two zones, the left side of the figure is the freshwater zone, the other side is the saltwater zone. Time ( $C_1$ ) and ( $C_2$ ) are depicted in Fig. V-2(a).....91

**Fig. V-4** The structure of the salt tip with an overturn for the contraction case (case 3) at time ( $C_1$ ). Time ( $C_1$ ) is depicted in Fig. VI-2(a) .....92

**Fig. V-5** The suspended concentration ( $C$ ) with the sediment flux vectors in a 1.0 km longitudinal cross-section of the salt tip for case 4 (Contraction case). The small black dotted line is the contour of 0.005 psu salinity, separating domain into two zones, the left side is freshwater zone, the right size is saltwater zone. The small blue dotted line show the locations of the interfacial flow layers. Time ( $C_1$ ) and time ( $C_2$ ) are depicted in Fig. V-2(a). ....94

**Fig. V-6** Schematic image of the variations of the salt head regime through the tidal cycle in the contraction case. (a) During ebb (uni-directional mode), (b) During flood (exchange flow mode). ....97

**Fig. VI-1** The summarize of the time for the existence of the exchange flow in the salt tip over a tidal cycle for three study cases (case 1, case 3 and case 4). ....102

**Fig. VI-2** The variations of the tidally averaged of the momentum flux for fresh layer ( $MF_1$ ) and for salt layer ( $MF_2$ ) through whole lateral cross section in 70 km distance around salt tip for three study cases. The formula computed  $MF_1$  and  $MF_2$  are presented in equation (6.1) and (6.2).....103

**Fig. VI-3** The variations of the pressure momentum flux and kinetic momentum flux for salt layer in a 4.0 km distance around salt tip over three study cases (case 1, case 3 and case 4). Two component of the momentum fluxes is



computed based on the equation (2.9) in section 2.1. Time ( $N_1$ ), ( $N_2$ ) and ( $N_3$ ) are depicted in Fig. IV-1(e). Time ( $T_2$ ), ( $T_4$ ) and ( $T_5$ ) are depicted in Fig. IV-8(a). Time ( $C_1$ ) and ( $C_2$ ) are depicted in Fig. V-2(a)..... 110

**Fig. VI-4** The internal Froude number of the freshwater layer ( $Fr^{2_1}$ ) and saltwater layer ( $Fr^{2_2}$ ) and the composite Froude number ( $G^2$ ) in the 3.0 km section around the salt tip for case 1 (the bottom slope for 2D model). Time ( $S_3$ ), time ( $S_5$ ) and time ( $S_7$ ) are depicted in Fig. IV-4(e). ..... 115

**Fig. VI-5** The variations of the Froude numbers at the salt tip for 2.5 tidal cycles for case 2 (the bottom slope for 2D model). (a) The maximum of the internal Froude number for the freshwater region ( $Fr^{2_1}$ ) and saltwater region ( $Fr^{2_2}$ ) and  $G^2$  around the salt tip. (b) The Froude number of the front ( $Fr_f$ ). Time ( $S_3$ ), time ( $S_5$ ) and time ( $S_7$ ) are depicted in Fig. V-1(e). Yellow area show the exchange flow mode depicted in Fig. V-1(e). ..... 117

**Fig. VI-6** The variations of the front Froude number ( $Fr_f$ ) of the salt front over 2.5 tidal cycles for three study cases: case 1 (non-bottom slope and contraction), case 3 (bottom slope case, 3D), case 4 (contraction case, 3D) and Yellow area show the exchange mode. .... 118

**Fig. VI-7** The total presence time for the existence of the exchange flow in the each slack or in the flood (experiment 4). (a) For the case with the river boundary current  $u_0 = 0.1$  m/s. (b) For the case with the tidal boundary amplitude  $\eta_0 = 0.5$  m/s. Red circle show for the overturn doesn't exist during this period..... 120

**Fig. VI-8** The sketch of effects of the contraction and bottom slope as well as the process for development of the overturn as a hydraulic jump in translation..... 124

## LIST OF TABLES

Table 1 The mesh information.....	36
Table 2 The study cases for the effects of the bottom slope investigation .....	43
Table 3 The statistics table of the information about four study cases for investigate the development of the hydraulic jump used in chapter VI .....	99
Table 4 The information about the thirty scenarios used for investigating the dependence of the presence time for the exchange flow on the tidal amplitudes and the river inflow rate (experiment 4).....	101

## LIST OF SYMBOLS

### Latin uppercase

$Fr$	The Froude number
$G^2$	The composite Froude number
$Ri$	Richardson number
$B_l$	A constant value at 16.6
$SF_x$	Total depth integrated sediment fluxes (the x-direction)
$SF_y$	Total depth integrated sediment fluxes (the y-direction)
$SF$	$SF = SF_x + SF_y$
$C$	Concentration of suspended sediment
$Mf$	Total momentum flux across a plane
$Mf_1$	Total momentum flux of the fresh water layer
$Mf_2$	Total momentum flux of the salt water layer
$Mf_{ip}$	The a pressure components of the momentum flux for fresh and salt layers
$Fr_1^2$	The internal Froude number for layer 1 (fresh layer)
$Fr_2^2$	The internal Froude number for layer 2 (fresh layer)
$H$	The coordination of the water depth
$W$	The width of the estuary
$D$	The water depth
$T$	The temperature
$K_H, K_V$	The horizontal and vertical mass diffusion coefficients of sediment
$W_s$	The settling velocity of sediment
$U$	The horizontal velocity on the cell faces

$C_d$	The bottom roughness
$G_1, G_2, \dots G_7$	Grid normalized ( $G_i$ )
$N$	The numbers of vertical layers
$R^2$	The linear correlation coefficient
$C_m$	The depth integral sediment concentration
$V$	The averaged of the velocity in the channel
$E$	The energy elevation grade line
$D_1$	The thickness of the upper layer (layer 1)
$E_1$	The energy of the upper layer (fresh water layer)
$D_2$	The thickness of the lower layer (layer 2)
$E_2$	The energy of the lower layer (salt layer)

### **Latin lowercase**

$q$	The turbulent velocity scale
$l$	The turbulent length scale
$u$	The streamwise velocity
$v$	The lateral velocity
$u_1$	The streamwise velocity in fresh water layers
$u_2$	The streamwise velocity in salt water layers
$p_1$	The pressure at fresh water layers
$p_2$	The pressure at salt water layers
$p_n$	The nonhydrostatic pressure component
$p_s$	The pressures of the free surface
$r$	The pressures of the baroclinic profile
$h_1$	The thicknesses of the fresh and salt layers

$h_2$	The thicknesses of the salt layers
$u_f$	Speed of flow at the front
$c$	Propogation speed of the front
$g'$	The reduced gravitaiotnal acceleration
$u(x,y,z,t)$	The Cartesian components of the averaged velocities in $x$ direction
$v(x,y,z,t)$	The Cartesian components of the averaged velocities in $y$ direction
$w(x,y,z,t)$	The Cartesian components of the averaged velocities in $z$ direction
$f, b$	The sine of the latitude Coriolis term and the cosine of the latitude Coriolis term
$s$	The salinity concentration
$k_H, k_V$	The horizontal and vertical mass diffusion coefficients of the salinity
$z_b$	The bottom elevation
$u_0$	The constant freshwater runoff at the upstream boundary
$\bar{u}$	The depth-averaged value of $u$
$c'w'$	The vertical turbulent diffusive flux
$d_{charac}$	The characteristic dimension
$f_1, f_2, f_3, f_4$	The coefficient terms of the energy lost
$s_1, s_2, s_3, s_4$	The scalar values of the triangles in $G_1$
$a_1, a_2, a_3, a_4$	The area of a triangle covering the location $i^{th}$ for mesh $G_1$
$a_0$	The areas of the triangle overlapped

## **Greek Symbols**

$\varepsilon$	The kinetic energy dissipation rate
$\rho_1$	The averaged density for fresh water layer
$\rho_2$	The averaged density for salt water layer
$\eta_1$	The vertical displacement of the fresh layer
$\eta_2$	The vertical displacement of the salt layer
$\eta$	The coordination of water surface
$\bar{\rho}$	The averaged density between two layers
$\rho$	The averaged density
$\rho_0$	The constant reference density
$\omega$	The Earth's angular velocity
$\phi$	The latitude
$\nabla_H$	The horizontal Laplacian
$\nu_H, \nu_V$	The horizontal and the eddy viscosities in vertical direction,
$\omega$	The mesh order convergence
$\eta_0$	The average amplitude of the tidal wave at the downstream boundary
$\Delta x$	The grid size
$\lambda$	The parameter as the product of $\Delta x/D_1$

### **Acronyms, Subscript or Superscript**

ETM	The estuarine turbidity maximum
Advection <sub>x</sub>	Depth integrated streamwise advection sediment flux in the streamwise direction ( <i>x</i> -direction).
Advection <sub>y</sub>	Depth integrated streamwise advection sediment flux in the streamwise direction ( <i>y</i> -direction).
Pumping <sub>x</sub>	Depth integrated streamwise tidal pumping flux in the streamwise direction ( <i>x</i> -direction).
Pumping <sub>y</sub>	Depth integrated streamwise tidal pumping flux in the streamwise direction ( <i>y</i> -direction).
<i>thalweg</i>	The deepest channel
SUNTANS	Stanford Unstructured Nonhydrostatic Terrain-Following Adaptive Navier-Stokes Simulator
<i>RMSE</i>	Root Mean Squared Error
<i>RSD</i>	The relative standard deviation of streamwise velocity fluctuations

# CHAPTER ONE

## I. INTRODUCTION

### 1.1 The background of the salt tip, the overturn and the effects of the geometry

#### 1.1.1 Overview of the structure of the salt tip

Estuaries are the connecting regions between the rivers and the ocean. The interactions between the salt-water flows from the ocean and the fresh-water flows from the river lead to the flows of the estuaries frequently be in the strong stratification regime. The stratified layer ends at the upstream of the estuary in the salt tip region (Fig. I-1). From the head of the salt tip (salt head) to the upstream, the density of the flow is the homogenous vertically since the fresh flow exists whole the water depth (Fig. I-1). In the other side of the salt tip region (right region of the salt head), the density is stratified and separated relatively into two layers (Fig. I-1). The upper layer (near the free surface) is the fresh layer where the density is mostly homogenous vertically. The lower layer (near the bottom) is the salt layer where the density is relatively stratified (Geyer, 1993).

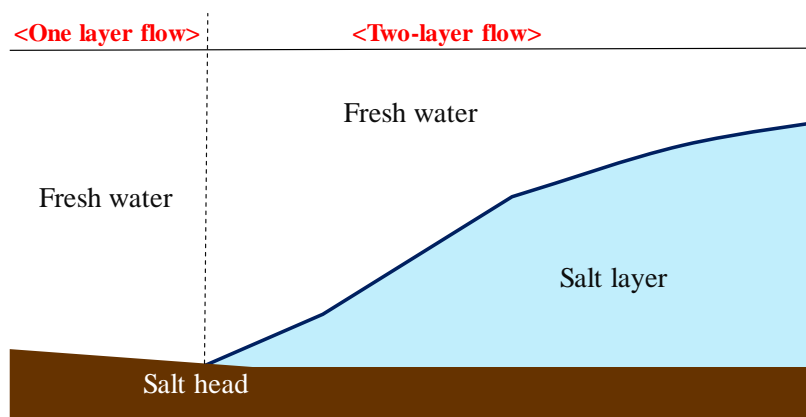


**Fig. I-1** The density structure in the salt tip region



### 1.1.2 Overview of the flow modes for two-layer flow

In downstream of the salt head where the two-layer flow exists, there are two kinds of the flow mode observed that are uni-directional (Fig. I-2(a)) and bidirectional (exchange flow) (Fig. I-2(b)). In which, the flows at the salt tip are frequently appear in the uni-directional mode (Sanford et al., 2001; Geyer, 1993). However, the bidirectional flow may be observed during the slacks in the upstream of the Cheksapeak Bay (Sanford et al., 2001) when the salt tip locates at the toe of the bottom slope. Besides, the exchange flow may be observed in around the geometric features such as at the downstream of the constrictions (Geyer and Ralston, 2015) or on the slope in nearshore coastal ocean (Masunaga et al., 2015; Walter et al., 2012; Carter et al., 2005).

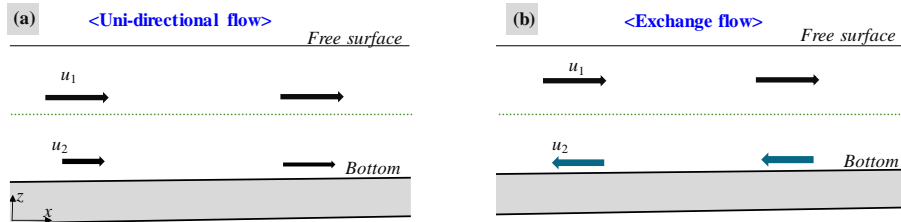


**Fig. I-2** The side view structure of the two modes of the two-layer mechanism. (a) Uni-directional flow; (b) The exchange flow

### 1.1.3 The effects of the geometry features

The effects of the geometry on the flow of the two-layer flow in the relationship with the Froude number are given in the following equations (Armi, 1986; Zhu and Lawrence, 2000):

$$\frac{\partial u_1}{\partial x} = \frac{-Fr_2^2}{1-G^2} \frac{u_1}{D_1} \frac{dz_b}{dx} - \frac{1-Fr_2^2 \left(1 + \frac{D_2}{D_1}\right)}{1-G^2} \frac{u_1}{W} \frac{dW}{dx} + f_1 \frac{dE_1}{dx}, \quad (1.1)$$

$$\frac{\partial u_2}{\partial x} = \frac{1 - Fr_1^2}{1 - G^2} \frac{u_2}{D_2} \frac{dz_b}{dx} - \frac{1 - Fr_1^2 \left(1 + \rho_1 D_2 / \rho_2 D_1\right)}{1 - G^2} \frac{u_2}{W} \frac{dW}{dx} + f_2 \frac{dE_1}{dx}, \quad (1.2)$$

$$\frac{\partial D_1}{\partial x} = -\frac{-Fr_2^2}{1 - G^2} \frac{dz_b}{dx} + \frac{G^2 - Fr_2^2 \left(1 + D_2 / D_1\right)}{1 - G^2} \frac{D_1}{W} \frac{dW}{dx} + f_3 \frac{dE_2}{dx}, \quad (1.3)$$

$$\frac{\partial D_2}{\partial x} = -\frac{1 - Fr_1^2}{1 - G^2} \frac{dz_b}{dx} + \frac{G^2 - Fr_1^2 \left(1 + \rho_1 D_2 / \rho_2 D_1\right)}{1 - G^2} \frac{D_2}{W} \frac{dW}{dx} + f_4 \frac{dE_2}{dx}, \quad (1.4)$$

where the  $W$  and  $z_b$  are the width of the channel and the elevation of the bottom, respectively. The  $u_1$ ,  $u_2$  are the velocity of each layer and  $D_1$  and  $D_2$  are the thickness of each layer, respectively. The  $\rho_1$  and  $\rho_2$  are the density of the lighter (upper) layer and denser (lower) layer. The  $f_1$ ,  $f_2$ ,  $f_3$  and  $f_4$  are the coefficient terms of the energy lost which are relative with Froude number, velocity and depth. The  $dE_1/dx$  and  $dE_2/dx$  are the function of the frictions and nonhydrostatic correction (Zhu and Lawrence, 2000). For the specified case such as without variation of the width,  $dW/dx$  will be zero (Fig. I-3(a)). On the other hand, without the effects of the slope,  $dz_b/dx$  will be zero (Fig. I-3(b)).

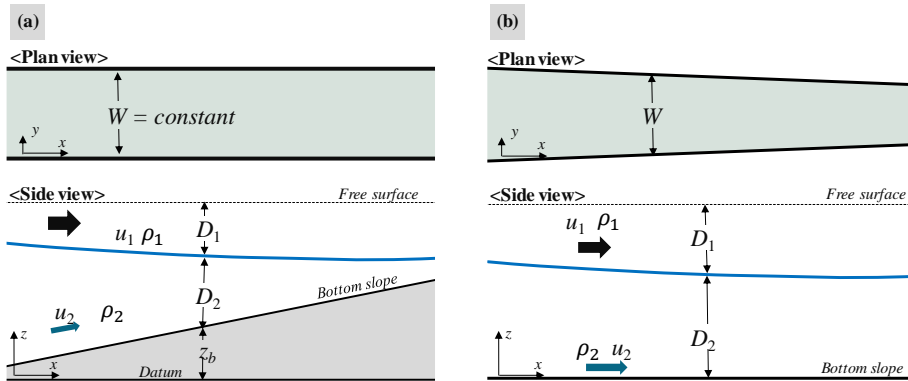


**Fig. I-3** Definition sketch for the two-layer flows with the free surface under effects of the geometry. (a) Bottom slope effect. (b) The contraction of the width effect.

The composite Froude number ( $G^2$ ) in equation (1.1) - (1.4) can be express as

$$G^2 = Fr_1^2 + Fr_2^2, \quad (1.5)$$

where  $Fr_1^2 = \frac{u_1^2}{g'D_1}$  and  $Fr_2^2 = \frac{u_2^2}{g'D_2}$  are the internal Froude number of

the upper layer (lighter density) and lower layer (heavier density). The  $g' = g\Delta\rho/\bar{\rho}$ , is the reduced gravitational acceleration, and  $\bar{\rho}$  is the averaged density. Similar to the traditional Froude number ( $Fr$ ), the flow state is termed critical since the composite Froude number ( $G^2$ ) equals nearly unity or equals unity.

For both the uni-directional flow and exchange flow, the common critical point for the existence of the hydraulic jump that is at the crest of the obstacle when  $dz_b/dz = 0$  (Fig. I-4(a)) or the narrowest of the constriction where  $dW/dx = 0$  (Fig. I-4(b)) (Armi, 1986; Armi and Farmer, 1986; Baines, 1995). However, without the critical condition caused by the geometry, the hydraulic jump still may have another chance to occur that are when the flow is as a form of the exchange flow without the upstream depth of denser layer, such as the density currents, the overturns in the internal bore, etc.

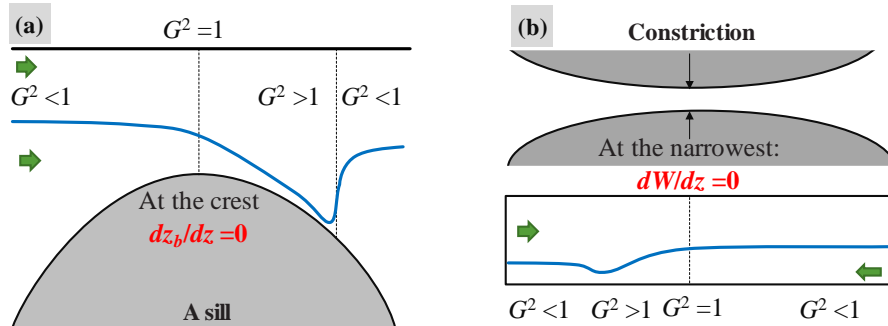


**Fig. I-4** An example for the two-layer flow through the geometry. (a) Side view of the uni-directional flow over the sill (Staalstrøm et al., 2014); (b) Plan view and side view for the two-layer exchange flow through a constriction (Armi and Farmer, 1986).

The density current is the density fluid flow propagating over/under another fluid flow (Fig. I-5) (Simpson, 1982). In which, the interface between two fluid flows normally is considered as the density front which may be broken under the certain flow condition, and this process is normally called as the breaking of the front (Benjamin, 1968). For the common phase, the edge of the density moves at the same speed as the flow, and at that time, Froude number normally observed is at about unity (Simpson, 1980; Baines, 1995). However, if the Froude number observed at the density front is far bigger than unity, the density currents may be considered as a special type of the two-layer hydraulic jump (Simpson, 1982; Benjamin, 1968; Baines, 1995). For that type, the heavier fluid discharged the mass to the lighter fluid through at the head of the density current (Fig. I-5) (Baines, 1995). At the transition as a overturn (Baines, 1995), the mixing is intense and the head of the current is a “head wave” or “supercritical head” as the breaking of the front (Benjamin, 1968; Xu, 1991). The hydraulic jumps as an overturns normally appear in regions where the geometrical features such as the bottom slope or the contraction of the width are observed. Evenly, the geometry feature and the seaward flow seems to be play an important for the development of the hydraulic jump.

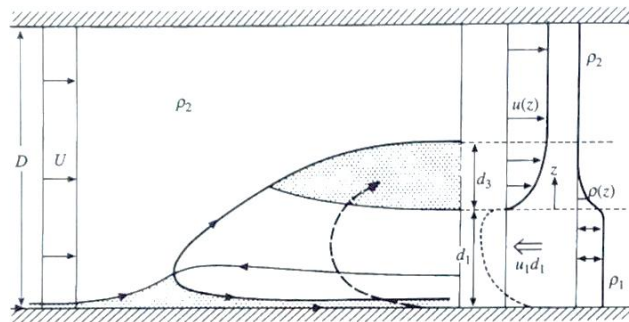


**Fig. I-5** An sketch of the density current head as the two-layer hydraulic jump (Baines, 1995).

#### ***1.1.4 The existence of the overturn and its effects on the sedimentary transport processes***

On the gentle slope of the river mouth, the overturn appears in the tidal bore on the free surface during the shoaling process of the incoming tide. Under effects of the river flow, bottom slope and friction, the sharp of the tidal wave is progressively distorted until a wall of water is formed as the bore (Bartsch-Winkle and Lynch, 1988; Savenije, 2005; Chanson, 2011a). Koch and Chanson, (2008) and Chanson, (2010a) found that when surge Froude number observed is from 1.3 to 1.6, the high energy is dissipated and the hydraulic jump can occur as a bore in rollers form (the bore roller) (Koch and Chanson, 2008; Chanson, 2010a). Peregrine and Svendsen, I. A. (1978) and Lubin and Chanson, (2017) suggested that the roller bores are the hydraulic jump in translation.

For two-layer flow, the overturns are generated from the shoaling process of the internal tide on bottom slope of the continental shelf (Petruncio et al. 1998; Wang et al. 2008) or of the coastal regions (Masunaga et al., 2015; Walter et al., 2012; Carter et al., 2005). During shoaling time to shallower water depth, the previous works (e.g., Klymak et al., 2007; Hosegood et al., 2004; Masunaga et al., 2015) observed that the streamwise currents are much accumulated at troughs of the internal tide during shoaling time to shallower water depth (Fig. I-6). Besides bottom slope, the strong turbulent mixing by the overturn is generated when the backflow from previous period encounters the front face from the incident intertidal wave (Helfrich, 1992; Wallace and Wilkinson, 1988; Masunaga et al., 2017). Masunaga et al.,(2017) found that the shear flow from the bottom friction and the vertical shear between the

interface of the two-layer exchange flows are important for the convergence of the horizontal flows. Masunaga et al., (2015) recorded that the horizontal currents at the overturn of the internal bore reaching 0.1m/s and 3.0 cm/s of the corresponding vertical velocity (  $|w| > 2$  cm/s). The strong horizontal and vertical velocity in the overturn are also the potentials for resuspension of sediment (Boegman and Ivey, 2009; Masunaga et al., 2015).

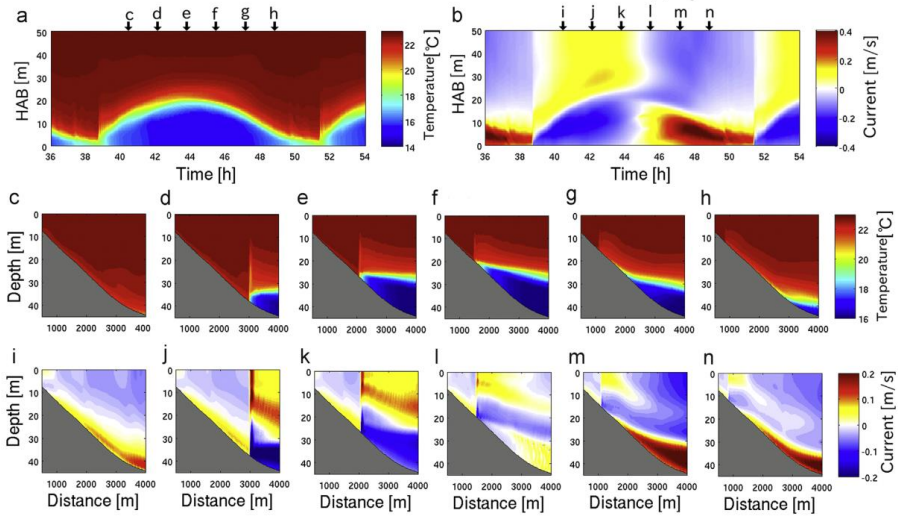


**Fig. I-6** The shoaling process of the internal tide on bottom slope in the Otsuchi Bay leading to the development of the internal bore shown (Masunaga et al. 2015).

Above discussions show that the bottom slope and the backflows can make the significant frictional resistance and induce for the hydraulic jump as the breaking of the internal tide or the density front. Therefore, if an estuary has a slope at the upstream of channel, the breaking of the salt tip front may occur due to the interaction between the upstream direction density flow and the downstream freshwater flow, similarly to the breakings of the density front of internal tide meeting a critical slope of the coastal regions. The upstream of the

Chesapeake bay has a slope near the salt tip region, and although this slope angle is much milder than those of the nearshore coastal ocean, the overturns was still observed by many researches such as North et al. (2004) or Sanford et al. (2001).

Kim et al., (2007) showed that the region near the salt tip in the upstream of the Chesapeake Bay has the bottom with a local slope of 10 m height over around 10 km length (Sanford et al., 2001). Although the angle of mild slope observed in Kim et al., (2007) (Fig. I-7(a)) is about ten times smaller than the angle of the bottom slope observed in the Otsuchi Bay but the salt front meets the significant interaction with the river flow on the slope. The magnitude of the river flows in the upstream of slope in the Chesapeake bay vary between 10 cm/s and 17 cm/s (North et al. 2004). Moreover, much higher concentration of the suspended sediment near salt front of upstream the Chesapeake Bay are observed (Fig. I-7(b)).

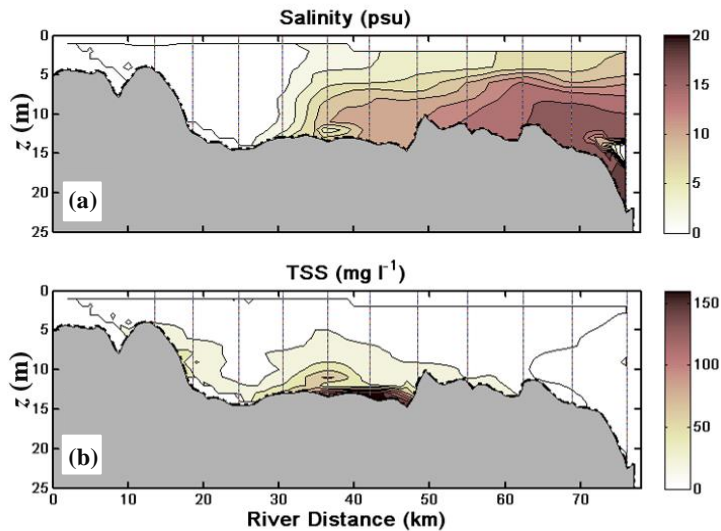


**Fig. I-7** The comparisons in the bottom slope, salinity and sediment concentration between the salt tip region in the upstream of the Chesapeake Bay near the slack before from Kim et al., (2007).

Much higher concentration observed in the upstream of the Chesapeake Bay seems to be relative with the overturn. Sanford et al., (2001) reported that the overturn at the upstream of the Chesapeake Bay occur in the slack before flood or slack before ebb, and during these periods, the highest concentration of the sediment is observed around the front of the salt tip. When the velocity of the wind near the water surface is large, the magnitude of the overturn is enhanced, the concentration of the sediment at the salt tip is significantly promoted (Sanford et al., 2001). The magnitude of the flow affect to the sedimentary process, the observation of the North-Houde (2001) show that the sediment concentration observed on the mild slope for the high river flow condition is much larger than that in the low river flow condition. Further, Geyer (1993) showed that the sediments can be transported vertically by overturn to the upper layer from the bottom even with the strong stratification near the head of salt tips (Fig. I-8).

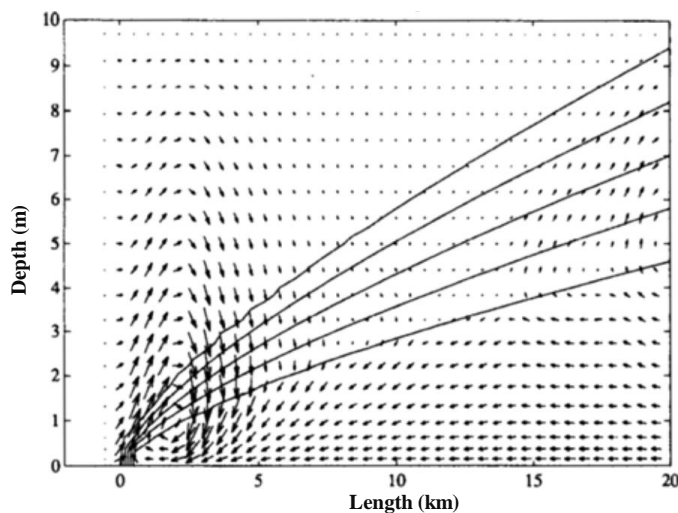


**Fig. I-8** The sediment flux with the overturn at the salt tip in Geyer (1993)



## 1.2 Literature review

### *1.2.1 Mixing and sedimentary processes under the effects of the bottom slope*

Normally, the sediment transport processes at salt tip regions are driven by the residual estuarine circulation and the tidal asymmetry. The residual estuarine circulation is relative with the unbalance between the seaward flow near the surface and the landward flow near the bottom (Burchard and Schuttelaars, 2011). Under effect of the tidal asymmetric flux, sediment near the surface is transported seaward and the sediment near the bottom is transported landward (Burchard and Schuttelaars, 2011).

The other dynamics process driving the convergence of the sediment at the salt tip that is the tidal straining. The tidal straining mechanism is relative with the tidal asymmetries in the turbulent mixing (Jay & Musiak, 1994). Further, Simpson et al., (1990) suggested that the tidal straining is relative with both the periodically oscillating stratification and vertical shear in the streamwise velocity. As a result, not only water parcel but also planktons, organic and sediment particles move to the landward (Lucas et al., 1998; Scully & Friedrich, 2007; Geyer, 1993; Burchard et al., 2018) until converging at the salt tip zone.

The convergences of the sediment driven by the tidal straining and tidal pumping have been studied and discussed well by the many previous researches (Allen et al. 1980; Jay & Musiak, 1994; Geyer, 2001; Yu et al., 2014). In which, even though the overturn process could be one of the important processes driving the vertical migration of the sediment, it did not get much attention nor be well so far discussed such as in Sanford et al (2001), Geyer (1993) and North-Houde (2001).

- (1) Sanford et al (2001) emphasized the importance of tidal asymmetry, the convergence of gravitation circulation, and the relative position of the cohesive sediment pools for convergence of the sediment at the upstream of the Chesapeake Bay. They also discussed the role of resuspension for the high turbidity maximum regions (ETM regions) but they didn't explain in detail why the resuspension is enhanced in the perspectives of flow dynamic but only concentration of convergence of circulation and relative locations of sediment pools. Sanford et al. (2001) also reputed that the sediments do not resuspend a lot in the exchange mode of ebb flow even with the strong overturn at the front due to the suppression by stratification, compared to the full flood. However, the view of Sanford et al. (2001) seems be inverse the view of the Geyer (1993) about the roles of the overturn.
- (2) Geyer (1993) illustrated the overturns from the vectors of the sediment flux. According to Geyer (1993), the overturn flows seem to strongly induce the vertical migration of the suspended sediments. Even after he emphasized the importance of overturn processes, it has not been discussed further which factors dynamically determine the overturn processes.
- (3) North and Houde (2001) found that the sediment concentration around the end of the salt tip is proportional with the fresh water magnitude. However, North and Houde (2001) supposed that the increase of the magnitude of fresh water leads to enhance the convergence of the sediment through the strength of gravitational circulation. Therefore, North and Houde (2001)

and other works ignored the effect of the river flow on the local vertical suspension of the sediment as well as ignored another important factor affecting to the interaction between the river flow and the salt flow that are the bottom slope.

- (4) The effects of the bottom slope and the downslope flow (backward flow) on the development of the internal bore with an overturn were already studied and discussed well in Masunaga et al., (2015; 2017; 2018) or in other researches such as Helfrich, (1992), Wallace and Wilkinson, (1988). Evenly, the Froude number at front of the internal bores in the Otsuchi Bay is approximately 1.3 (Masunaga et al., 2015). The Froude number is larger than 1.0 meaning that the internal bore seems to be a single wave advected from the hydraulic jumps. However, they studied the development of the overturn for the coastal regions where the bottom slope angles are far larger than those in the estuaries. Although the surrounding physical and geomorphological conditions of the coastal regions (Walter et al., 2012 and Masunaga et al., 2015) are very different from that of the estuary (Sanford et al. 2001; North and Houde, 2001; Geyer, 1993), but phenomenologically the overturning event at the density current head at two different locations look very similar.

### ***1.2.2 The effects of the upstream contraction of the width***

Besides the bottom slope, the contraction of the width may cause a hydraulic jump. By experiment method, Henderson (1966) showed that a hydraulic jump as the shock waves can develop on the water surface when the

supercritical flows over the contraction section of the channel. However, this experiment has been done for the homogeneous fluid.

In the estuary where the density is stratified vertically, the baroclinic exchange flows, which are supposed to be important for the development of the density current, and the hydraulic jump may be found at the downstream of the constrictions where the widths are landward contracted (Geyer and Ralston, 2015) (Fig. I-9(a)-(c)). The baroclinic exchange flow occurs in the several hours near the end of the ebb as the landward flow develops in a thin layer above the bed (Fig. I-9(b)). The landward currents remain and even encounter the ebb currents in the throat region of the constriction for the several hours during slack for flood (Fig. I-11(a)-(b)). Although the baroclinic exchange flows are confirmed to be very important to the convergences of the along estuary currents and the development of the density fronts in Hudson River estuary (Fig. I-9(a)-(c)), some parts in their dynamics have not been clearly understood, especially in the influence of the gradual contraction associated with the interaction of the ebb flow (Geyer and Ralston, 2015). Theoretically, the gradual reduction of the width ( $dW/dx < 0$ ) affects to not only the depth of water but also affects to the magnitude of the flow and their effects are in a similar way to the positive bottom slope ( $dz_b/dx > 0$ ) (Equation (1.1) -(1.4)). Therefore, if the exchange flow may cause a hydraulic jump as the breaking of the front on the mild slope, we can expect that the exchange flow may cause similar results in the gradual contraction region.

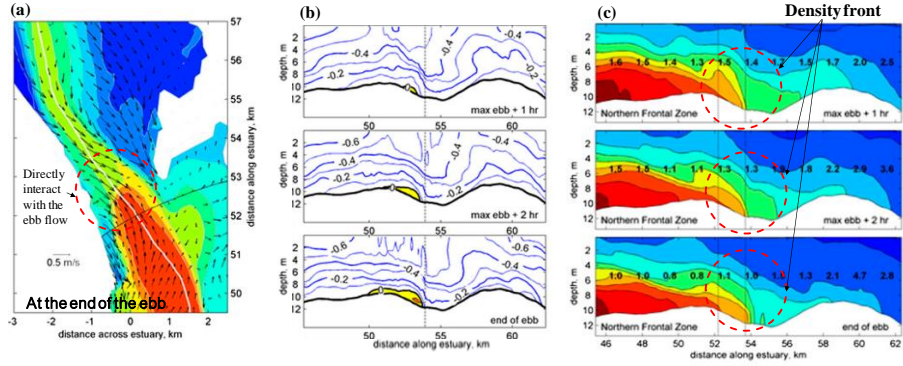


**Fig. I-9** Plan view and side view of salinity concentration (psu), currents and the Composite Froude number  $G$  around the constriction at 54 km distance in Hudson river. (a) The plan view of the salinity concentration and with the currents near the end of the ebb phase. (b) The side view of contours of the flow magnitude. (c) The side view of the salinity concentration and Composite Froude number  $G$ .

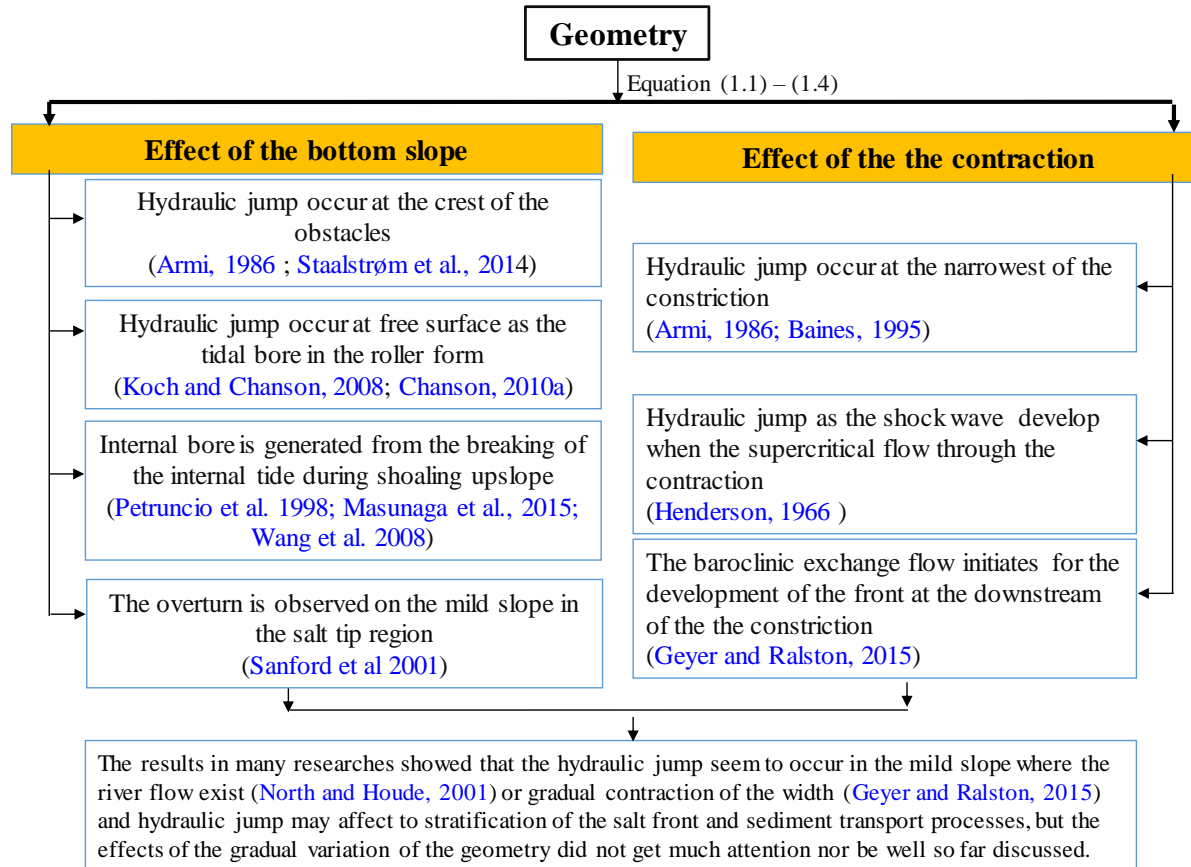


**Fig. I-10** The summary of literature review and the reasons for research.

### 1.3 Objective

The objectives of this research can be listed as follows:

1. To identify the existence of the overturn in the salt tip on the mild slope and its effects on stratification and mixing
2. To investigate the effects of the gradual width contraction on propagation of the density flow of the salt tip to the narrower upstream channel
3. To relate the sediment suspension and flux to the above two geometrical features driven mixing processes
4. To explain the mechanism occurring the overturning at the salt tip in terms of internal hydraulic jump

To answer the above questions, we use the Sunans model to compute the estuarine dynamics of the salt tip for both the mild slope and the contraction of the width domain. The domains with the slope are as like as the slope observed in the upstream of the Chesapeake Bay. The all domains of this research are setup in the ideal channels, running in both 2D or 3D model.

## **1.4 Outline of the Thesis**

The present study reports the findings and methods by seven chapters. The assessment tools and the theory of the SUNTANS are shown in chapter II. Chapter III contains the experimental set-ups, study case and the grid convergence. Chapter IV and chapter V present and discuss the existence of the overturn and the mixing as well as and the sedimentary transport processes in the mild slope region and the gradual contraction region, respectively. Chapter VI focuses on explaining the mechanism for the development of the overturn as the term of the hydraulic jump. The thesis ends with summary and recommendations in chapter VII. The overview of content thesis is shown in Fig. I-11.



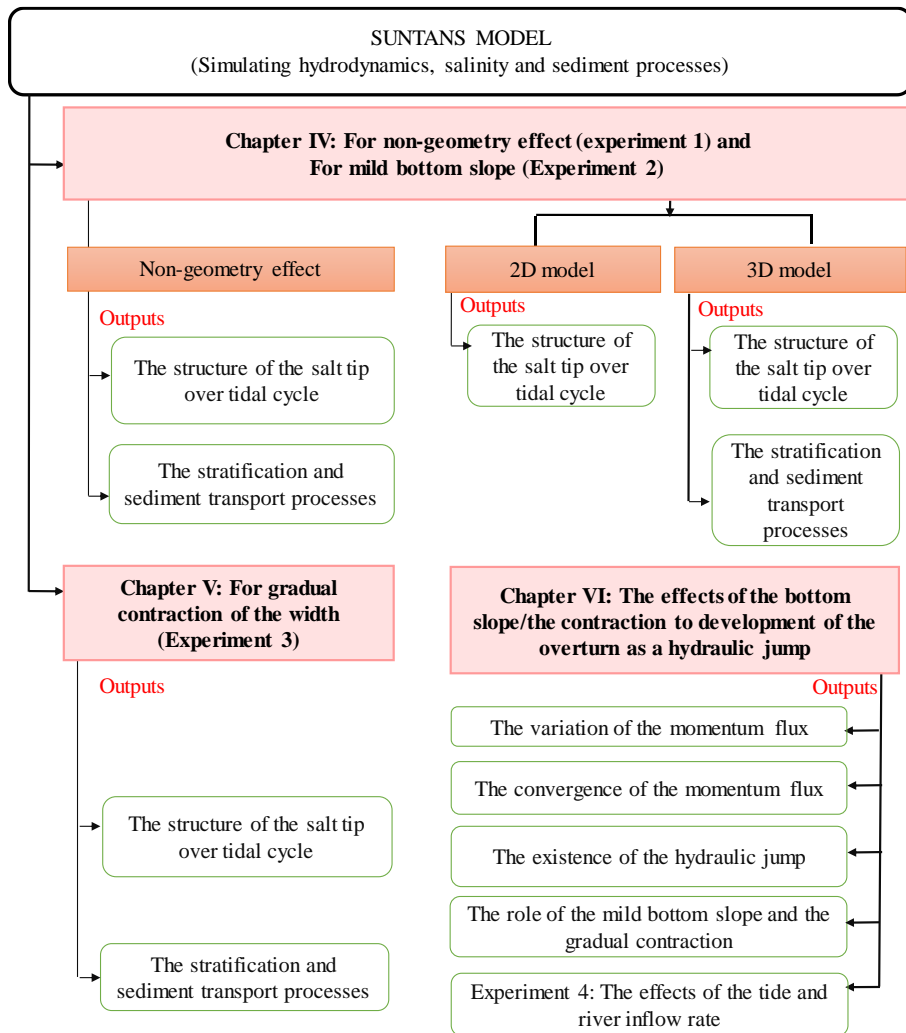


**Fig. I-11** Thesis overview

# CHAPTER TWO

## II. METHODOLOGY

### 2.1 The assessment tools

To find out the dynamics of overturns and its effects on the mixing and transport of salt and particles, main parameters which are used here are: The Richardson number ( $Ri$ ), the kinetic energy dissipation rate ( $\varepsilon$ ), the total momentum flux ( $Mf$ ) and the Froude number ( $Fr_f$  and  $G^2$ ). Relative strength of the mixing and stratification in flows is characterized by the  $Ri$  and  $\varepsilon$  quantifies the relative strength of turbulence in flows and mixing. To quantify the accumulation of momentum during the shoaling process, the momentum flux is used. the mechanism of occurrence of hydraulic jump is investigated with using the Froude number. Along with such hydraulic parameters, to study the effects of front head mixing to the sedimentary process, the sediment fluxes are investigated.

#### 2.1.1 *The high kinetic dissipation rate*

Bottom shear stress, tidal straining and lateral circulation are as known as main processes to generate mixing of the salt water in the estuaries (e.g., Jay and Musiak, 1994; Uncles et al., 2006; Scully & Friedrich, 2007). To quantify elaborately and distinguish the mixing generated by breaking of the front from straining and lateral flow, the energy dissipation rate ( $\varepsilon$ ) and the Richardson number ( $Ri$ ) are computed and compared together. Normally, at the internal bore front on the continental shelf where the internal tide breaks, the high kinetic dissipation rate is observed. For instance, Richards et al., (2013) reported that

the kinetic dissipation rate is greater than  $10^{-5}$  W/kg, which was measured near the internal bore during shoaling process. Masunaga et al., (2015) also observed over  $10^{-6}$  W/kg of the dissipation rate near the internal bore head and along the isopycnal interface, while in other regions where there is far from the internal bore,  $\varepsilon$  was much smaller than  $10^{-7}$  W/kg. Therefore, the kinetic dissipation rate is popularly applied for quantifying the turbulence strength of the breaking of the internal tide in the near-shored coastal regions (Klymak et al., 2007; Masunaga et al., 2015) or breaking of internal solitary waves (Carter et al. , 2005). The reason why the dissipation rate is used for the turbulence strength in field measurements rather than turbulence kinetic energy itself is that turbulence kinetic energy could include also larger scale fluctuations of wave or vibration of ship or equipment. To discuss in a cord with the previous works, the present work computes and compares the kinetic dissipation rate ( $\varepsilon$ ) given by Gerrity and Black, (1993) such as

$$\varepsilon = \frac{q^3}{lB_1} \quad (2.1)$$

where  $q$  is the turbulent velocity scale and  $l$  is the turbulent length scale.

The constant value  $B_1$  is at 16.6.

### ***2.1.2 The gradient Richardson number***

While the high dissipation rate implies the strong turbulent mixing in the internal bore, the relative dominance between the mixing and the stratification can be quantified by the gradient Richardson number ( $Ri$ ). The parameter is widely used to describe the relative stability of the stratified shear flow (West et al., 1986; West and Shiono, 1984; Kim et al., 2018) and defined as:

$$Ri = \frac{g}{\rho} \frac{\partial \rho / \partial z}{(\partial u / \partial z)^2 + (\partial v / \partial z)^2}, \quad (2.2)$$

where the  $g$  is the gravitational acceleration and  $u$ ,  $v$  are the streamwise and lateral velocities, respectively. The  $\rho$  is the water density component. Based on the previous works such as Miles and Howard, (1964) or Hazel, (1972), flow is actively mixing if  $Ri$  is less than 1/4 and as  $Ri$  is getting larger than this value, flow seems to become more stably stratified. The  $Ri$  is zero when the vertical density profile of water is homogeneous (from equation (2.2)). Therefore, the high dissipation rate and the small gradient Richardson number ( $Ri \leq 1/4$ ) indicate vigorous mixing around the salt front.

### ***2.1.3 The total sediment flux***

Besides the strong saline mixing, the breaking of the internal tidal bore at front resuspends sediments significantly by enhancing the vertical turbulent flux flux (Boegman and Ivey, 2009; Masunaga et al., 2017, 2019). To confirm that the braking of the front is a main driving force for resuspension of sediments among many processes, the sediment flux is decomposed depending on each mechanism similar as Scully and Friedrichs (2003) did for the momentum flux. According to Scully and Friedrichs (2003), the total momentum flux includes two individual components and one is flux by the tidal pumping (pumping) and another is non-tidal advection sediment flux (advection). The present work decomposes the pumping and advection fluxes to the streamwise and lateral portions as follow:

$$u(x, y, z)C(x, y, z) = \underbrace{\langle u(x, y, z) \rangle \langle C(x, y, z) \rangle}_{\text{Tidal averaged}} + \underbrace{u'(x, y, z)C'(x, y, z)}_{\text{fluctuation}}, \quad (2.3)$$

$$v(x, y, z)C(x, y, z) = \underbrace{\langle v(x, y, z) \rangle \langle C(x, y, z) \rangle}_{\text{Tidalaveraged}} + \underbrace{v'(x, y, z)C'(x, y, z)}_{\text{Fluctuation}}, \quad (2.4)$$

where  $C(x, y, z)$  is the concentration of the suspended sediment,  $u(x, y, z)$  and  $v(x, y, z)$  are the streamwise and the lateral one, respectively. Angled brackets indicate tidal average quantities and the primes denote the deviations from the tidally averaged values.

Using the equations (2.3) and (2.4), total depth integrated sediment fluxes are composed of sediment fluxes by the advection and pumping respectively in the longitudinal direction and the lateral direction at the center of  $y$ -axis ( $y = 0$ ) as following equations:

$$SF_x = \underbrace{\int_{z=-H}^{z=\eta} \langle u(x, y, z)C(x, y, z) \rangle dz}_{\text{Advection}_x} + \underbrace{\int_{z=-H}^{z=\eta} u'(x, y, z)C'(x, y, z) dz}_{\text{Pumping}_x}, \quad (2.5)$$

$$SF_y = \underbrace{\frac{2}{W} \int_{y=-W/2}^{y=0} \int_{z=-H}^{z=\eta} \langle v(x, y, z)C(x, y, z) \rangle dz dy}_{\text{Advection}_y} + \underbrace{\frac{2}{W} \int_{y=-W/2}^{y=0} \int_{z=-H}^{z=\eta} v'(x, y, z)C'(x, y, z) dz dy}_{\text{Pumping}_y}, \quad (2.6)$$

where  $z = \eta$  is the coordination of water surface and  $z = -H$  is the coordination of the bottom. The  $W$  is the estuarine width.

According to Geyer (2001), the variations of streamwise advected sediment flux ( $\text{Advection}_x$ ) may reflect for the variations of the gravitational circulation, and the effects of the tidal pumping may be inferred from the size of the streamwise tidal pumping flux ( $\text{Pumping}_x$ ). We investigate the relative contributions of lateral processes on the sediment concentration variations at the thalweg. The lateral process is also decomposed into the lateral advection portions

(Advection<sub>y</sub>) and pumping portions (Pumping<sub>y</sub>) for the whole lateral sediment fluxes. Total momentum flux is also calculated through a water column at a middle point of channel and compared to the total flux of sediment ( $SF = SF_x + SF_y$ ) to understand the relationship between total sediment flux and a process driving fluxes of sediment in particular related with the breaking and mixing of/at the density front.

#### **2.1.4 The total momentum flux**

To find out the reasons for the breaking of the density front at the salt tip which affects to the sediment transport process and mixing process, the accumulation of energy at the salt tip is investigated because the breaking of the internal tidal is initialed from the accumulation of energy in mass and velocity at the trough (Van Gastel et al., (2009) or Masunaga et al., (2017). In our work, the momentum fluxes are calculated by following Umeyama and Shintani, (2006). However, instead of considering the total flux of the horizontal momentum across a plane caused by the propagating of the wave as Umeyama and Shintani, (2006), we consider the total momentum flux across a plane for fluid at the salt tip ( $Mf$ ) caused by the fresh flow and salt flow (Fig. II-1) that is

$$Mf = \int_{h_1-\eta_2}^{\eta_1} (p_1 + \rho_1 u_1^2) dz + \int_{h_1+h_2}^{h_1-\eta_2} (p_2 + \rho_2 u_2^2) dz, \quad (2.7)$$

where the streamwise velocities in fresh and salt water layers are  $u_1$  and  $u_2$ , respectively.  $p_1$  and  $\rho_1$  are respectively the pressure and density of the upper water layer (the fresh water) and  $p_2$  and  $\rho_2$  are respectively the pressure and density of the salt water layer. The thicknesses of the fresh and salt layers are  $h_1$  and  $h_2$ , respectively. The interface between two layers is determined by vertical

displacement of the salt layer,  $\eta_2$  from  $z = h_2$ . From  $z = h_1$ , fresh layer has a vertical displacement of the water surface  $\eta_1$ .

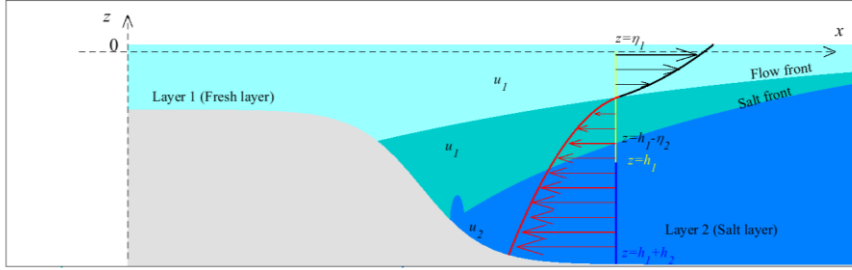


**Fig. II-1** Diagram of the vertical structure for the salt tip zone in the present work.

To examine the variations of the momentum flux in each layer and the processes driving those variations, total momentum fluxes of each layer in equation (3.7) are decomposed into two components of the fresh water layer ( $Mf_1$ ) and for salt water layer ( $Mf_2$ ) as :

$$Mf_1 = \underbrace{\int_{h_1-\eta_2}^{\eta_1} p_1 dz}_{Mf_{1p}} + \underbrace{\int_{h_1-\eta_2}^{\eta_1} \rho_1 u_1^2 dz}_{Mf_{1u}}, \quad (2.8)$$

$$Mf_2 = \underbrace{\int_{h_1+h_2}^{h_1-\eta_2} p_2 dz}_{Mf_{2p}} + \underbrace{\int_{h_1+h_2}^{h_1-\eta_2} \rho_2 u_2^2 dz}_{Mf_{2u}}, \quad (2.9)$$

where  $Mf_{1p}$  and  $Mf_{2p}$  are as a pressure components of the momentum flux for fresh and salt layers, respectively.  $Mf_{1u}$  is a kinetic momentum flux in the fresh layer and  $Mf_{2u}$  is a kinetic momentum flux in the salt layer. If the salt tip becomes thicker as the internal bores in Masunaga et al., (2015), the pressure component of momentum flux increases. Similarity, fast convergence of the velocity leads to increase the kinetic momentum flux at the salt tip. In any case,

the salt tip front breaks only if the momentum flux increases and so the mass and the streamwise velocity increase.

### 2.1.5 The Froude numbers

The Froude number of the front has been used to study the hydraulic jumps at the interface of the density in the previous works (e.g., Simpson, 1982; Baines, 1995; Nash and Moum, 2005). The present work applies a definition of the Froude number in Nash and Moum (2005), which is defined as:

$$Fr_f = \frac{u_f}{c}, \quad (2.10)$$

where  $u_f$  is the speed of flows near the front and  $c$  is the propagation speed of the front. The  $c$  equals a distance traveled divided by a given period. Similar to the general Froude number, when  $Fr_f$  is larger than unity, flows at the density front become supercritical (Lean & Whillock, 1965).

Besides, we use the composite Froude number ( $G^2$ ) to quantify the state flow from the salt tip to the downstream (for stratified flow) (Fig. II-1). For two-layer flow including the salt layer and the fresh layer, the composite Froude number ( $G^2$ ) with a free surface can be expressed as

$$G^2 = Fr_1^2 + Fr_2^2, \quad (2.11)$$

where  $Fr_1^2 = \frac{u_1^2}{g'D_1}$  and  $Fr_2^2 = \frac{u_2^2}{g'D_2}$  are the internal Froude numbers of the

salt layer (Layer 1) and fresh layer (Layer 2), respectively. The  $g' = g \frac{\rho_2 - \rho_1}{\rho}$

is the reduced gravitational acceleration. The  $\bar{\rho}$  is the averaged density. The

$D_1$  and  $D_2$  are the thicknesses of the freshwater layer (upper layer) and saltwater



layer (lower layer), respectively (Armi, 1986). Based on the previous works (e.g., Armi, (1986); Farmer and Denton, (1985); Armi and Farmer, 1986) the flow is in the subcritical state since the  $G^2$  is less than 1.0 and for that state, the long internal wave at the interface can travel in both two directions. In contrast, the internal wave can just travel in one direction since  $G^2$  is larger than 1.0 (supercritical condition). At the critical state,  $G^2$  equals unity. The composite Froude number is widely applied to determine whether the state of flow for the stratified flow such as at the estuarine mouth (MacDonal and Geyer, 2004; Armi and Farmer, 1986), at the middle of density front (Geyer and Ralston, 2014). For our work, we use both the composite Froude number ( $G^2$ ) and its internal Froude number ( $Fr_1, Fr_2$ ) to describe the state of the energy for both whole water depth and for each layer (salt layer and fresh layer).

## 2.2 Numerical experiment setups

For the simulations of hydrodynamics and salinity transport, the present work employed the SUNTANS (Stanford Unstructured Nonhydrostatic Terrain-Following Adaptive Navier-Stokes Simulator). The model employs the unstructured-grid and the finite-volume framework for the horizontal plane. This model provides a nonhydrostatic calculation and allows to parallelize running to solve hydrodynamics and salinity transport equations for the estuarine and coastal zones (Fringer et al., 2006). The SUNTANS has been used successfully for studies related with the mixing processes in the shallow water regions such as the salt wedge type estuary (Wang et al., 2008; Wang et al., 2011), or the estuarine mouth regions (Wang et al., 2008; Chua & Fringer, 2011; Holleman et al., 2013), the coastal and the continental shelf zones (Zhang et al., 2011;

Masunaga et al., (2015); Chua & Fringer, 2011). So, the present work uses this model to simulate hydrodynamics and salinity transport in three-dimensional nonhydrostatic mode.

### 2.2.1 The governing equation

The SUNTANS computes based on the three dimensional Reynolds-averaged primitive equations (Fringer et al., 2006):

$$\begin{aligned} \frac{\partial u}{\partial t} + \nabla \cdot (\mathbf{u}u) - fv + bw = & -\frac{1}{\rho_0} \frac{\partial p_n}{\partial x} - \frac{1}{\rho_0} \frac{\partial p_s}{\partial x} - g \frac{\partial}{\partial x} (h + r) \\ & + \nabla_H \cdot (v_H \nabla_H u) + \frac{\partial}{\partial z} \left( v_v \frac{\partial u}{\partial z} \right), \end{aligned} \quad (2.12)$$

$$\frac{\partial v}{\partial t} + \nabla \cdot (\mathbf{u}v) + fu = -\frac{1}{\rho_0} \frac{\partial p_n}{\partial y} - \frac{1}{\rho_0} \frac{\partial p_s}{\partial y} - g \frac{\partial}{\partial y} (h + r) + \nabla_H \cdot (v_H \nabla_H v) + \frac{\partial}{\partial z} \left( v_v \frac{\partial v}{\partial z} \right), \quad (2.13)$$

$$\frac{\partial w}{\partial t} + \nabla \cdot (\mathbf{u}w) - bu = -\frac{1}{\rho_0} \frac{\partial p_n}{\partial z} - \nabla_H \cdot (v_H \nabla_H w) + \frac{\partial}{\partial z} \left( v_v \frac{\partial w}{\partial z} \right), \quad (2.14)$$

where  $u(x,y,z,t)$ ,  $v(x,y,z,t)$ , and  $w(x,y,z,t)$  are the Cartesian components of the averaged velocities in  $x$ ,  $y$ ,  $z$  directions.  $\mathbf{u}$  is the averaged velocity in vector form, and the averaged density and the constant reference density are  $\rho$  and  $\rho_0$  respectively. The  $f = 2\omega \sin \phi$  is the latitude Coriolis terms and  $b = 2\omega \cos \phi$  is the cosine of the latitude Coriolis terms. The  $\phi$  and  $\omega$  are the latitude and the Earth's angular velocity, respectively. The  $\nabla_H$  is the horizontal Laplacian and  $v_H$  and  $v_v$  are the horizontal and vertical eddy viscosities, respectively. The  $p_n$  is the nonhydrostatic pressure component and  $p_s$  and  $r$  are the pressures of the free surface and the baroclinic profile, respectively.

The conservation of mass of the incompressible flow is shown as:

$$\frac{\partial u}{\partial x} + \frac{\partial v}{\partial y} + \frac{\partial w}{\partial z} = 0. \quad (2.15)$$

Integrating this equation from the bottom to the surface and employing a kinematic condition at the free-surface to yield the depth-averaged continuity equation as:

$$\frac{\partial h}{\partial t} + \frac{\partial}{\partial x} \left( \int_{-H}^{\eta} u dz \right) + \frac{\partial}{\partial y} \left( \int_{-H}^{\eta} v dz \right) = 0, \quad (2.16)$$

where the vertical coordination of the bottom and free surface are defined by  $z = -H(x, y)$  and  $z = (x, y)$ , respectively. The density  $\rho$  is determined by the state equation which relates to both the salinity and temperate as follow:

$$\rho = \rho(s, T) \quad (2.17)$$

where  $s$  is the salinity and  $T$  is the temperature, but here we considered salinity into density only for simplification. Since the effect of the temperature is neglected,  $\rho$  is determined by the state equation which just relates salinity and so the transport equation of density is given by bellow equation:

$$\frac{\partial \rho}{\partial t} + \nabla \cdot (\mathbf{u} \rho) = \nabla_H \cdot (k_H \nabla_H \rho) + \frac{\partial}{\partial z} \left( k_v \frac{\partial \rho}{\partial z} \right). \quad (2.18)$$

At the bottom boundary, the bottom shear stress  $\tau_b$  is determined by below equation

$$\tau_b = -\rho_0 C_d |\mathbf{u}| \mathbf{u}, \quad (2.19)$$

where  $C_d$  is the drag coefficient. MY25 method (Melor and Yamada, 1982) is used to get the vertical and horizontal eddy diffusivities. We also use this model to compute the suspended sediment transport. Module for the suspended sediment transport, is developed based on density equations to follow a form of the advection and diffusion equation which is introduced in Fringer et al., (2006):

$$\frac{\partial \rho}{\partial t} + \frac{\partial(uC)}{\partial x} + \frac{\partial(vC)}{\partial y} + \frac{\partial(wC)}{\partial z} = W_s \frac{\partial C}{\partial z} + \frac{\partial}{\partial z} \left( K_v \frac{\partial C}{\partial z} \right) + \nabla_H \cdot (K_H \nabla_H C), \quad (2.20)$$

where  $K_H$  is the horizontal mass diffusion coefficients ( $m^2/s$ ) of the sediment. The  $K_v$  is the vertical mass diffusion coefficients ( $m^2/s$ ) of the sediment and  $W_s$  is the settling velocity of sediment. Those equations and their solutions were explained in very detail by Fringer et al., (2006).

### 2.2.2 Horizontal and vertical grid

SUNTANS use the three-dimensional simulation  $z$ -coordinate approach for the vertical grid direction. Unstructured two-dimensional grids Delaunay triangulation is used. The horizontal velocity  $U$  is defined on the cell faces and the salinity, temperature, eddy viscosity, diffusivities and other scalars are defined at the Voronoi points. On the top and the bottom of the cells the vertical velocity  $w$  is defined at Voronoi points. Depiction of a three-dimensional prismatic grid cell is shown in Fig. II-2.

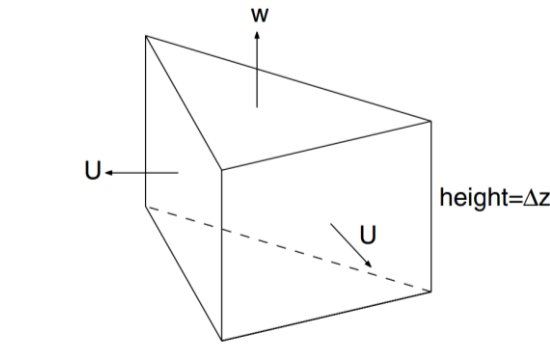


**Fig. II-2** An example of the grid cell used in SUNTANS (Fringer et al., 2006)

## CHAPTER THREE

### III. THE EXPERIMENTAL DOMAIN AND THE GRID CONVERGENCE

#### 3.1 The experimental domain

There are three experiments investigated by the numerical method and these experiments use the domains with 70 km length. In the first experiment (experiment 1), the width of the domain is constant at 500 m and the bottom elevation ( $z_b$ ) is constant at -14.5 m (Non-geometry case) (Fig. III-1(a)). The domain used in experiment 1 can represent for an estuary without the variation of the geometry such as the bottom slope or the contraction.

The domain in experiment 2 was designed to mimic the Chesapeake Bay where the salt tip exists as presented in the previous works (e.g., Sanford et al., 2001; North et al., 2004; Kim Y. H. 2007). To examine the effects of the bottom geomorphology,  $z_b$ , the bottom elevation at the center was set to vary following a tanh equation (Equation (3.1)). The equation is determined by the best fitting of the bottom elevations measured by Kim et al., (2007) (Fig. I-7).

$$z_b(x) = -14.5 + 0.5(14.5 - 4) \left( 1 + \tanh \frac{-3x + 51080.4}{7851} \right) \quad (3.1)$$

Similar to North et al., (2004) and Kim et al., (2007),  $z_b$  obtained by the equation (3.1) remains in the range of between -4.0 m and -14.5 m for  $x < 10$  km and  $x > 25$  km. In the distance of  $10.0 \text{ km} < x \leq 25.0 \text{ km}$ , the bottom elevation  $z_b$  significantly rises to 10 m below the water free surface (Fig. I-7). To study the effects of the bottom slope, the first experiment (Experiment 2(a))

applies the 2D numerical model with 6.0 m of width domain (Fig.III-1(b)). To include the lateral processes in the simulation, we use the domain with 500 m of width and the bottom slope in the second simulation (Experiment 2(b)) (Fig.III-1(c)). In 3D model, the lateral bathymetries of the bottom varies symmetrically at the center and the crosssection of the channel is in a parabolic form as Huijts et al. (2006) did.

Experiment 3 uses domains with the flat and narrow bottom ( $z_b = -14.5$  m) (Fig. III-1(d)). The channel width in experiment 2 varies significantly between  $W = 155$  m and  $W = 500$  m from  $x = 10.0$  km to  $x = 20.0$  km. In the upstream contraction domain, the width is designed based on the following principles: at any  $x$ -location, the cross-section area of this domain (the upstream contraction domain) mostly equals the cross-section area of the bottom slope domain (3D model). Therefore, instead of deforming vertically, the geometry feature of the domain in the last experiment deforms horizontally. Experiment 3 is applied to study for the contraction of the geometry.

The initial and boundary conditions of the salinity for all simulations are inferred from Kim et al., (2007) (Fig. III-2(a)). The upstream boundary at  $x = 0$  km has zero of the salinity while the downstream boundary has salinity concentration ranging from 2.5 psu to 15 psu from the surface to the bottom (Fig. III-2(b)). The friction coefficient for the bottom roughness ( $C_d$ ) is  $2.5 \times 10^{-3}$ , referenced Spitz (1998) work. All simulations ignore the effects of the temperature, wind, and the Coriolis force for simplifications.

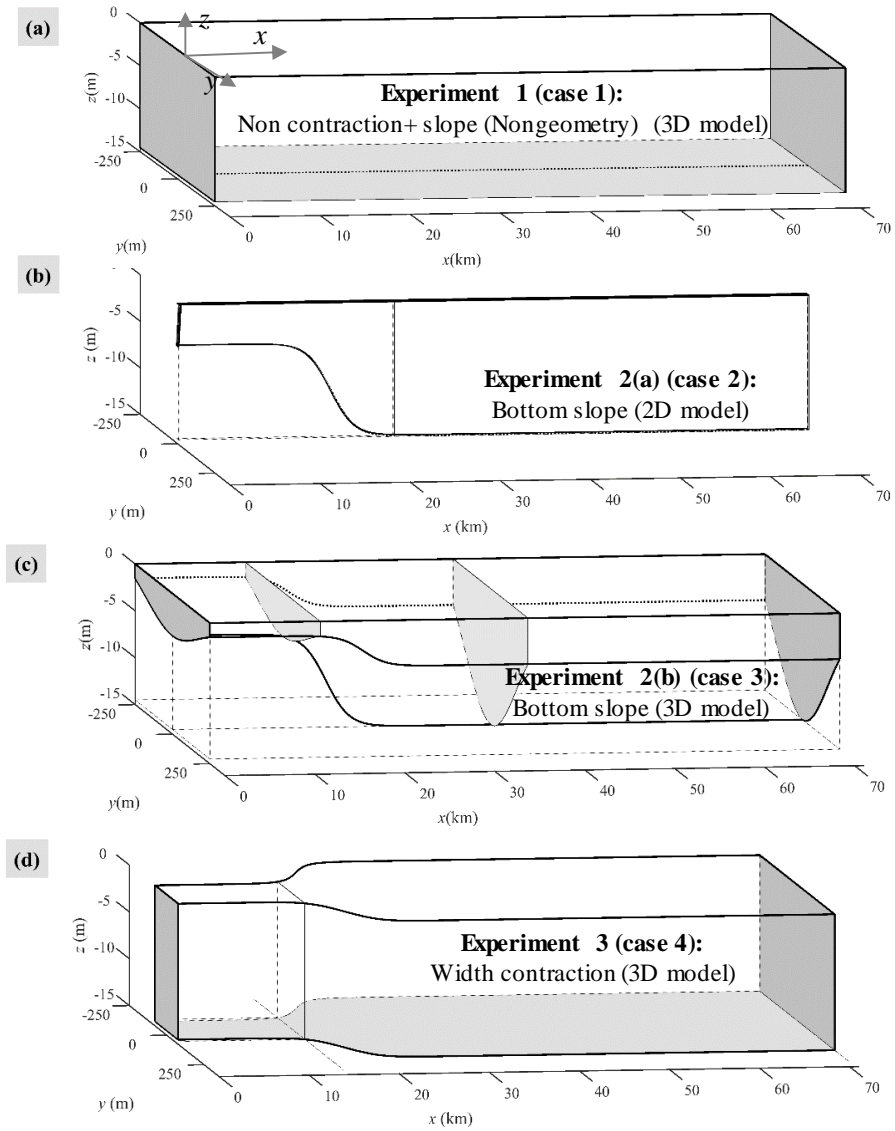


**Fig. III-1** The sketch of the geomorphological conditions in three experiments. (a) The constant width and without the bottom slope; (b) The mild bottom slope for 2D model; (c) The mild bottom slope for 3D model; (d) Upstream contraction of the width.

The settling velocity is set up at  $W_s = 0.3 \times 10^{-3}$  m/s of median settling speed which was estimated in the northern Chesapeake Bay by Sanford et al., (2001). In order to focus on the resuspension of the bottom sediment around the salt tip, we ignore the sediment flux through the upstream and downstream boundaries from the out of the domain. The concentration of the suspended sediment at the bottom is constant at  $0.2 \text{ kg/m}^3$  over all time steps of each simulation.

The amount of freshwater runoff and the tidal amplitudes in the experiment are based from North et al., (2004). For the four main study cases (case 1 to case 4) in three experiments, the average amplitude of the tide ( $\eta_0$ ) is set at 0.5 m and the constant freshwater runoff at the upstream boundary ( $u_0$ ) used is at 0.1 m/s. Besides, in the others study cases, each study we simulate for one among two level of the average amplitude tide that are 0.25 m and 1.0 m and one among two level of the river currents that are 0.05 m/s and 0.17 m/s.

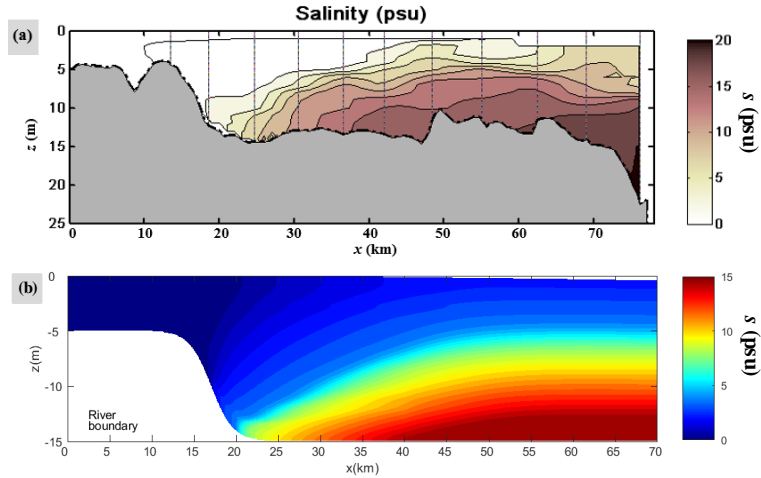


**Fig. III-2** Salinity concentration measured in Kim et al., (2007) and initial salinity concentration in model runs (psu). (a) in Kim et al., (2007); (b) in the model runs.



## 3.2 The grid convergence investigation

### 3.2.1 The grid convergence method

In order to find out a reliable horizontal grid dimension for the meshes in the simulations of the two experiments, we investigate the convergence of the grid from three parameters that are the Root Mean Squared Error ( $RMSE$ ), the  $E_l$ , and the order convergence of the grid ( $\omega$ ). The methods applied to compute the above three parameters are referenced from Ferziger and Peric (2002).

In which, the Root Mean Squared Error ( $RMSE_l$ ) for the  $l^{\text{th}}$  mesh is computed from the below equation:

$$RMSE_l = \sqrt{\frac{1}{N} \sum_{i=1}^N |f_i^l - f_i^{l-1}|^2}, \quad l = 2, 3, \dots, L, \quad (3.2)$$

where  $N$  is the number of the observed points of the  $l^{\text{th}}$  mesh. The  $i$  is the  $i^{\text{th}}$  of the  $N$  observation points.  $L$  is the number of the investigating mesh. The  $f_i^l$  is the value of the scalar given at the  $i^{\text{th}}$  observation point of the  $l^{\text{th}}$  mesh. The  $f_i^{l-1}$  is the value of the scalar given at the  $i^{\text{th}}$  observation point of the  $(l-1)^{\text{th}}$  mesh. The  $RMSE_l$  shows the error between two levels of mesh such as  $(l-1)^{\text{th}}$  and  $l^{\text{th}}$ . The numerical result is converged since:

$$RMSE_2 \geq RMSE_3 \dots \geq RMSE_L. \quad (3.3)$$

In the present work, we will show the plot of the number of cells of each mesh ( $M_l$ ) versus  $RMSE_l$ . If that plot shows a decreasing tendency, this means that the numerical results are converged.

The accuracy of the model with the  $l^{\text{th}}$  mesh is computed by the below equation:

$$E_l = \sqrt{\frac{\sum_{i=1}^N |f_i^l - f_i^{l-1}|^2}{\sum_{i=1}^N |f_i^{l-1}|^2}} \times 100, \quad l = 2, 3, \dots, L. \quad (3.4)$$

Normally, the accuracy is acceptable since  $E_l$  is smaller than or equal to 1.0%. Therefore, if a mesh which have the  $E_l$  between two level of the mesh is smaller or equal to 1.0%, it can be used for the next simulation.

### ***3.2.2 The grid information and model set-up***

The present research investigates the convergence of the grid by using seven meshes ( $L = 7$ ). The shape of the domain is similar to the shape of the domain in the contraction experiment (Experiment 2(b)) (Fig. III-1(d)). The maximum and minimum width are 500 m and 155.0 m, respectively. The length of each mesh is about 70 km and the vertical grid size ( $\Delta z$ ) varies from 30 cm to 55 cm. The bottom elevation is constant at -14.5 m. Our investigation focuses on the region in the distance of  $15.0 \text{ km} < x \leq 25.0 \text{ km}$  where the salt tip is observed after one tidal cycle simulation. We investigate at ten locations for each region ( $N = 10$ ). In the distance of  $15 \text{ km} < x < 22 \text{ km}$ , the length of the cell varies gradually from 100 m to 10 m over seven meshes. In the other regions in the domain, the grid spacing doesn't change. The grid spacing of the coarsest and the finest mesh (length of one edge in a triangle) is about 229 m and 10 m, respectively. More information of the seven meshes are shown in detail in Table 1 and the figures of the meshes are shown in Fig. III-3(a)-(d).

**Table 1** The mesh information

Grid normalized ( $G_i$ )	Length of edge (m)	Number of the horizontal grid cell ( $M_i$ )	Number of the observation points ( $N$ )	Total time simulation in Chundoong (hours)
1	100	4250	10	0.5
2	80	4968	10	4.0
3	60	7118	10	14.0
4	40	10108	10	40
5	30	13442	10	60.2
6	20	21022	10	82.5
7	10	48574	10	120

For each simulation, the average amplitude of the tide ( $\eta_o$ ) is set at 0.25 m. The time step requires to get an agreement results that is 0.1 s. We use the most common tidal type that is the semi-diurnal tide for all simulations. The constant freshwater runoff at the upstream boundary is at 0.1 m/s. Table 1 shows that the total simulation time in Chungdoong server for five tidal cycles simulation increases when the number of the cells in each mesh increases. The simulation times for the coarse mesh such as for grid 1 to grid 2 are very short (< 5 hours). However, since the number of the cell grid increases, the total time for simulation increases significantly. For the finest mesh ( $G_7$ ), the total time requiring a tidal cycle simulation is about 120 hours.

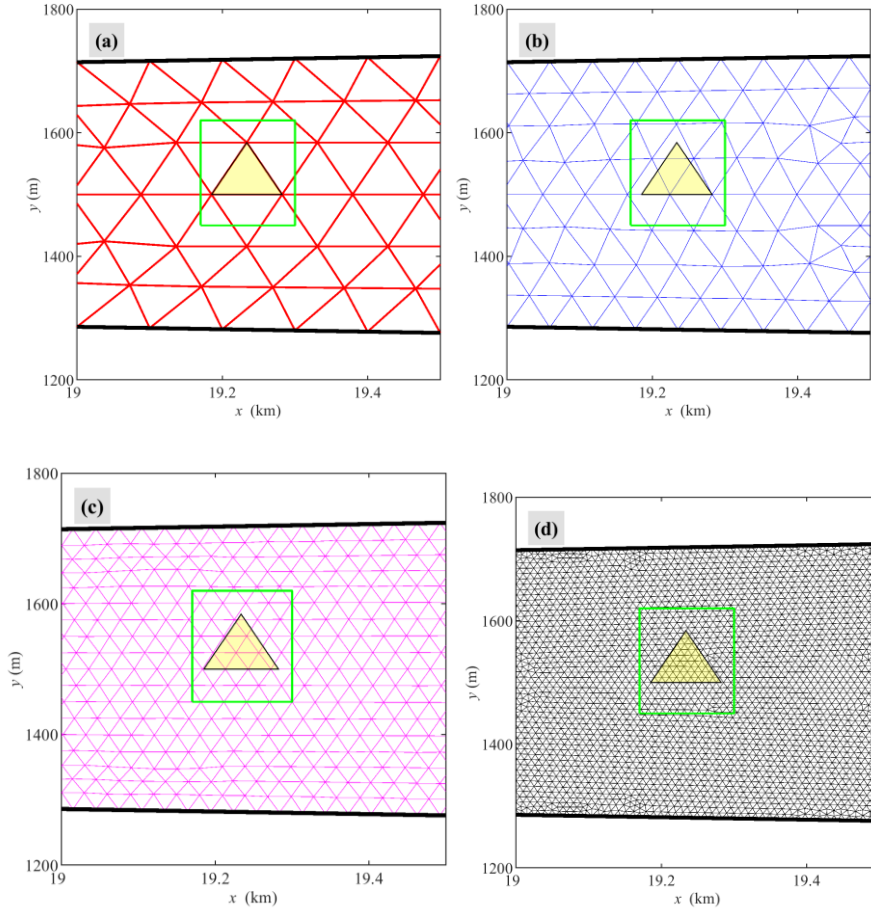


**Fig. III-3** The structure of the meshes used for grid convergence investigation. (a) The grid structure for  $G_1$  ( $\Delta x = 100$  m); (b) The grid structure for  $G_3$  ( $\Delta x = 60$  m); (c) The grid structure for  $G_5$  ( $\Delta x = 30$  m); (d) The grid structure for  $G_7$  ( $\Delta x = 10$  m).

First, the scalar value of the observation points for mesh 1 ( $f_i^1$ ) is computed directly from the model result. More detail, the  $f_i^1$  equals the scalar value of the triangle (just for mesh 1) which has the area overlapping this observation point (Fig. III-4(a)). For the other meshes ( $G_2, G_3, \dots, G_7$ ), the  $f_i^1$  is computed by the area weighted method shown by the following formula:

$$f_i^l = \frac{a_1}{a_0} s_1 + \frac{a_2}{a_0} s_2 + \dots + \frac{a_Z}{a_0} s_Z, \quad (4.4)$$

where  $a_0$  is the area of a triangle covering the location  $i^{\text{th}}$  of mesh  $G_1$ . The  $a_1, a_2, \dots, a_Z$  are the areas of triangle for mesh  $G_3$  overlapping the triangle of mesh  $G_1$  ( $a_1 + a_2 + \dots + a_Z = a_0$ ). The  $s_1, s_2, \dots, s_Z$  are the scalar values of the triangles which have a part or all area overlapping the triangle of  $G_1$ . For instance, at the observation point 5 ( $i^{\text{th}} = 5$ ), four triangles in mesh  $G_3$  overlapping the triangle in mesh  $G_1$  ( $Z = 4$ ) are observed (Fig. III-4(b)). Therefore, the scalar value  $f_5^3$  for mesh  $G_3$  is determined by the below formula:

$$f_5^3 = \frac{a_1}{a_0} s_1 + \frac{a_2}{a_0} s_2 + \frac{a_3}{a_0} s_3 + \frac{a_4}{a_0} s_4, \quad (4.5)$$

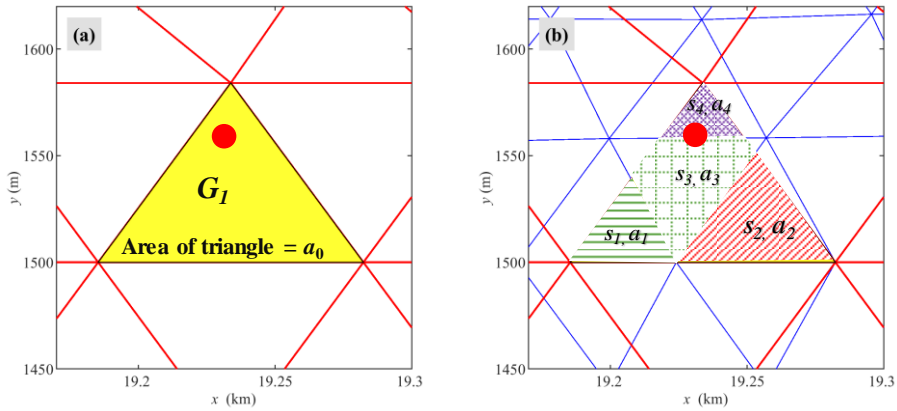


**Fig. III-4** The illustration for the method of calculating the scalar value of  $f_i^l$  (equation (3.5)). (a) For  $G_1$  ( $\Delta x = 100$  m); (b) For  $G_3$  ( $\Delta x = 60$  m). Red point indicates the location of the observation point  $i^{\text{th}}$ . Red line shows the edge of the mesh 1 ( $G_1$ ) and blue line shows the edges of the mesh 3 ( $G_3$ ).

### 3.2.3 The convergence of the grid

In order to demonstrate the independence of the grid, the Root Mean Squared Error ( $RMSE$ ) and  $E_I$  are carried out for salinity concentration value, respectively. The salinity results at ten observation points around the salt tip are observed after the one day ( $t/T = 2$ ). We observe the accuracy of the grid at four location of the water depth. The results show that the error between two grids for four layers decreases when the number of cells increases (Fig. III-5(a)-(d)). The tendency of the error in the plots (Fig. III-5) seems to decrease to zero when the number of the cell in the mesh increase. Therefore, we can conclude that the numerical result is converged when the size of the cell decreases.

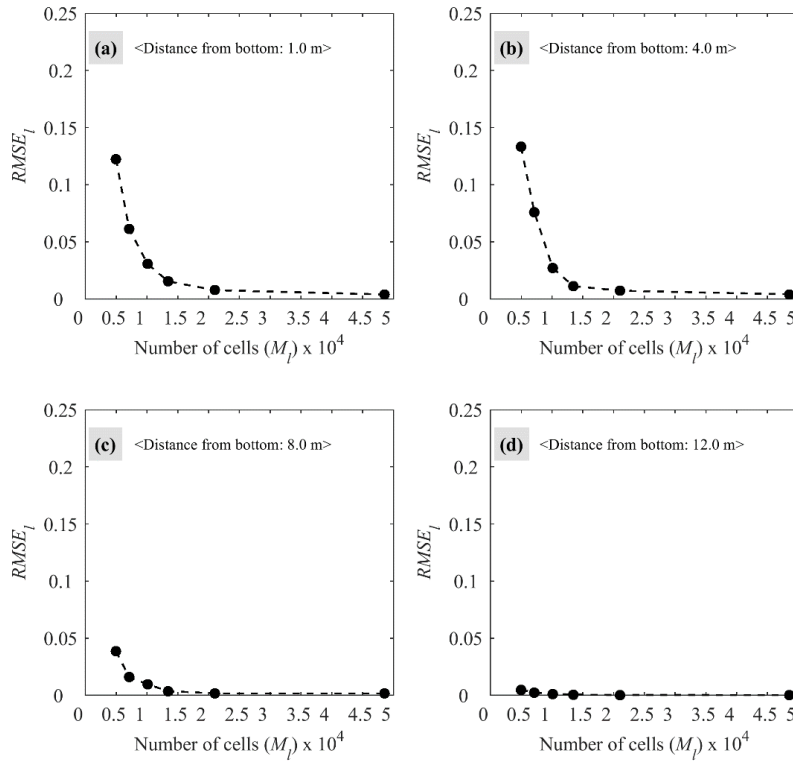


**Fig. III-5** The number of the cells vs  $RMSE_I$  for four vertical locations. (a) at 1.0 m distance from the bottom; (b) at 4.0 m distance from the bed; (c) at 8.0 m distance from the bed; (d) at 12.0 m distance from the bed.

Further, we investigate the accuracy of the mesh by using the equation 3.3. Fig. III-6 shows that the  $E_I$  of the last three meshes ( $G_5$ ,  $G_6$ ,  $G_7$ ) are smaller than 1.0%. Therefore, among the seven observations (Fig. III-6(a)-(d)), the accuracies of resolution for the last three meshes ( $G_5$ ,  $G_6$ ,  $G_7$ ) are acceptable. Moreover, Fig. III-7 shows that when the number of the cell increases, the relative errors between two meshes decrease, and this is mostly a linear relationship. Therefore, we can assume that the mesh is converged.

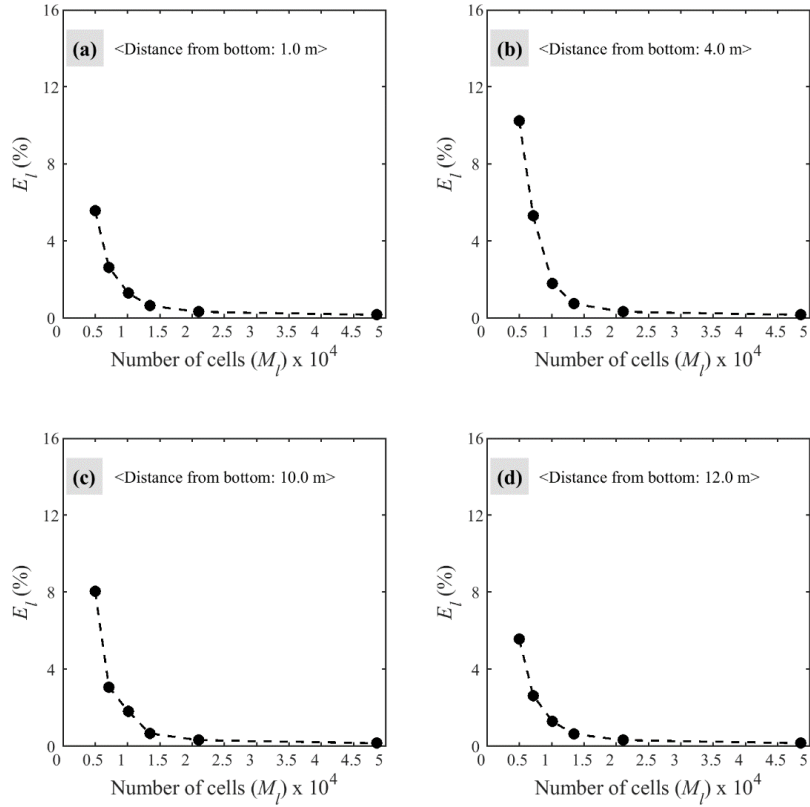


**Fig. III-6** The number of the cells vs  $E_I$  for four vertical locations. (a) at 1.0 m distance from the bottom; (b) at 4.0 m distance from the bed; (c) at 8.0 m distance from the bed; (d) at 12.0 m distance from the bed.

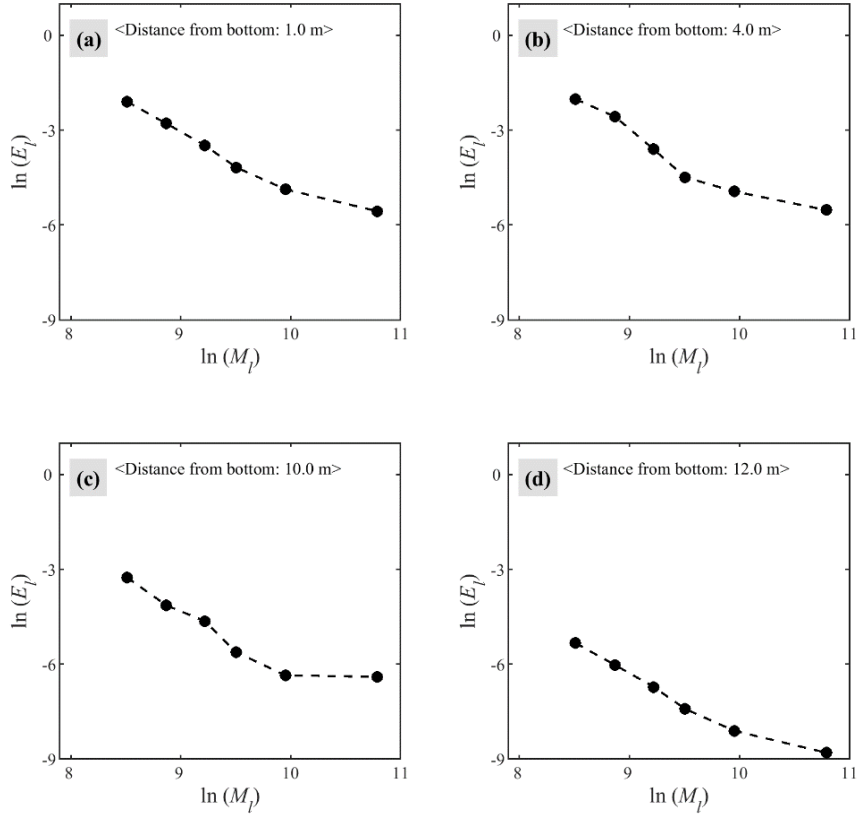


**Fig. III-7** The number of the cells vs  $\ln(E_l)$  for four vertical locations. (a) at 1.0 m distance from the bottom; (b) at 4.0 m distance from the bed; (c) at 8.0 m distance from the bed; (d) at 12.0 m distance from the bed.

### 3.2.4 Summary

The above investigation shows that the numerical results are converged if the number of cells in the mesh increases. The accuracy of the model may be independent on the horizontal resolution from mesh  $G_3$ . ( $\Delta x \geq 60$  m). In the present work, we will use the mesh with the grid size in the range between 50 m and 6.0 m for the next simulations.



## **CHAPTER FOUR**

### **IV. THE EXISTENCE OF THE OVERTURNS ON THE MILD SLOPE AND THEIR EFFECTS**

#### **4.1 Introduction about the existence of the overturn**

The overturns have been observed in the nearshore coastal regions where the bottom slope is significant (Petruncio et al. 1998; Masunaga et al., 2015; Wang et al. 2008). However, the results from the several works (e.g., Sanford et al. 2001, North et al. 2004, and Kim et al. 2007) show that the overturns seems to even exist on the mild slope around the salt tip where the tidal flows directly interact with the river flows. Evenly, on the mild slope, the overturns seem to influence on the mixing and the sedimentary processes. However, the existence of the overturn at the salt tip and their effects have not been studied or investigated further.

Therefore, to confirm that the overturns at the salt tip may develop in the mild slope region and the bottom slope is an essential condition for the development of the overturn, we respectively investigate the processes in the salt tip for two kinds of the bottom that are: the flat bottom (experiment 1) and the slope bottom (experiment 2). In which, the bottom slope used in experiment 2 is setup mimic the slope of the upstream of the Chesapeake Bay. In order to clarify the existence of the overturns and their effects, the flows and density structures as well as the sediment processes around the salt tip over the tidal cycle in both two cases will be respectively analyzed.

## 4.2 Model setup and data output

In this chapter, three study cases in two experiments are respectively investigated (Table 2). In the first case (experiment 1), the width of the domain is constant at 500 m and the bottom elevation is at -14.5 m for the whole domain as the non-geometry case (Fig. III-1(a)). In the second experiment, we investigate two study cases (case 2 and case 3) and the bottom elevation in both two cases varies significantly in the distance from  $x = 10$  km to 20 km. The change of the bottom elevation in experiment 2 is following Equation (3.1).

In case 2, the domain is designed to a very narrow domain ( $W = 6.0$  m) (Fig. III-1(b)) as 2D model simulation to the overturn be observed in high resolution. The other case of the bottom slope experiment was designed to a narrow domain with 500 m width of the channel (3D model) (Fig. III-1(c)). In three study cases, the average amplitude of the tide ( $\eta_0$ ) is set at 0.5 m, and the current at the river boundary condition ( $u_0$ ) is set at 0.1 m/s. Besides, the other information about model setup for three cases was introduced in section 3.1 and table 2.

Table 2 The study cases for the effects of the bottom slope investigation

Name of study case	Width of domain ( $W$ )	The grid size ( $\Delta x$ )	Boundary condition for $\eta_0$	Boundary condition for $u_0$	Characteristics	Short name of the experiment
Case 1	500 m	20 m	0.5 m	0.1 m/s	Without the effects of the geometry	Non-geometry
Case 2	6.0 m	6.0 m	0.5 m	0.1 m/s	Includes the effect of nonhydrostatic pressure, medium tidal amplitude.	Bottom slope, 2D
Case 3	500 m	42 m	0.5 m	0.1 m/s	Includes the effects of the lateral flow.	Bottom slope, 3D

The vertical grid sizes used in three study case vary from 9 cm to 30 cm. The horizontal grid size in the mesh of the case 1 (Non-geometry case) is constant at 20 m. The grid size of the meshes used in case 2 are 6.0 m as 2D model. For 3D model (case 3), the grid size used is about at 42 m. The grid size for 3D model is referenced from Masunaga et al (2007)'s work whom use 100 m grid size to investigate the existence of the internal bore on the coastal region. Besides, with this size ( $\Delta x = 42$  m), the SUNTANS model releases the reliable results because it is smaller than the reliable grid size which was chosen by the convergence test with several sizes of grid ( $\Delta x < 50$  m). Since the thickness of the upper layer ( $D_1$ ) predicted from the two experiments near the end of the salt tip varies from 10 m to 12 m (section 3.2), the grid size of 6.0 m is suitable in order to the nonhydrostatic pressure be effective. The condition for the effects of the nonhydrostatic pressure is shown by below formula (Griffies et al., 2000)

$$\lambda = \frac{\Delta x}{D_1} < 1. \quad (3.1)$$

All study cases are simulated for five tidal cycles. After two tidal cycles, the salt head seems to stay and move back and forth in the similar region, where the bottom elevation changes significantly ( $10 \text{ km} \leq x \leq 25 \text{ km}$ ) and so the results from periods of 2 to 4.5 are used for the analysis. In outputs from the SUNTANS used in this chapter include: salinity concentration, sediment concentration, the turbulent velocity scale ( $q$ ), the turbulent length scale ( $l$ ). Besides, three component of the velocities ( $u, v, w$ ) are used.

### **4.3 The structure of the flow and the sedimentary transport processes in the upstream of the estuary with the flat bottom and the constant width (non-geometry)**

#### ***4.3.1 The structure of the salt tip in two flow modes***

The thesis starts with investigating the processes in the non-geometric estuary (case 1). In 1.5 tidal cycle ( $2.5 < t/T \leq 4.0$ ), the salt tip for case 1 seems to be exist from  $x = 14$  km to  $x = 24$  km. The locations of the salt tip in that distance are found from the results of the tidally averaged sediment concentration and the streamwise gradient salinity presented in Fig. IV-1(a)- (b).

Fig. IV-1(a) shows that the distance from the near river boundary ( $x = 0$ ) to  $x = 15$  km is the freshwater where the highest sediment concentration is observed ( $\bar{C} = 0.15$  kg/m<sup>3</sup>). The distance of  $22 \text{ km} < x \leq 70 \text{ km}$  is the downstream of the salt tip since in this region because the sediment concentration is smallest ( $\bar{C} \approx 0.01$  kg/m<sup>3</sup>). According to Geyer (1993), the sediment is significantly resuspended in the freshwater region, and in the salt water region the resuspension process of the sediment is limited by the stratification. Therefore, the region in distance of  $15 \text{ km} < x \leq 22 \text{ km}$  is the transition region where the salt tip starts and affect to the suspended sediment processes and the sediment concentration in this region significantly decreases between  $0.15 \text{ kg/m}^3$  and  $0.01 \text{ kg/m}^3$  (Fig. IV-1(a)).

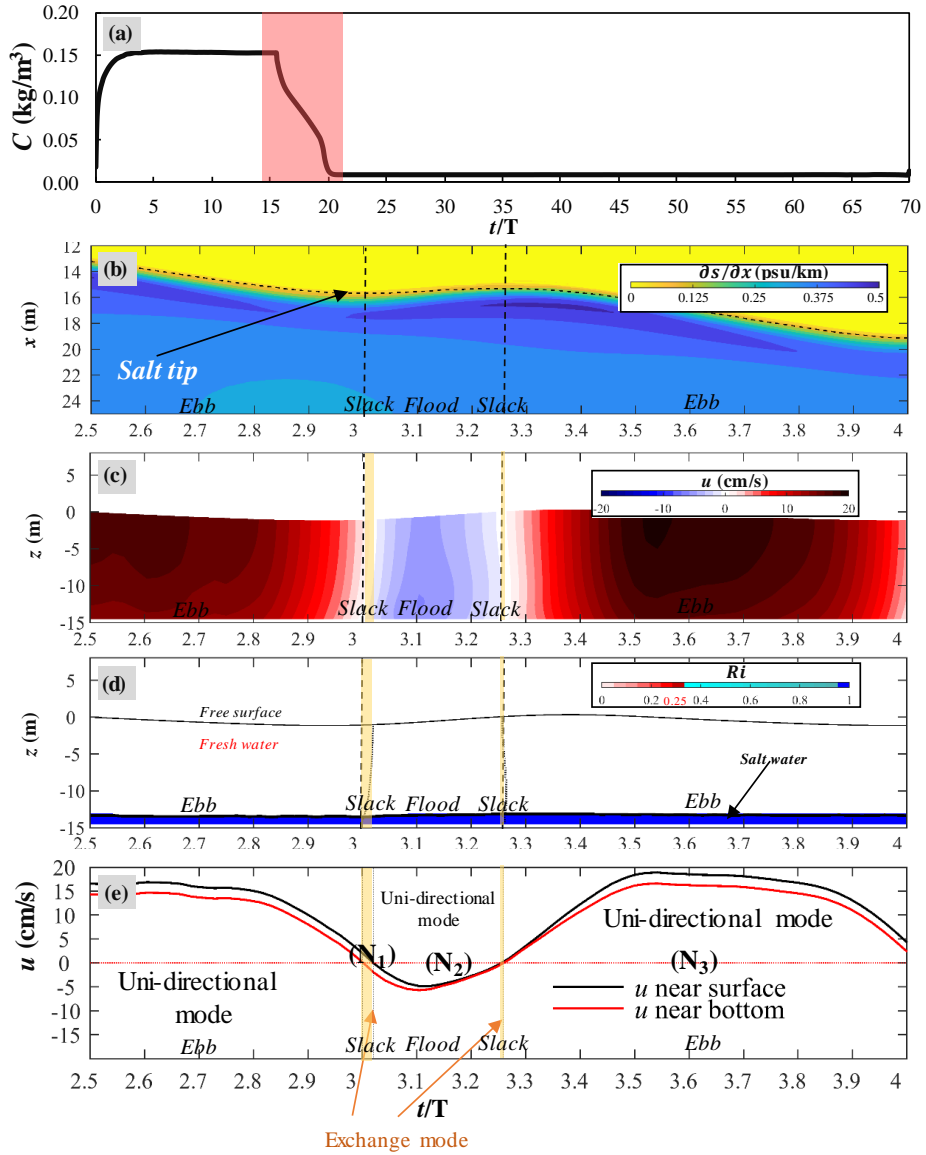


**Fig. IV-1** The tidally averaged sediment concentration, the streamwise salinity density gradient, the vertical distribution of the streamwise flow at the salt tip, gradient Richardson number for salt layer and the flow modes from the profile of the velocity magnitudes near surface and near bottom for case 1 (Non-geometry case). (a) The tidally averaged sediment concentration near the bed (kg/m<sup>3</sup>) for a 70 km distance from the upstream to the downstream. (b) The salinity density gradient (psu/km) near the bed around the salt head, (c) The vertical profiles of  $u$ -velocity (cm/s) at locations of the salt head, (d) the gradient Richardson number for salt layer, (e) the flow modes from the files of the velocities near surface and near bottom (cm/s). The black dotted line in (d) shows the location of the flow interface.

The exactly locations of salt tip in the distance of  $15 \text{ km} < x \leq 20 \text{ km}$  can be identified from the results the streamwise gradient salinity distribution ( $\partial s / \partial x$ ) shown in Fig. IV-1(b). The salt front is observed from the locations where the salinity concentrations change notably within a relatively short distance. Fig. IV-1(b) show that in 1.5 tidal cycle, the salt tip fluctuates in 5 km from  $x = 13 \text{ km}$  to  $x = 18 \text{ km}$  and the variation of the salt tip location depends on the tidal phases.

The tidal phases telling whether flood, ebb and slacks are determined in a Lagrange way by using the results of  $u$ -velocity at the salt tip (front) (Fig. V-1(c)). Flood is determined for a period when  $u$  at the water surface above the salt tip becomes negative (toward  $x = 0 \text{ m}$ ) and ebb begins at a time when  $u$  at the surface changes to be positive toward downstream. For example, in Fig. V-1(c),  $u$  changes the sign to negative at  $t/T=3.0$ , and from this time we can say the flow is in flood. At that time the salt tip is located at  $x = 15.85 \text{ km}$  (Fig. V-1(b)). The flow turns to the ebb at  $t/T=3.28$  (Fig. V-1(c)) and at that time the salt tip is located at  $x = 15.8 \text{ km}$  (Fig. V-1(b)) and the ebb period ends at  $t/T=4.0$  and the salt tip is at  $x=18.0 \text{ km}$ .

However, at any time in ebb phase or flood phase, the flows in the salt layer are in the strong stratification. Fig. V-1(d) show that over 1.5 tidal cycle, the  $Ri$  number for the salt layer is bigger than 1.0. The large gradient Richardson number is evenly observed when the flow mode at the salt tip are bidirectional (Fig. V-1(d)).

The exchange flow just occurs during the slack before flood ( $3.0 < t/T \leq 3.03$ ) or slack after flood ( $3.27 < t/T \leq 3.28$ ) and during these periods, the surface  $u$ -velocity is positive while the near bottom  $u$ -velocity is negative (Fig. V-1(e)). While the bidirectional mode exists in the short time ( $t/T \leq 0.03$ ), the uni-directional flow is dominant during the periods of the ebb ( $t/T \leq 3.0$  or  $t/T \geq 3.28$ ) and the flood of  $3.03 < t/T \leq 3.27$  (Fig. V-1(e)). Fig. V-1(e) show that the almost time during ebb or the flood, the  $u$ -velocities near surface and near bottom are same positive or same negative.

To clarify the differences in the flow and salt front structures between the unidirectional mode and the exchange mode (for case 1), we investigate the vertical distributions of the flows and vertical distribution of the salinity in 10 km distance at the time moments of  $t/T=3.02$ ; 3.15; 3.60, marked from ( $N_1$ ) to ( $N_3$ ) in Fig IV-1(e). Time ( $N_1$ ) and time ( $N_3$ ) are at ebb phase when the flow is near the end of the ebb ( $3.02 t/T$ ) and near full flood ( $3.60 t/T$ ), respectively. While the flow at time ( $N_1$ ) is in the exchange flow mode, the flow at time ( $N_2$ ) is in the uni-directional mode. The time ( $N_3$ ) is near full flood and at that time, the flow is in the uni-directional mode. The results of the flow structures and salinity distribution around the salt tip at three times are presented from Fig IV-2(a) to Fig IV-2(k).

In which, Fig. IV-2(a) shows that at time ( $N_1$ ), the salt tip locates at  $x = 15.85$  km and from that location to the downstream, the two-layer flow is absolutely observed. However, the longitudinal velocity near the bottom gradually decreases from  $x = 20$  km to the salt tip without any convergence observed. The vertical flow at this time is very slow ( $|w| < 0.01$  cm) Fig. IV-2(b)

and the thickness of the salt layer slightly decreases from the downstream to the end of the salt tip at ( $x = 15.85$  km) (Fig. IV-2(c)). Fig. IV-2(a)-(c) shows that the overturn and internal bore structure is not observed in case 1 (Non-geometry effect case).

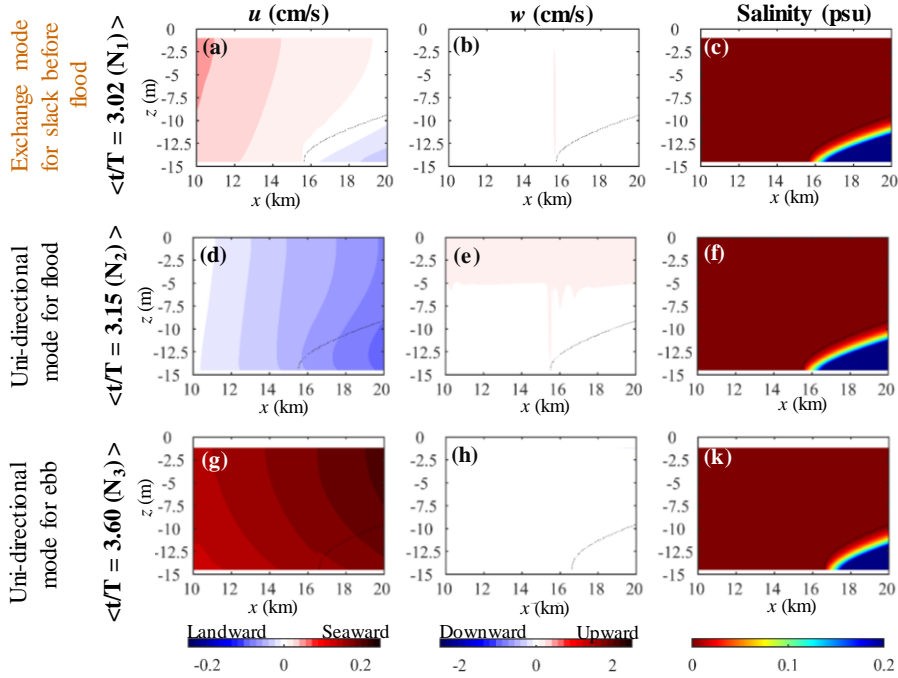


**Fig. IV-2** The distribution of the two velocity components ( $u$ ,  $w$ ) and the salinity concentration in the 10 km longitudinal cross-section of the salt tip at time ( $N_1$ ), ( $N_2$ ), ( $N_3$ ) in experiment 1 (Case 1) (Non-geometry effect). The small black dotted line is the contour of 0.005 psu salinity, separating domain into two zones, the left side is freshwater zone, the right size is saltwater zone. Yellow areas show the exchange mode.

At time ( $N_2$ ), the water flows to mainly upstream for whole water depth formatting for the uni-directional flow mode, and the vertical flow is slow ( $|w| < 0.01$  cm/s) (Fig. IV-2(d)-(f)). Fig. IV-2(f) shows that the variation of thickness of the salt layer from the downstream to  $x = 15.8$  km (salt tip) is similar



to that in the previous step (Fig. IV-2(c)). At the uni-directional mode for ebb (time ( $N_3$ )), the ebb flow is dominant and the vertical flow is small ( $|w| < 0.005$  cm/s) in 10 km distance from  $x = 10$  km to  $x = 20$  km (Fig. IV-2(g)-(h)). Fig. IV-2(k) shows that the structure of the salt layer at that time seems to be similar to the structure of the salinity in previous periods (Fig. IV-2(c) and (f)).

#### ***4.3.2 The suspended sedimentary processes***

In order to clarify the sedimentary process in two flow mode for the non-geometry case, the distribution of the suspended sediment and the size of the sediment fluxes at three moments in case 1 (time ( $N_1$ ) – ( $N_3$ )) are investigated. The results of the sediment processes for case 1 is presented in Fig. IV-3. Fig. IV-3 shows that the concentration of the sediment from the salt tip to the downstream is far smaller than that in the upstream region of the salt tip where the fresh water is dominant. According to Geyer (1993), under effects of the bottom shear stress, the sediment is strongly resuspended from near the bottom into the water column in the fresh water. Therefore, at three moments, the sediment the higher concentrations of sediment are just observed at the fresh water region (Fig. IV-3(a)). From the salt head to the downstream, the salt flows are in the stratification ( $Ri > 1$ , (Fig. IV-3(d))) and the stratification suppress resuspension processes leading to the sediment concentration from the in the freshwater layer is far smaller than the sediment concentration in the region from the salt head to upstream. In the exchange mode for slack before flood (time ( $N_1$ )), the main direction of the resuspended sediment transport is downstream with the slow speed (Fig. IV-3(a)). In contrast, the sediment is transported to the upstream when the flow is in the uni-directional mode for flood (time ( $N_2$ )) (Fig.

IV-3(b)). Finally, at time ( $N_3$ ), the sediment in case 1 is transported to landward (Fig. IV-3(c)).

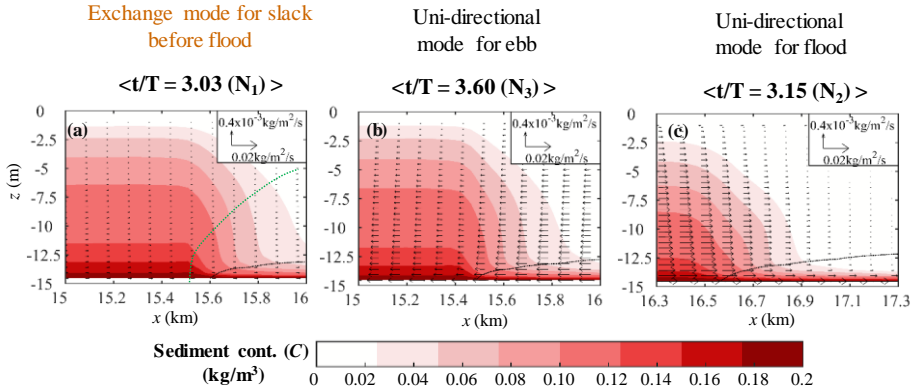


**Fig. IV-3** The suspended concentration ( $C$ ) with the sediment flux vectors in a 1.0 km longitudinal cross-section of the salt tip for case 1 at time ( $N_1$ ) – ( $N_3$ ). The small black dotted line is the contour of 0.005 psu salinity, separating domain into two zones, the left side is freshwater zone, the right size is saltwater zone. The small blue dotted line show the locations of the interfacial flow layers. Time ( $N_1$ ), time ( $N_2$ ) and time ( $N_3$ ) are depicted in Fig. IV-1(e).

Therefore, in a tidal cycle, the salt tip in the non-geometric estuary experiences in two flow modes that are exchange mode and uni-directional mode (Fig. IV-1(e)). In both two flow mode, the magnitude of the vertical flows is small, compared to magnitude of the streamwise flows (Fig. IV-2). Similar to the observation of Geyer (1993), the sedimentary transport processes in the salt tip are driven by the stratification. The sediment near the bottom in the is resuspended in the freshwater region but limited in the salt water regions by the stratification (Fig. IV-3). Especially, the overturn not observed in the exchange flow mode or in the uni-drectional mode (Fig. IV-2).

#### **4.4 The existence of the overturn in exchange flow mode on the mild slope in 2D model**

##### ***4.4.1 The salt tip structure and the existence of the exchange flow***

The overturn structure could not be found in the estuary with the flat bottom and narrow width, but they seem to be found from in the estuary with the mild slope bottom. The results for the estuary with mild slope bottom shows that in particular tidal period, higher concentrations of sediment are observed at the head of the salt wedge (salt tip) (Fig. IV-4(a)-(b)). The such significant rises of the sediment concentration must be related to the existence of the specific flow structures along with geomorphology (Fig. IV-4(a)-(c)).

Fig. IV-4(a) show that tidally averaged concentrations of sediment are much higher in the upstream of the estuary than in the other regions (Fig. V-4(a)). In far downstream from the 21.5 km, the sediment concentrations vary from  $0.012 \text{ kg/m}^3$  to  $0.031 \text{ kg/m}^3$  and the concentrations of sediment  $0.15 \text{ kg/m}^3$  of maximum by 21.5 km from  $x = 0$ , which is about ten times higher than the concentration of the sediment in the downstream ( $x > 21.5 \text{ km}$ ). The maximum concentration is observed at  $x = 18.5 \text{ km}$ , where the head of salt wedge seems to be located in the range of between  $x = 14 \text{ km}$  and  $20 \text{ km}$ .

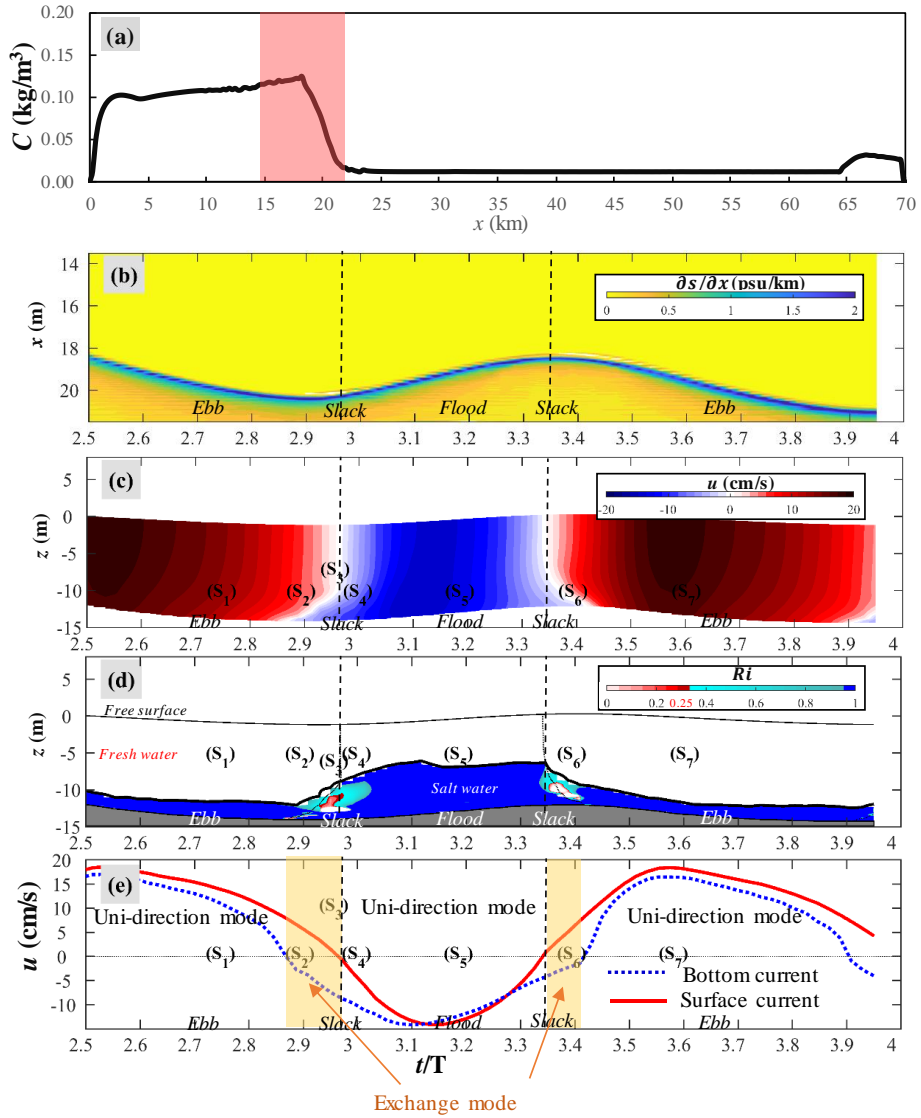


**Fig. IV-4** The tidally averaged sediment concentration, the streamwise salinity density gradient, the vertical distribution of the streamwise flow at the salt tip, gradient Richardson number for salt layer and the flow modes from the profile of the velocity magnitudes near surface and near bottom for case 2 (the bottom slope, 2D model). (a) The tidally averaged sediment concentration near the bed (kg/m<sup>3</sup>) for a 70 km distance from the upstream to the downstream. (b) The salinity density gradient (psu/km) near the bed around the salt head, (c) The vertical profiles of  $u$ -velocity (cm/s) at locations of the salt head, (d) the gradient Richardson number for salt layer, (e) the flow modes from the file of the velocity near surface and near bottom (cm/s). The black dotted line in (d) shows the location of the flow interface.

To identify the presence of the salt tip in that region, the density gradient is computed (Fig. V-4(b)). Fig. V-4(b) shows that during the time from  $t/T=2.5$  to  $t/T=4.0$ , the salt front occurs in a region between  $x = 18.2$  km and  $20.2$  km where the change of the salinity concentration is largest and the bottom changes rapidly (Fig. III-2(b)). Similar to the salt tip in case 1, the locations of the salt tip in case 2 varies depending on the tidal phase.

Similar to case 1, we use the results of the longitudinal velocity at the salt tip in a Lagrange way to determine the tidal phases. Fig. IV-4(c) shows that from  $t/T=2.93$  to  $t/T=3.35$ , the flow is in the ebb since the  $u$ -currents show the positive value. During the ebb of  $2.93 \leq t/T < 3.35$ , the locations of the salt tip varies about  $2.0$  km distance (Fig. IV-4(b)). At  $t/T=2.93$ , the salt tip is located at  $x = 20.15$  km (Fig. IV-4(b)). The flow is in flood phase in the period of  $2.93 \leq t/T < 3.35$  since the streamwise currents shows negative value (Fig. IV-4(c)). At  $t/T=3.35$ , the  $u$  changes the sign to positive when the salt tip is located at  $x = 18.2$  km and from that time the flow is in ebb (Fig. IV-4(b)- (c)).

For 1.5 tidal period, uni-directional flow mode and bidirectional flow mode observed by taking turns and the processes for mixing and sediment transport look very different depending on the modes. Fig. IV-4(d) shows that flow in the salt tip is well mixed at the interface flow ( $Ri \leq 0.25$ ) during the slack before flood ( $2.87 \leq t/T < 2.93$ ) and the slack after flood ( $3.35 \leq t/T < 3.41$ ), and in the other moments over 1.5 tidal cycles, the flow is in strong stratified condition ( $Ri \geq 1$ ). During the slack before flood ( $2.87 \leq t/T < 2.93$ ), the surface current is negative and the bottom current is positive implying for the existence of the bidirectional mode (the exchange flow mode) (Fig. IV-5(e)). Similarly, the

bidirectional mode exists during the slack after flood ( $3.35 \leq t/T < 3.41$ ) since the surface current turns to the ebb phase but the bottom current is still in the flood phase (Fig. IV-4(e)). Excepting the slack before flood ( $2.87 \leq t/T < 2.93$ ) and the slack after flood ( $3.35 \leq t/T < 3.41$ ), the flows near the full ebb or full flood is in the uni-directional flow mode since the  $u$ -currents near the free surface and the bottom boundary at the same moments observed in Fig. IV-4(e) show for same tidal phase.

#### ***4.4.2 The existence of the overturn and the internal tidal bore on the mild slope***

To clarify the differences in the mixing and sediment processes of the bidirectional and uni-directional modes, the structures of flow and the distributions of salinity from case 2 (2D model) are compared at seven instants of  $t/T=2.73$ ; 2.88; 2.94; 2.98; 3.17; 3.38; 3.58, marked from (S<sub>1</sub>) to (S<sub>7</sub>) in Fig IV-4(e). Time (S<sub>1</sub>) and time (S<sub>7</sub>) are at the near end of ebb (2.73  $t/T$ ) and during the ebb (3.58  $t/T$ ) when the flows are in the uni-directional flow mode (Fig IV-4(e)), respectively. The flows at both time (S<sub>4</sub>) and (S<sub>5</sub>) are in the uni-directional flow mode during flood. Times (S<sub>2</sub>), (S<sub>3</sub>), (S<sub>4</sub>) and (S<sub>6</sub>) are near slack before flood and slack after flood respectively and at that moments, the flows are in the exchange mode. The flow structures and salinity distribution at the seven instants around the salt tip are shown in Fig. IV-5.

In Fig. IV-5, the results of the velocity magnitudes and salinity concentration for seven time instants are respectively shown in the figures from the first line to seventh line. The distribution of the streamwise velocity in Fig. IV-5(a<sub>1</sub>) shows that the flow at time (S<sub>1</sub>) is uni-directional mode for the ebb with negative value in the velocity. In the ebb, the vertical flow around the salt tip is

downward with small size ( $|w| < 0.02$  cm/s), compared to the magnitude of the streamwise flow ( $|u| > 15$  cm/s). In the 500 m distance from the downstream to the salt tip ( $x = 19.75$  km), the thickness of the salt layer gradually decrease until to zero (Fig. IV-5(c<sub>1</sub>)).

At time (S<sub>2</sub>), the flood flow appears in the salt from the head of the salt tip to downstream ( $x > 20.5$  km) (Fig. IV-5(a<sub>2</sub>)). As a result, the flow is in the bidirectional mode. At that moment, the vertical currents at the salt head is positive and significant ( $|w| > 0.2$  cm/s), compared with the vertical currents in the previous step (time (S<sub>1</sub>)) (Fig. IV-5(b<sub>2</sub>)). The shape of the salt tip slightly different (Fig. IV-5(c<sub>2</sub>)) from that in the previous step (Fig. IV-5(c<sub>1</sub>)).

Similar to the results at the time (S<sub>2</sub>), the exchange flow mode exists at the time (S<sub>3</sub>) (Fig. IV-5(a<sub>2</sub>) to (c<sub>3</sub>)). At this time, the salt tip is located at  $x = 20.17$  km, and from the salt tip to the downstream, two-layer flows is observed (Fig. IV-5(a<sub>3</sub>)). While the flow in the upper layer is still in ebb phase, the flow in the lower layer is the flood phase. Especially, Fig. IV-5(b<sub>3</sub>) shows that the magnitudes of streamwise currents at the end of the salt tip for both two layers are significant ( $|u| > 5$  cm/s) implying for a convergence of the velocity. At that time (time (S<sub>2</sub>)), the vertical flows at salt tip is significant ( $|w| > 0.5$  cm/s). Further, the distribution of the  $u$ -velocity and  $w$ -velocity in the Fig. IV-5(a<sub>3</sub>) and (b<sub>3</sub>) show for the existence of the big circulation at the salt tip. Under effects of the significant vertical flow at the overturn, the thickness of the salt head increase from 4.0 m to 5.5 m between time (S<sub>2</sub>) and time (S<sub>3</sub>) (Fig. IV-5(c<sub>2</sub>) and (c<sub>3</sub>)).

In a short time after time (S<sub>3</sub>), the flows turn to the uni-directional mode for flood since the  $u$ -current near the surface observed in Fig. IV-5(e) shows

positive value. The overturn flow which is observed the previous time (time ( $S_3$ )) disintegrates when the flow turn to flood because of the disappearance of the bidirectional flow structure. At the beginning of the flood (time ( $S_4$ )) the convergence in magnitude of the streamwise velocity and the significant vertical current at the salt tip are still observed (Fig. IV-5(a<sub>4</sub>) and Fig. IV-5(b<sub>3</sub>)). Compare to the previous time in the slack before flood, the thickness of the salt wedge head at time ( $S_4$ ) is largest (Fig. IV-5(c<sub>2</sub>), (c<sub>3</sub>) and (c<sub>4</sub>)). At time ( $S_4$ ), the thickness of the salt wedge head can get about 38% water depth (Fig. IV-5(c<sub>4</sub>)).

The results of the flows around the salt tip in full flood are shown by the results at time ( $S_5$ ) in group of figures from Fig. IV-5(a<sub>5</sub>) to Fig. IV-5(c<sub>5</sub>). In the flood phase, the flow is upward and slow (Fig. IV-5(a<sub>5</sub>)). The magnitude of the vertical velocity is smaller than 0.02 cm/s and is far smaller than the magnitude of the velocity observed in the slack before flood ( $|w| < 0.5$  cm/s) (Fig. IV-5(b<sub>5</sub>) & Fig. IV-5(b<sub>3</sub>)). The thickness of the salt head decrease 50% in the period between the moment ( $S_4$ ) and moment ( $S_5$ ) (Fig. IV-5(c<sub>4</sub>) & Fig. IV-5(c<sub>5</sub>)).



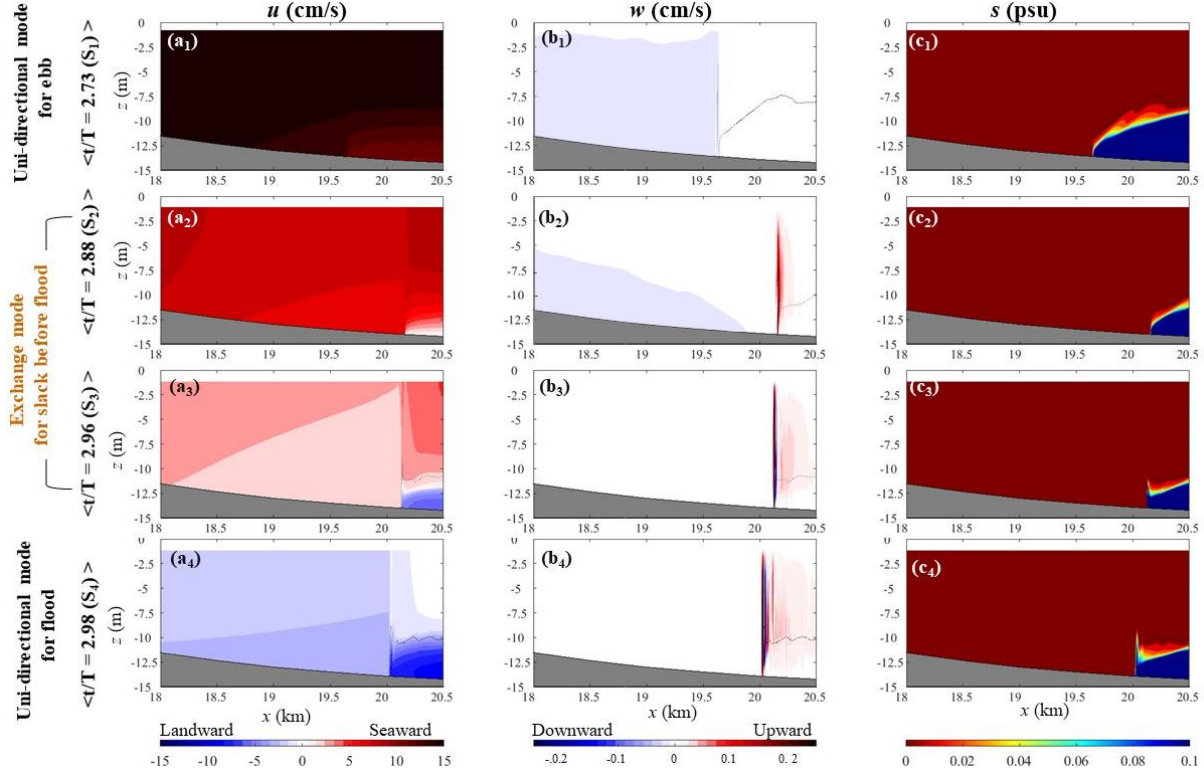


**Fig. IV-5** Distributions of the three velocity components, the distributions of the salinity concentration for the case 2 (2D model) in experiment 1 at time ( $S_1$ ), ( $S_2$ ), ( $S_3$ ) and ( $S_4$ ). Streamwise velocity ( $u$ ), vertical velocity ( $w$ ), salinity concentration ( $s$ ) in the 1.5 km longitudinal cross-section of the salt tip. The small black dotted line is the contour of 0.005 psu salinity, separating the domain into two zones, the left side of the salt tip is the freshwater zone, the other side is the saltwater zone.

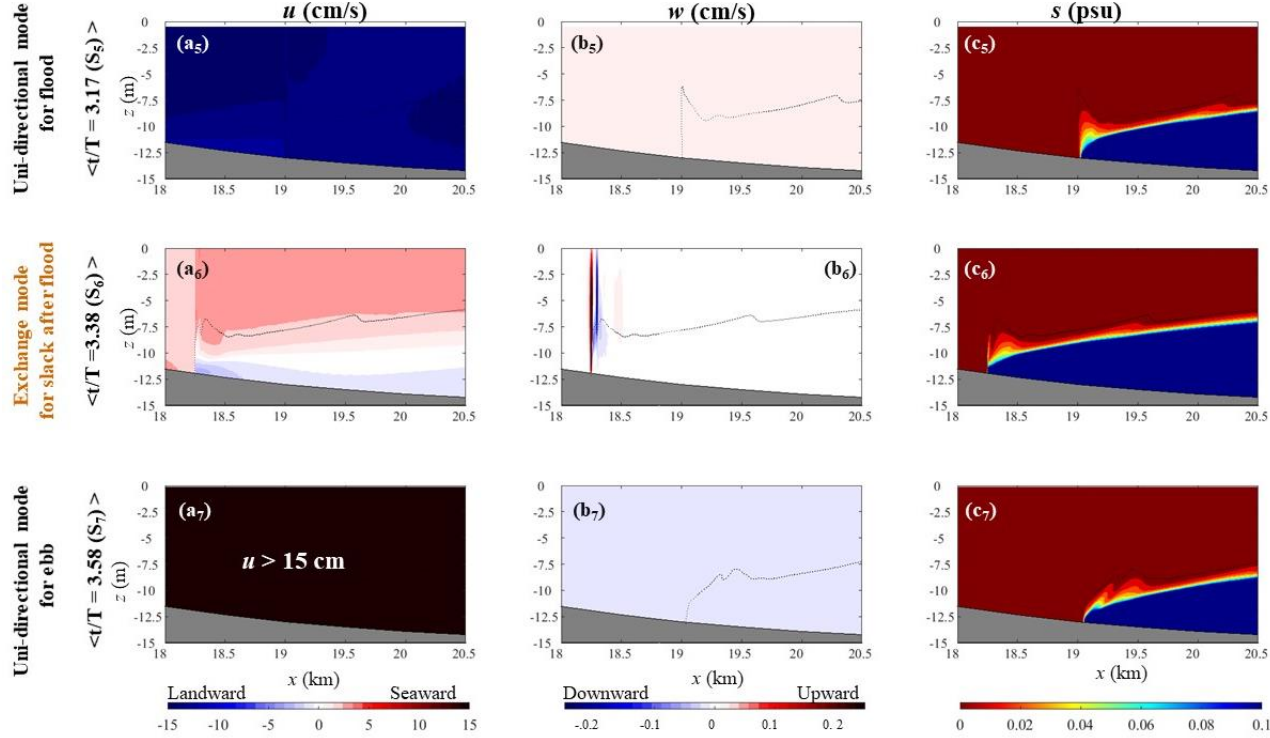


**Fig. IV-5 (cont.)** Distribution of the three velocity components, the distribution of the salinity concentration for the case 2 (2D model) in experiment 1 at time ( $S_5$ ), ( $S_6$ ), ( $S_7$ ). Streamwise velocity ( $u$ ), vertical velocity ( $w$ ), salinity concentration ( $s$ ) in the 1.5 km longitudinal cross-section of the salt tip. The small black dotted line is the contour of 0.005 psu salinity, separating the domain into two zones, the left side of the salt tip is the freshwater zone, the other side is the saltwater zone.

At the end of flood, the unidirectional mode is replaced by the exchange flow mode (Fig. IV-4(e)). During the exchange mode, the overturn exist and its form is similar to the overturn observed in near the end of the ebb case. the size of the  $u$ -current and the  $w$ -current of the overturn at time ( $S_6$ ) are about 3.0 cm/s and 0.15 cm/s, respectively (Fig. IV-5(a<sub>6</sub>) and (b<sub>6</sub>)), and far smaller than those in the slack before flood (Fig. IV-5(a<sub>3</sub>) and (b<sub>3</sub>)). Due to the increased entrainment of the freshwater into salty zone, the salt tip at  $x = 18.3$  km (Fig. V-2(c<sub>6</sub>)) is 1.6 m thicker than at  $x = 19.1$  km (Fig. IV-5(c<sub>5</sub>)).

From time ( $S_6$ ) to time ( $S_7$ ), the thickness of the head of salt wedge decreases since the flow is in the unidirectional mode for ebb. The time ( $S_7$ ), in the ebb period of  $t/T = 3.58$ , the ebb current is strong with  $|u| > 15.0$  cm/s (Fig. IV-5(a<sub>7</sub>)). The vertical flow is downward with the small size (Fig. IV-5(b<sub>7</sub>)). From  $t/T = 3.38$  (time ( $S_6$ )) to  $t/T = 3.58$  (time ( $S_7$ )), the salt tip retreated by 0.8 km to downstream and its thickness decreasees to 2.5 m (Fig. IV-5(c<sub>6</sub>) & Fig. IV-5(c<sub>7</sub>)).

Fig. IV-5 shows that the structure of flows in the bidirectional mode is far different from the uni-directional mode. For the unidirectional mode, the vertical flows in two tidal phases are slow ( $|w| < 0.2$  cm/s) and the longitudinal flow is fast ( $|u| > 15$  cm/s). However, in the exchange flow mode, the vertical flow at the salt tip is significant ( $|w| > 5$  cm/s). The exchange flow appear two times over a tidal cycle and in these period, the internal bore along with overturn flow is observed.

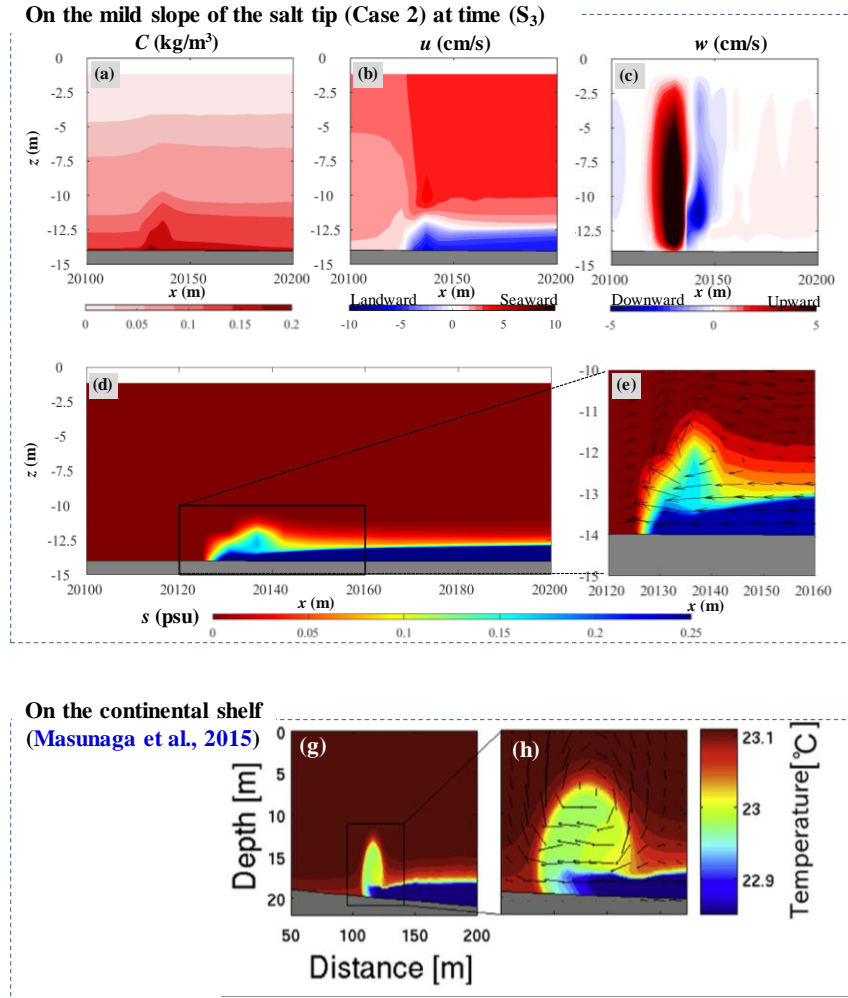


**Fig. IV-6** The sediment concentration, salt tip structure at time ( $S_3$ ) in 100 m distance for case 2 and the structure of the internal bore on the coastal region. (a) Distribution of sediment concentration ( $\text{kg/m}^3$ ); (b) the longitudinal current distribution ( $\text{cm/s}$ ); (c) the vertical current ( $\text{cm/s}$ ); (d) the salinity distribution around the salt tip and (e) the structure of the salt tip with an overturn. (g) and (h) the internal bore and vortex core on the coastal region in Masunaga et al., (2015).

Under existence of the overturn flow, the sediment seems to be highly resuspended. For instance, at time ( $S_3$ ) when the flow is in the exchange mode, the higher concentration of the sediment is observed at near the end of the salt tip ( $x = 20130$  m) (Fig. IV-6(a)). The high concentration of the sediment is located at the place where the longitudinal velocity in the fresh layer and salt layer is converged and the vertical flow is more significant than the other place around the salt tip (Fig. IV-6(b) and (c)). The head of the salt tip at time ( $S_3$ ) appears as a density bore and density bore is along with a vortex core (Fig. IV-6(d) and (e)). The bore with an overturn on the mild slope in the salt tip seems to be a kind of hydraulic jump as a shock process since it is similar to the internal bore with a vortex observed on the coastal region (Fig. IV-6(g) and (h)) (Masunaga et al., 2015).

## 4.5 The existence of the overturn in exchange flow mode on the mild slope in 3D model

### 4.5.1 The salt tip structure and the existence of the exchange flow

The internal bore with overturn is observed in the exchange flow mode not only in the 2D model but also in 3D mode where the lateral component is obtained in the simulation. For 3D model (case 3), in order to clarify the existence of the exchange mode, the surface current, the bottom current as well as the gradient Richardson number along the salt head (Lagrangian way) are investigated and compared together. Fig. IV-7 shows that the flows at the salt tip are in ebb phase in the periods of  $2.5 < t/T \leq 3.0$  and  $3.4 < t/T \leq 4.0$  since the velocity near the surface shows positive value (Fig. IV-7(a)). From  $t/T = 2.87$  to  $t/T = 4.0$ , the flow is in flood because of the negative surface current (Fig. IV-7(a)).

Fig. IV-7(a) shows that during the period of  $3.0 < t/T \leq 3.4$ , the flows are in the uni-directional mode for flood since both the current near the free surface and current near the bottom boundary are negative. The exchange mode for 3D model occurs during the slack before flood ( $2.87 < t/T \leq 3.0$ ) and the slack after flood ( $3.4 < t/T \leq 3.46$ ), and during these moments the bottom  $u$ -current is positive for ebb phase but the surface  $u$ -current is in negative for flood phase (Fig. IV-7(a)). During the period of  $2.5 < t/T \leq 2.87$  and of  $3.4 < t/T \leq 4.0$ , the flows are in the uni-directional mode for ebb and during these period, both the  $u$ -surface and  $u$ -bottom currents shows the positive values.

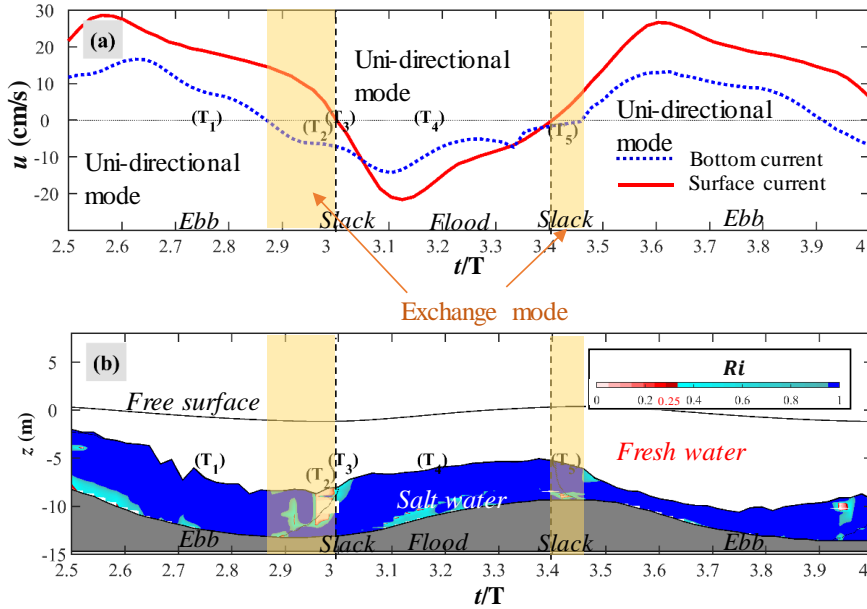


**Fig. IV-7** The profile of the streamwise velocity at the salt tip near the free surface and near the bottom boundary and the vertical distribution of the gradient Richardson number for salt layer in case 2 (the bottom slope, 3D model). (a) The vertical profiles of  $u$ -velocity (cm/s) at locations of the salt head, (d) the gradient Richardson number for salt layer. The black dotted line in (b) shows the location of the flow interface.

Besides, the periods for the existence of the exchange flow mode coincides with the time when the strong mixing in the water column of the salt layer is observed. In the exchange flow mode for slack before flood ( $2.87 < t/T \leq 3.0$ ) or slack after flood ( $3.4 < t/T \leq 3.46$ ), the gradient Richardson number at the interface of the flow shows the small value ( $Ri < 0.25$ ) indicating for the strong mixing (Fig. IV-7(b)). In the other period of 1.5 tidal cycle, the flow at the salt tip tend to be stratified since  $Ri$  is large than 0.25 (Fig. IV-7(b)).

#### 4.5.2 The existence of the overturn and the internal tidal bore

To clarify the differences in salt tip structures between the bidirectional and unidirectional modes for 3D model, the structures of flow and salinity are investigated and compared at five times that are:  $t/T=2.75; 2.96; 3.00; 3.17; 3.42$ , and these time moments are marked between  $(T_1)$  to  $(T_5)$  in Fig. IV-7(a) and (b). Time  $(T_1)$  is at the near end of ebb ( $2.75 t/T$ ). Time  $(T_3)$  and time  $(T_4)$  are at the early flood ( $3.00 t/T$ ) or the near the full flood ( $3.17 t/T$ ), respectively. At the moments of time  $(T_1)$ ,  $(T_3)$  and  $(T_4)$ , the flows are in the uni-directional mode. At the other moments (time  $(T_2)$  and time  $(T_5)$ ), the flows in the exchange flow mode for slack before flood ( $2.96 t/T$ ) and for slack after flood ( $3.42 t/T$ ), respectively. The flow structures and salinity distribution at the salt tip in 4.0 km distance at the five moments are shown in Fig. IV-8.

The figures in the first line of Fig. IV-8 show the results of the salt tip near the end of ebb at the time  $(T_1)$  when the flow is in the unidirectional mode. The distribution of  $u$ -velocity in Fig. IV-8(a<sub>1</sub>) shows that the water flows to mainly downstream in a uni-directional mode at the time  $(T_1)$ . In Fig. IV-8(b<sub>1</sub>), the flow is very slow ( $|w| < 4 \times 10^{-2}$  cm/s) and vertically downward at the *thalweg* of whole 4 km cross-section. At time  $(T_1)$ , the salt tip locates at  $x = 19.75$  km and that location, the lateral flows are laterally to the sidewall directions (Fig. IV-8(c<sub>1</sub>) and (d<sub>1</sub>)). The maximum size of the lateral flow is about 8.0% the size of the streamwise currents (Fig. IV-8(a<sub>1</sub>) and (d<sub>1</sub>)).



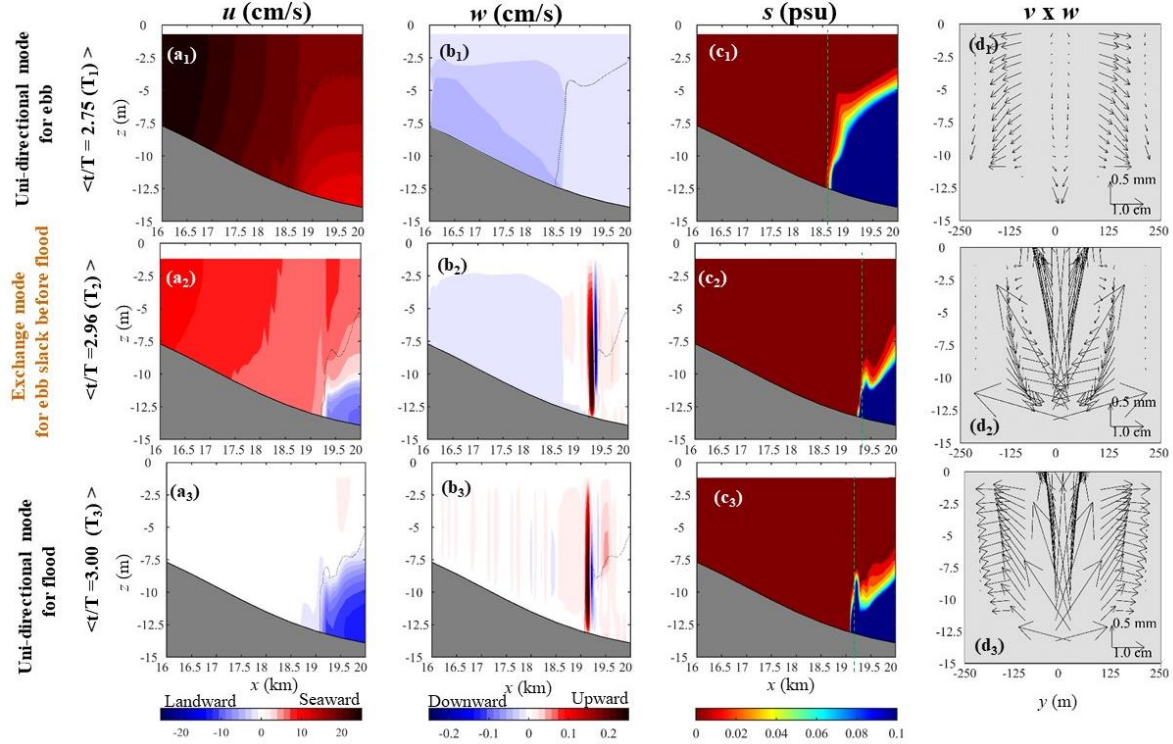


**Fig. IV-8** Distributions of the three velocity components as well as distribution of the salinity concentration for the case 3 in experiment 2 (3D model) at time ( $T_1$ ), ( $T_2$ ), ( $T_3$ ). Streamwise velocity ( $u$ ), vertical velocity ( $w$ ), salinity concentration ( $s$ ) in the 1.5 km longitudinal cross-section of the salt tip and the lateral velocity vectors ( $v \times w$ ) in 500 m transverse cross-section at the salt head (second column). The small black dotted line is the contour of 0.005 psu salinity, separating the domain into two zones, the left side of the salt tip is the freshwater zone, the other side is the saltwater zone. The grey dashed line shows the pycnocline layer. The vertical dotted blue line shows the location for the lateral cross section.

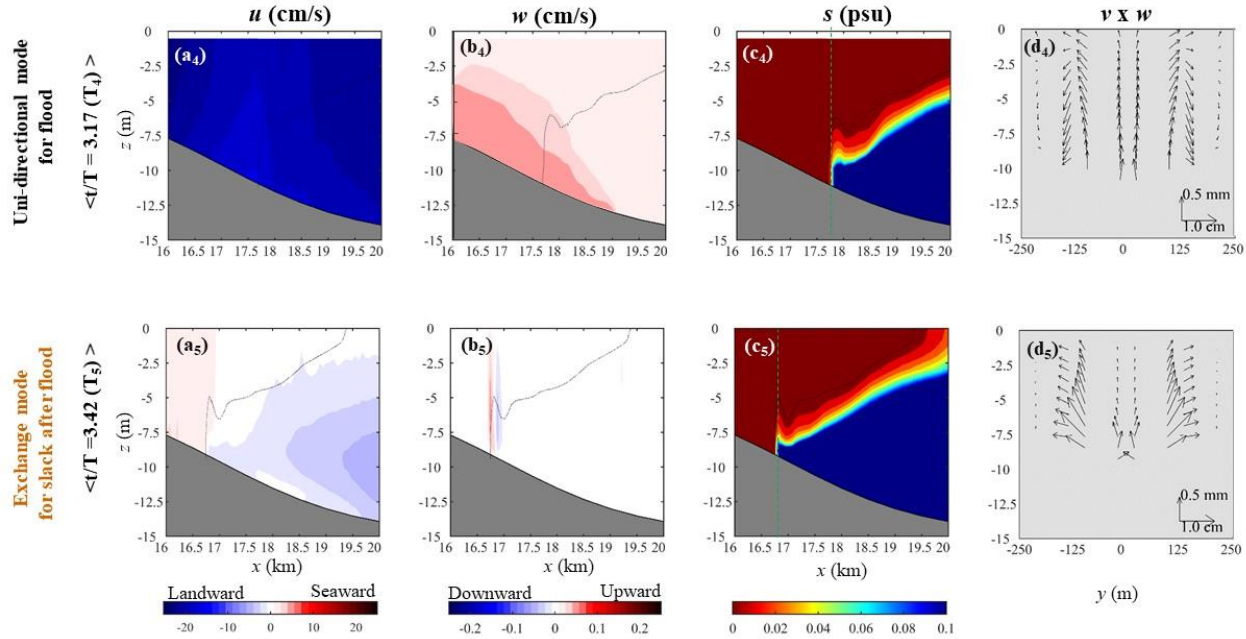


**Fig. IV-8 (cont.)** Distributions of the three velocity components as well as distribution of the salinity concentration for the case 3 in experiment 2 (3D model) at time (T<sub>4</sub>) and (T<sub>5</sub>). Streamwise velocity ( $u$ ), vertical velocity ( $w$ ), salinity concentration ( $s$ ) in the 1.5 km longitudinal cross-section of the salt tip and the lateral velocity vectors ( $v \times w$ ) in 500 m transverse cross-section at the salt head (second column). The small black dotted line is the contour of 0.005 psu salinity, separating the domain into two zones, the left side of the salt tip is the freshwater zone, the other side is the saltwater zone. The grey dashed line shows the pycnocline layer. The vertical dotted blue line shows the location for the lateral cross section.

The shape of the salt tip slightly different and flow structure at time ( $T_2$ ) are far different from that at time ( $T_1$ ) since the flow is in exchange flow mode (Fig.IV-8(a<sub>1</sub>) - (d<sub>1</sub>) and Fig.IV-8(a<sub>2</sub>) - (d<sub>2</sub>)). At time ( $T_2$ ), the salt tip is located at  $x=19.30$  km, and at this location, the water column has two-layers vertically (Fig. IV-8(a<sub>2</sub>)). Both the lower and upper layers have significant increases in the magnitude of  $u$ -velocity ( $|u|>10$  cm/s) at the salt tip (Fig.IV-8(a<sub>2</sub>)). Besides, the flow at salt tip has a strong vertical flow in  $z$ -directions. The maximum magnitude ( $|w|$ ) found in Fig.IV-8(b<sub>2</sub>) is about 0.5 cm/s, and it's could be very helpful for vertical resuspension process of the sediment because that magnitude is 0.7 times bigger than the maximum settling speed of median sediment at the upstream Chesapeake bay estimated by Sanford et al., (2001). Besides, Fig.IV-8(a<sub>2</sub>) and (b<sub>2</sub>) show that there is a vertical circulation existing at the front of the salt tip (the overturning flow), and that circulation seems to mix salinity at the salt tip and also resuspended the sediment. The thickness of the salt head increase 1.5 m for 0.21 periods from time ( $T_1$ ) to time ( $T_2$ ) (Fig.IV-8(c<sub>1</sub>) and Fig.IV-8(c<sub>2</sub>)). Besides vertical flow, the salt tip at the time ( $T_2$ ) has a significant lateral circulation also (Fig.IV-8(d<sub>2</sub>)). Fig.IV-8(d<sub>2</sub>) shows that the currents are divergent near the free surface but convergent near the bottom. The largest magnitude of transverse flows ( $|v|$ ) is approximately 1.4 cm/s and equals up to 14% the size of streamwise flow at the *thalweg*.

The overturning flow, which is observed from the previous time (time ( $T_2$ )), doesn't sustain at the salt tip since the ebb currents near the surface at the salt tip disappear (Fig.IV-8(a<sub>3</sub>) and (b<sub>3</sub>)) as the unidirectional flow mode ( $t/T = 3.0$ ). However, Fig.IV-8(a<sub>3</sub>) show that a signal for an increase in flow magnitude

in the salt layer of the salt head is still observed. Besides, the maximum of the vertical flow at time ( $T_3$ ) is mostly equal to that at time ( $T_2$ ) (Fig.IV-8(b<sub>2</sub>) and Fig.IV-8(b<sub>3</sub>)) and the thickness of the salt tip increases 1.0 m compared to time ( $T_2$ ) (Fig.IV-8(c<sub>2</sub>) and Fig.IV-8(c<sub>3</sub>)). The thickness of the salt wedge head seems to gradually increase from time ( $T_1$ ) to time ( $T_3$ ) and its structure is like a bore, similar to the internal bore observed in case 2 (Fig.V-3(e)) and on the coastal region (Masunaga et al., 2015). At time ( $T_3$ ), the thickness of the salt wedge head can get about 40% water depth (Fig.IV-8(c<sub>3</sub>)). At the salt tip, lateral currents are laterally to the sidewall directions and their magnitude equals about 10% of the size of streamwise currents.

From time ( $T_3$ ) to near the end of the flood ( $3.0 < t/T \leq 3.4$ ), the flow is in the uni-directional mode for flood (Fig. IV-8(a<sub>3</sub>)). At the time ( $T_4$ ) in this period, the landward flows appear on whole water column (Fig.IV-8(a<sub>4</sub>)). The vertical velocity around the salt tip is distributed uniformly with small magnitude ( $|v| < 0.04$  cm/s) which just equals to 8.0% of the maximum vertical velocity in the baroclinic phase (Fig.IV-8(b<sub>2</sub>) and Fig.IV-8(b<sub>4</sub>)). At this moment, the flow structure can be categorized an internal bore which is a kind of shock phenomena after abrupt changes of velocity. The bore seems to decrease its thickness during the uni-directional mode (Fig.IV-8(c<sub>3</sub>) and (c<sub>4</sub>)). Besides Fig.IV-8(d<sub>5</sub>) show the lateral currents at time ( $T_4$ ) flow slowly ( $|v| < 0.05$  cm/s) and the lateral currents at the middle of lateral cross-section ( $y = 0$ ) become divergent and move to the flank of the estuary.

Similar to the case 2 (2D model), the exchange flow for 3D model (case 3) appear in the second time in a tidal cycle and in this flow mode, the internal

bore is observed. Just after the end of the flood, the flows turn from uni-directional mode to exchange flow mode (Fig.IV-8(a<sub>6</sub>)) with very small longitudinal flow. The maximum  $u$ -velocity at the salt tips is just 2.3 cm/s at this moment but this magnitude is still slightly larger than the velocities near outside of the salt tip, and its size is smaller than but its structure is similar to the early flood case (Fig.IV-8(a<sub>6</sub>)). Fig.IV-8(a<sub>6</sub>) and (b<sub>6</sub>) show that the overturning flow exists slightly enhancing the vertical mixing of salinity even though its velocity in the vertical direction is not large ( $|w| < 0.03$  cm/s) compared to the early ebb. And due to the increased entrainment of the freshwater into salty zone, the salt tip at  $x = 16.7$  km (Fig.IV-8(c<sub>6</sub>)) and the thickness is about 9.0 m. For the lateral flows, the lateral flow has the shallower flank direction as in the early flood period (Fig.IV-8(d<sub>6</sub>)).

Fig. IV-8 shows that the structure of flows over ebb and flood in the 3D (case 2) are similar to that in the 2D model (case 1) but in the slightly different size. For the uni-directional mode for ebb, the magnitudes of the vertical and lateral velocities in both that flow modes are too small ( $|w| < 0.04$  cm/s and  $|v| < 0.05$  cm/s, respectively), compared with the significant streamwise velocity ( $|u| > 10$  cm/s). In contrast, the magnitude of lateral flow in exchange flow mode is significant ( $|v| > 1.0$  cm/s), and is more equal than 15% size of  $u$ -currents at that time. Besides, while the size of vertical flow in the uni-directional mode for both ebb and flood from the salt head to upstream is mostly same, the size of vertical flow at the salt tip in the exchange flow mode are far larger than in the other place ( $|w| > 0.5$  cm/s). In the exchange mode, the internal bore with overturn exist, and the existence of the overturn seem to induce for development of the

significant resuspension process of the sediment, compared with flow in the uni-directional mode.

### ***4.5.3 Mixing and sedimentary transport processes***

#### ***4.5.3.1 The mixing process and sedimentary process around the salt tip regions***

The differences of flow structures lead to bigger differences in stratification and sediment transport processes among various phases of tide. Those processes were investigated in ebb, flood and the transition periods (near slack before flood or slack before ebb) by comparing the kinetic energy dissipation rate ( $\varepsilon$ ), the Richardson numbers ( $Ri$ ) and the sediment concentrations ( $C$ ) with its fluxes within 1.0 km distance near salt tips in two modes of flow (Fig. IV-9). Flows are in the uni-directional mode during both flood time ( $T_1$ ) and ebb ( $T_4$ ), and the flow is in the exchange flow mode near the end of ebb, time ( $T_2$ ).

At  $t/T = 2.75$ , the maximum dissipation ( $\varepsilon$ ) is observed with larger than  $10^{6.0}$  W/kg within 0.5 m of thickness near the bottom in the region of  $x > 18.62$  km (Fig. IV-9(a)). In contrast, when the flow is in the exchange flow mode near end of ebb, time ( $T_2$ ), the maximum dissipation rate is observed not near the bottom but at the middle of water column in the range of between  $z = -12.5$  m and  $-10.0$  m where  $x > 19.2$  km (Fig. IV-9(b)). The position of this strong mixing layer matches the position of interfacial layers between upper and lower layers in Fig. IV-8(a<sub>2</sub>). At the time ( $T_4$ ), the maximum dissipation rates are observed at the bottom layer between  $x = 17.8$  km and  $x = 18.1$  km (Fig. IV-9(c)), similar to the uni-directional mode in the ebb (Fig. IV-9(a)).

$Ri$  at time ( $T_1$ ) in Fig. IV-9(d) shows that during ebb even though the flow is strongly stratified at the head of salt tip ( $Ri \geq 1.0$ ), the flow exists in uni-directional mode. The maximum dissipation rates are observed near the bottom, but strong stratification still persists (Fig. IV-9(a) and (d)). Near slack before flood (at time ( $T_2$ )), strong mixing layer appears with  $Ri < 0.25$  (Fig. IV-9(e)) and the dissipation rate shows the maximum in this interfacial mixing layer (Fig. V-5(a<sub>2</sub>) and V-6(b)). Fig. IV-9(b) & (e) shows that with the high dissipation rates in that layer, turbulence due to the strong shear seems to mix water column vertically. This mixing layer disappears in the uni-directional mode for flood. At the time ( $T_3$ ), the Richardson numbers are larger than 1.0 and the flow is strongly stratified in most place of the salt head including the locations where maximum dissipation rates are observed (Fig. IV-9(c) & (f)).

In contrast to the salt tip, the flow in the upstream shows very small or zero of the Richardson number and the dissipation rates is smaller than  $10^{-8.5}$  W/kg at all times (Fig. IV-9(a)-(c)) and the flow has uniform density distribution as in Fig. IV-8. So this region is well mixed and the strong resuspension is also observed over the whole period. The bottom shear velocity in the upstream is larger than 0.005 m/s ( $|u| > 10$  cm/s) (Fig. IV-9(a)-(d)), which is much larger than a critical number of the bed-shear stress initiates suspension of the sediments which Van Rijn (1993) provided.

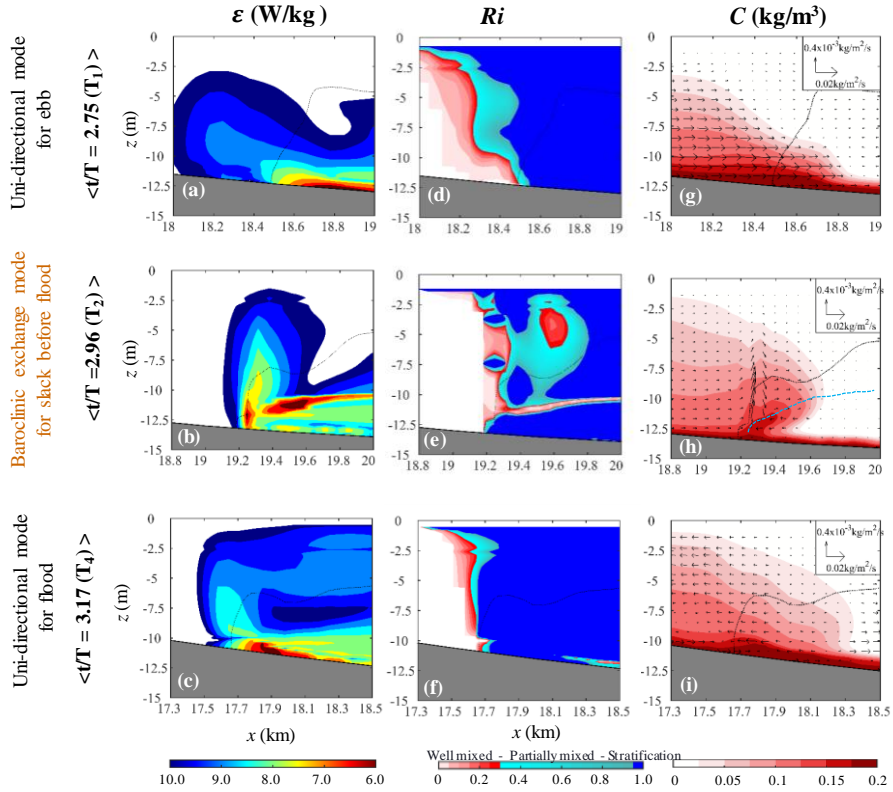


**Fig. IV-9** Kinetic dissipation rate ( $\epsilon$ ), Richardson number (Ri) number and suspended concentration (C) in a 1.0 km longitudinal cross-section of the salt tip for two flow modes in two tidal phase for case 3 (3D). (a)-(c): dissipation rate ( $\log_{10}(\epsilon)$ ), (d)-(f): the Richardson number (Ri), (g)-(h): the suspended concentration (C) with the sediment flux vector. The results in uni-directional mode for ebb and flood is represented by the results at time ( $T_1$ ) and ( $T_4$ ), respectively. The results in the exchange flow mode is represented by the results at time ( $T_2$ ). The small black dotted line is the contour of 0.005 psu salinity, separating domain into two zones, the left side is freshwater zone, the right size is saltwater zone. The white color in the freshwater show for the case density is homogenous in the vertical direction. The small blue dotted line show the locations of the interfacial layer between two flow layers.



In the uni-directional mode of the ebb, the resuspended sediments are transported to seaward (Fig. IV-9(g)). From the salt tip to downstream ( $x > 18.5$  km), higher concentrations of sediment are observed only near the bottom implying that the sediments are trapped near the bottom by the stratification (Fig. IV-9(g)). According to Geyer (1993), strong stratification at the salt head may work as a trap to suppress the suspended sediment, since the stratification can limit resuspension of the near bottom sediments into upper layer.

At the time ( $T_2$ ) near the end of the ebb or near slack just before flood, the flow is in the exchange flow mode (Fig. IV-9(h)) and the sediments resuspended from the bottom near the salt tip ( $x = 19.23$  km) vertically migrate a lot into the whole water column, similar to the Geyer (1993) mentioned. Generally, the resuspension and vertical transport of sediments are related to bottom shear stress and vertical advection by the overturn flow, but at this moment, the vertical advection seems to be more dominant than the bottom shear stress. Fig. IV-9(h) shows the vectors of the sediment fluxes between  $x = 19.25$  km and  $x = 19.35$  km, where the strong overturn flow exists (Fig. IV-9(a<sub>2</sub>) & (b<sub>2</sub>)) and at this location, the strong mixing layer is observed in Fig. IV-9(b), therefore, the lightly higher concentrations of sediment are observed near this layer along with overturn (Fig. IV-9(h)).

The sediment transport near the head of salt tip at the time ( $T_4$ ) are not similar to at the time ( $T_2$ ) (Fig. IV-9(h)-(i)) since there is no overturn, which drives strong resuspension at time ( $T_2$ ). At time ( $T_4$ ), the suspended sediments are mainly transported to landward, except sediments in the thin layer near the bottom which are transported to seaward after resuspension (Fig. IV-9(i)). At that

time, the higher concentrations of sediment and the convergence of their fluxes are observed in a distance from  $x = 17.7$  km to  $x = 18.1$  km. In the temporal perspectives, over a tidal cycle, higher sediment concentrations were observed near the salt tip at time ( $T_2$ ) (Fig. IV-9(h)) and during at the slack before flood ( $3.19 < t/T \leq 3.44$ ), respectively (Fig. IV-7(a)). During those periods, flows are in the exchange modes (Fig. IV-7(a)) and so the strong overturn of flows were observed (Fig. IV-8(a<sub>2</sub>) and (b<sub>2</sub>)). Conventionally, tidal pumping, gravitational circulation and lateral circulation have been known as main mixing mechanisms. Along with such macro and conventional mixing processes, the overturn related with baroclinity must play an important role in increasing the suspension rate of sediments at the salt tip.

#### 4.5.3.2 *The effects of the overturns to the sedimentary transport process*

To find the relative contribution of the tidal pumping and the estuarine circulation to determining the sediment concentration during the slack before flood when the exchange flow mode occurs, the variations of the sediment concentration and the lateral and streamwise sediment fluxes are investigated at salt head over a tidal cycle. The concentration of the sediment is represented by the values computed by the concentrations which are determined by depth-integrating at the *thalweg* and streamwisely averaging over 250 m of the distance from the salt tip to downstream (Fig. IV-10(a)). We apply equation (2.5) – (2.6) which were shown in the section (2.1.3) to compute the magnitude of sediment flux in longitudinal (Fig. IV-10(b)) and lateral directions (Fig. IV-10(c)),

respectively. Each directional flux is separated into two components that are non-tidal advection driving flux (advection) and the tidal pumping flux (pumping).

In the temporal perspectives, the sediment concentration reaches the highest value at  $t/T = 2.94$  of time (F), near the slack just before flood over a tidal cycle as in Fig. IV-10(a). At that moment, the magnitude of the sediment pumping flux at time (F) is much larger than the advected flux of sediments (Fig. IV-10(b)) and so the increase of the sediment concentration seems to be more largely induced by the intense of the tidal pumping than the estuarine circulation.

Besides streamwise process, the lateral process partly contributes to the increases of sediment concentration at time (F). Fig. IV-10(c) shows that the size of the lateral sediment pumping flux is  $0.38 \times 10^{-2} \text{ kg/m/s}$  and equals to 10% of the longitudinal sediment pumping flux at the same time (Fig. IV-10(b)). At time (F), the lateral process partly induces for the increase of the sediment at the *thalweg* showing by the negative lateral sediment pumping flux (direction to the center). However, even though including the lateral flux, total sediment flux ( $SF_x + SF_y$ ) at the time (F) does not explain the reason for the significant increase of the sediment concentration at that time. At time (F), the total sediment flux is much smaller than in another period such as in flood ( $3.0 < t/T \leq 3.4$ ) (Fig. IV-10(d)). During flood, the maximum of the total sediment flux is observed at  $t/T = 3.12$  (Fig. IV-10(d)), but the sediment concentration at that time just equals about 70% the sediment concentration at time (F) (Fig. IV-10(a)). The high sediment concentration is observed near the slack before ebb ( $3.0 < t/T \leq 3.4$ ), but the magnitude of the total sediment flux at any time during this period is smaller than that at  $t/T = 3.12$  (Fig. IV-10(d)). Therefore, beside the tidally

pumping or the estuarine circulation, the sediment transport process at the salt tip near the slack before ebb is partly induced by another process such as overturns of flow.

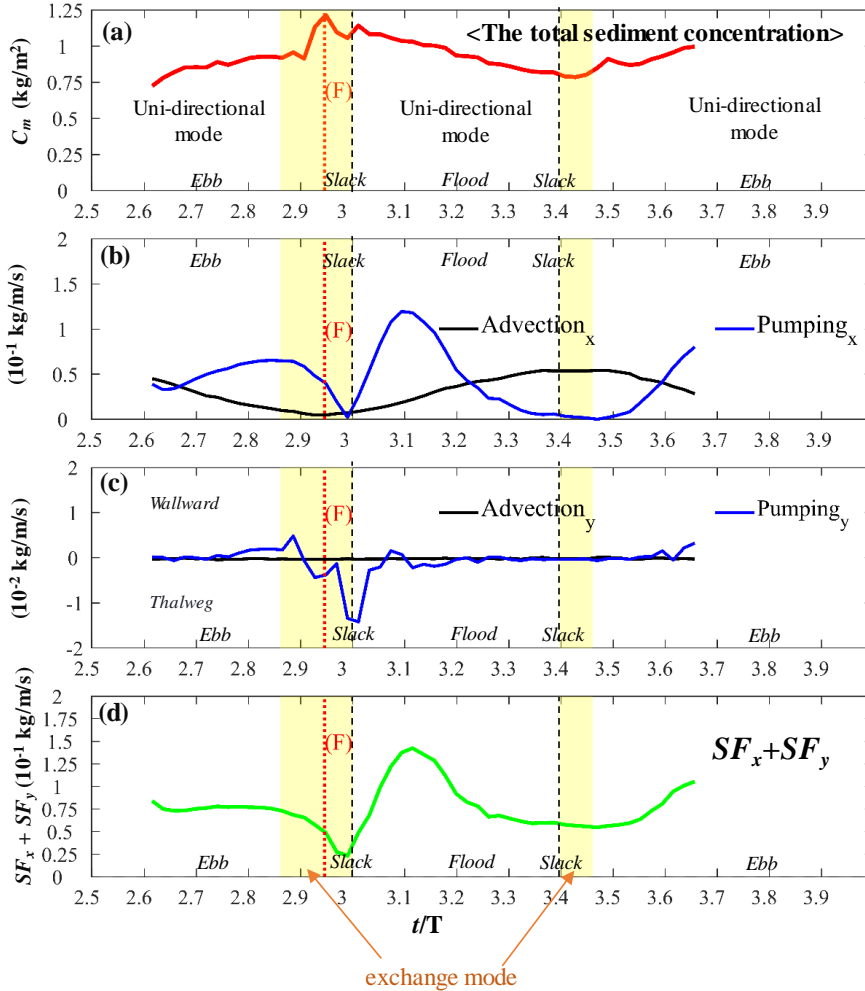


**Fig. IV-10** The time series of the total sediment concentration, the integral sediment advection flux and the sediment pumping flux through the water column in the streamwise direction and lateral direction and the total sediment flux over a the tidal cycle for case 3. (a) The averaged of the depth integral sediment concentration ( $C_m$ ) in the short distance from the salt tip to downstream (about 250 m distance around the head). (b) The integral sediment advection flux (Advection<sub>x</sub>) and the integral sediment pumping flux (Pumping<sub>x</sub>) through the water column in the longitudinal direction. (c) The width averaged of the integral the sediment advection fluxes (Advection<sub>y</sub>) and sediment pumping flux (Pumping<sub>y</sub>) through the water column in lateral direction. Positive value show sediment is transport to wallward, negative value show the sediment is

transport to *thalweg*. (d) The total sediment flux through the water column in both two directions lateral and streamwise directions ( $SF_x + SF_y$ ). Time (F) is the time the sediment concentration in (a) is greatest. Dotted red line show the time the concentration is greatest ( $t/T = 2.94$ ). Yellow aground show the periods of exchange flow mode found from Fig. V-4(a).

Besides streamwise process, the lateral process partly contributes to the increases of sediment concentration at time (F). Fig. IV-10(c) shows that the size of the lateral sediment pumping flux is  $0.38 \times 10^{-2}$  kg/m/s and equals to 10% of the longitudinal sediment pumping flux at the same time (Fig. IV-10(b)). At time (F), the lateral process partly induces for the increase of the sediment at the *thalweg* showing by the negative lateral sediment pumping flux (direction to the center). However, even though including the lateral flux, total sediment flux ( $SF_x + SF_y$ ) at the time (F) does not explain the reason for the significant increase of the sediment concentration at that time. During time (F), the total sediment flux is much smaller than in another period such as in flood ( $3.0 < t/T \leq 3.4$ ) (Fig. IV-10(d)). During flood, the maximum of the total sediment flux is observed at  $t/T = 3.12$  (Fig. IV-10(d)), but the sediment concentration at that time just equals about 70% the sediment concentration at time (F) (Fig. IV-10(a)). Further, the high sediment concentration is observed near the slack before ebb ( $3.0 < t/T \leq 3.4$ ), but the magnitude of the total sediment flux at any time during this period is smaller than that at  $t/T = 3.12$  (Fig. IV-10(d)). Therefore, beside the estuarine circulation and the tidally pumping, the sediment transport processes at the salt tip near the slack before ebb is partly induced by another process such as overturns of flow.

To clarify the difference between the roles of the tidal pumping, gravitational circulation and overturns in driving the sediment transport at the

salt tip, the linear correlations between sediment concentration at the salt tip and the total momentum flux, the vertical turbulent diffusive flux ( $c'w'$ ) is investigated in two periods of near the slack before flood( $2.87 < t/T \leq 3.0$ ) and the flood ( $3.0 < t/T \leq 3.4$ ) (Fig. IV-11). According to Fugate and Friedrichs (2002), the vertical turbulent diffusive flux seems to be relative directly with the downward velocity of suspended sediment and so the vertical turbulent diffusive flux can be used here to represent for the size of vertical mixing in the water.

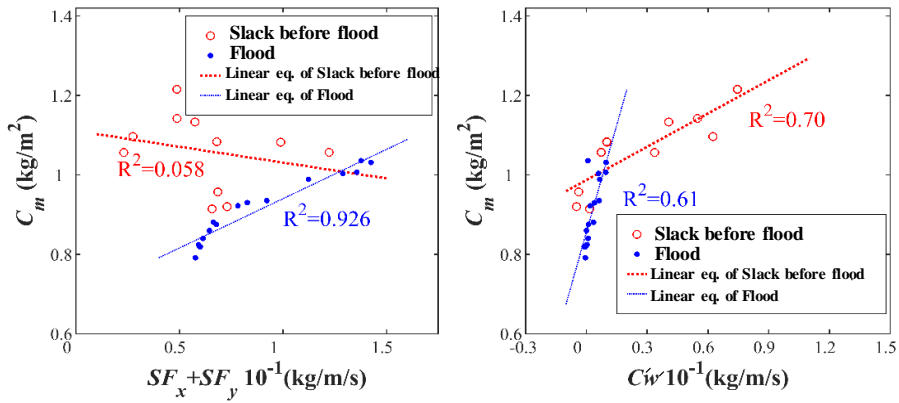


**Fig. IV-11** The linear correlation between the sediment concentration and total sediment flux, the vertical turbulent diffusive flux for case 3 (3D model) for the period of slack before flood and period of flood. (a) The linear correlation between the depth integral sediment concentration ( $C_m$ ) and total sediment flux ( $SF_x + SF_y$ ), (b) The correlation between the sediment concentration ( $C_m$ ) and the vertical turbulent diffusive flux ( $C'w'$ ).

The sediment concentration at the salt head in the flood has strong relationship with the total sediment flux ( $R^2 = 0.926$ ) as expected (Fig. IV-11(a)). The sediment concentrations in flood increase along with increases in the total sediment flux ( $SF_x + SF_y$ ) and therefore, the tidal pumping and estuarine circulation may play an important role in driving sedimentary processes in the flood. On the other hand, there is no linear correlation between the sediment

concentration ( $C_m$ ) and the total momentum flux ( $SF_x + SF_y$ ) in the ebb just before slack and the correlation  $R^2$  is only 0.058. Therefore, the significant increases of the sediment concentration in that period seems to less related with the tidal pumping or estuarine circulation. Instead, the correlation between sediment concentrations and the vertical turbulent diffusive flux is 0.7 of  $R^2$  which is high enough value to say that they are correlated (Fig. IV-11(b)). Previously, we observed strong overturns during this period and this overturns of flow significantly enhance the vertical migration and mixing of sediment. During flood, flux is mainly driven by tidal pumping, and so has less vertical fluxes (Fig. IV-10(b)) which has less correlated with concentration. It means that during flood turbulence does not generate vertical transport of sediment. This result also confirms by the observations of the Richardson number in Fig. IV-11(f) showing that vertical mixing is limited during flood while turbulent mixing occurs near slack before flood (Fig. IV-11(e)).

#### **4.6 Discussion and summary**

Therefore, similar to the observation of the Sanford et al., (2001) for the upstream of the Chesapeake Bay region, the tidal asymmetry plays an important role in the sediment resuspension. Our work found that the size of the tidal pumping is far larger than the size of the advection from the full ebb to the full flood ( $2.65 < t/T \leq 3.2$ ) (Fig. IV-10(b)). Besides, similar to the Sanford et al., (2001), we find that the overturns may occur at the salt tip on the slope of the upstream of the Chesapeake Bay in the slack before flood ( $2.87 < t/T \leq 3.0$ ) and the slack before ebb ( $3.4 < t/T \leq 3.46$ ). In a sketch of in Sanford et al., (2001)'s work, the vertical resuspension of the sediment could not be induced by the

overturn of the flow and this process is even suppressed by the strong stratification in the slacks. However, the results in the stretch of the Sanford et al., (2001) seem to be contract to the results in the observations from Sanford et al., (2001) and other researches (e.g., North & House, 2001; North et al., 2004) for several time moments. The observations in several surveys show that the higher concentration at the salt tip may be observed in the slacks (Fig. IV-12) and the presence of the high concentration in the slacks is similar to our results. We found that the sediment may be highly resuspended in the slack before flood (Fig. IV-9(h)) and this process is driven by the overturns (Fig. IV-8(a<sub>2</sub>)-(b<sub>2</sub>)) and the form of overturn observed in the mild slope is similar to the form of the overturn shown by the sediment flux vectors in Geyer (1993) (Fig. I-8).

Besides, the thesis found that the overturns observed in the slack before flood may induce the vertical mixing at the head of the salt tip and well mixing at the interface of the flow (Fig. IV-9(e)). In contract to North & House, (2001), the resuspension processes of the sediment during the slacks are not directly driven by the gravitational circulation, but they are driven by the turbulent mixing which is generated from the overturning flow. The results in Fig. IV-11(a) show that the sediment concentration at the salt tip in the slack before flood has the strong correlation to the vertical turbulent diffusive flux ( $R^2 = 0.7$ ) but has the less correlation to the total sediment flux ( $R^2 = 0.058$ ).

The existence of the overturn at the salt tip is directly relative to the existence of the geometry feature that is the bottom slope. Without the existence of the bottom slope, the overturning flow as well as the significant vertical resuspension of the sediment as the overturning are not observed (Fig. IV-2(b)-



(c) and Fig. IV-3(a)). Besides, in order to the overturn exists at the salt tip on the mild slope, the river flow may play an important role. Fig. IV-11(a) show that the overturn just develops on the slope when the flow is in the exchange mode and the exchange flow mode is composed by the downstream flow of the freshwater and the upstream flow of the seawater (Fig. IV-6(b)) and Fig. IV-8(a<sub>2</sub>)-(b<sub>2</sub>)). In the uni-directional mode, the seaward river flow doesn't exist near the surface and during that time, the overturn is not observed (Fig. IV-8(a<sub>1</sub>)-(b<sub>1</sub>) and Fig. IV-8(a<sub>4</sub>)-(b<sub>4</sub>)).

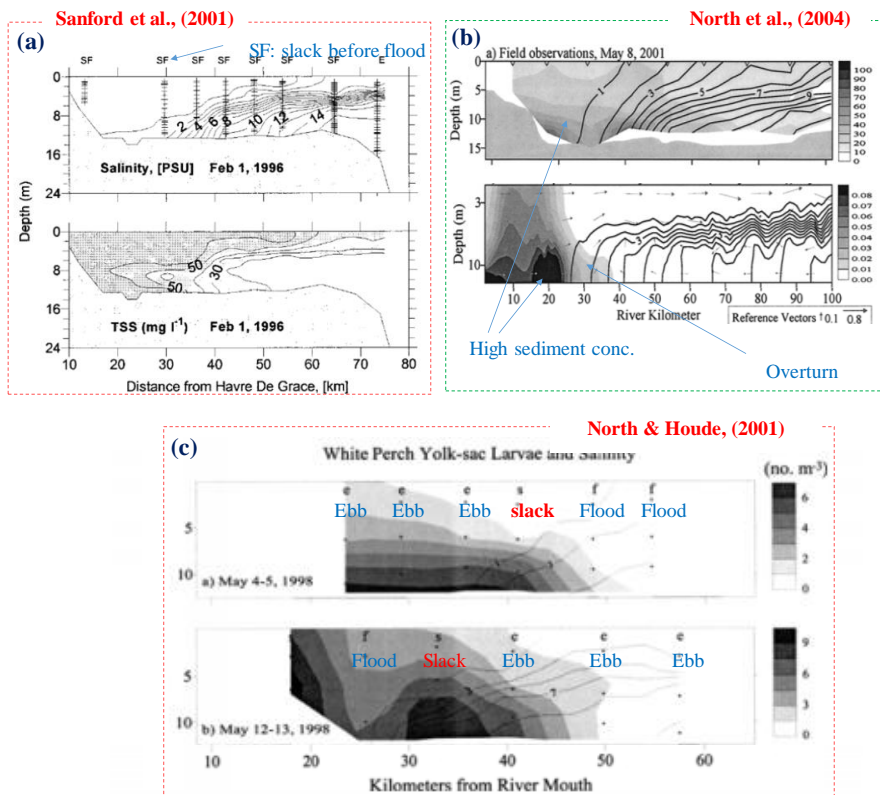


**Fig. IV-12** The observation and simulation results of the sediment concentration and salinity around the salt tip the upstream of the Chesapeake Bay estuary in North et al., (2004), North & House, (2001), Sanford et al., (2001). (a) Salinity and TSS on Feb. 01 1996 observed by Sanford et al., (2001). (b) The observation results (upper figure) on May 08, 2001 which used to be compared to the computational region (lower figure) on day 352.38 on North et al., (2004). (c) The observation results in May 4-5 and 12-13 in North & House, (2001).

The present work observes that the serious backflow in the salt tip after shoaling during the ebbs after or before slack, respectively. During that time, the freshwater and the seawater flow to the opposite directions (Fig. IV-5(a<sub>3</sub>)-(b<sub>3</sub>) and Fig. IV-8(a<sub>2</sub>)-(b<sub>2</sub>)) and the propagation of the density front seems to meet the upstream obstruction caused by the freshwater flow. That process is similar to that the frontal face of the run-up bore is hindered by the backflow on slope bottom of the continental shelf regions (Helfrich, 1992; Wallace and Wilkinson, 1988) or on the slope bottom of the coastal regions (Masunaga et al., 2015).

Similar to Masunaga et al., (2015), that the overturn in the salt tip appear with the bore. The thickness of the density front at the internal bore on the mild slope is about 5.0 m (2D model) and 4.0 m (3D model) (Fig. IV-6(e) and Fig. IV-8(c<sub>2</sub>)). The salt head becomes thicker due to the development of the density current in the exchange mode as the internal tidal bore (Fig. IV-6(d)-(e)). With this form, the internal bore with the overturn at the salt tip seem to be a form of the density current with the hydraulic jump at the head as the sketch of Bain (1995) (Fig. I-5), and is similar to the internal bore with an overturn on the coastal region observed in Masunaga et al.,(2015).

Therefore, according to the computing results, we illustrate the tidal variation of the salt tip and suspended sediment under effects of the mild slope over the tidal cycle in Fig. IV-13.

(a) During full ebb, the salt front moves to the downstream, which is the same direction to the freshwater flows at the upper layer. Sediments seem to be strongly resuspended in the freshwater layer, while the resuspension is limited by stratification in the saltwater layer.

- (b) During slack before flood, the density front of the salty water moves landward and the fresh water in the upper layer and upstream flows to the seaward accumulating of the density and velocity at the salt tip. These accumulations lead to thicken the salt tip and overturn the flow. The overturned flow induces the strong mixing and the significant resuspension of the sediment at the salt tip.
- (c) During full flood, the density front in the lower layer and freshwater in the upper layer move together to the landward and the sediments are significantly resuspended in the fresh water layer of the unstratified upstream and is vertical limited in the salt water layer by stratification.
- (d) During slack after flood, the overturn flow and the bore appear at the salt head with the smaller size and scale, compared to the previous overturn. The dynamics for the bore and overturn flow are similar to the first time (b). The sediment slightly resuspended at the salt tip by the overturn flow.

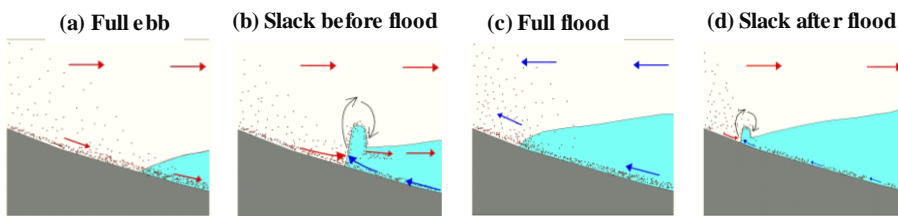


**Fig. IV-13** Schematic image of the changes of the salt head regime over a tidal cycle on the mild slope. (a) At the full ebb (the uni-directional mode for ebb), (b) At the slack before flood (in the exchange mode), (c) At the full flood (the uni-directional mode for flood) and (d) At the slack after flood (in the exchange mode).

## **CHAPTER FIVE**

### **V. THE EXISTENCE OF THE OVERTURN IN THE GRADUAL CONTRACTION AND THE SEDIMENTARY TRANSPORT PROCESSES**

#### **5.1 Introduction**

Armi (1986) found that the strong mixing from internal hydraulic jump may exists at the interface of the two-layers flow when the flow overs the constriction or the sill. However, since the overturn may develop on the mild slope bottom, we expect that the overturn may development in the contraction the contraction of the width and the bottom slope affects to the one-layer flow in the similar way (Chaudhry, 2008). In specify, we investigate for the two-layer flow over the gradual contraction. The gradual contractions may be found at the downstream of the constriction in the Hudson River estuary (Geyer and Ralston, 2015) but the effects of the width contractions to the existence of the baroclinicity as well as sedimentary transport processes have been not discussed further.

To clarify that the mild slope can be replaced by the gradual contraction in inducing the development of the internal bore as a hydraulic jump in translation or not, we try to investigate propagating process of the salt density flow in the salt tip in the gradual contraction region. The variation of the flow and salinity structure are investigated and compared the results obtained to the results in chapter IV. Besides, we investigate the sedimentary processes around

the salt tip to clarify the relative the sediment process with the contraction of the width.

## 5.2 Model set-up and data analysis

The study case in in experiment 2 uses the upstream contraction mesh shown in Fig. V-1(a)-(b). Fig. VI-1(a) shows that the width of the upstream contraction mesh varies from 155 m to 250 m between  $x = 10$  km and  $x = 20$  km. The horizontal grid size in the section between  $x = 15$  km and  $x = 22$  km is approximatly 20 m and is much smaller than those in the other regions ( $x < 15$  km or  $x > 22$  km). The vertical grid space of the mesh ranges between 0.2 m and 0.5 m. The domain uses a total of 40 layers for vertical space. The estuarine domains for the contraction case are obsolutely illustrated in 3D in Fig. III-1(d).

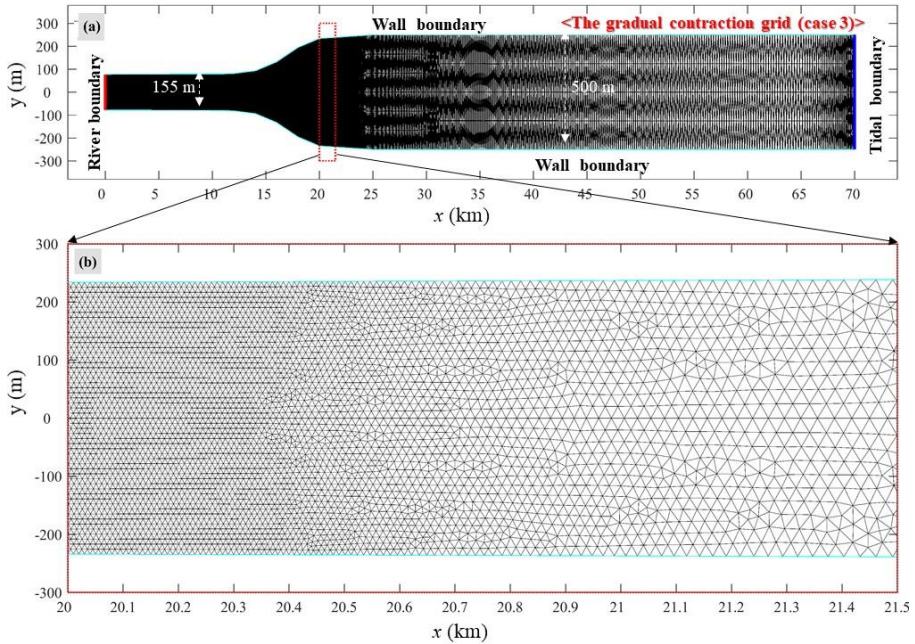


**Fig. V-1** The upstream contraction mesh used for case 4

The average amplitude of the tide ( $\eta_0$ ) and the constant freshwater runoff for case 4 are set at 0.5 m and 0.1 m/s, respectively, and the bottom elevation ( $z_b$ ) is at -14.5 m for the whole domain. With the above setup, case 4 in this chapter and case 3 (bottom slope, 3D) in chapter IV have the same magnitude of the river discharge and tidal discharge at the boundary conditions. Other information about setups for case 4 is introduced in section 3.1.

Similar to bottom slope case, the contraction case is simulated for five tidal cycles. Since the salt head is observed in a distance from  $x=10$  km to  $x=20$  km from two tidal cycles, the results from tidal cycles of 2 to 4.5 are used for the analysis. The outputs from the SUNTANS used in this chapter include: salinity concentration, sediment concentration, the turbulent velocity scale, the turbulent length scale. Besides, three components of the velocities are used.

### **5.3 The existence of the overturn and internal bore in the contraction region**

Similar to the previous chapter, before clarifying the existences and the effects of the overturn, we determine the locations of the salt tip from the streamwise salinity density gradient. At the locations of the salt tip, we get the profile of the  $u$ -velocities by using the Lagrangian way. From the profile of the  $u$ -currents near the free surface and near the bottom boundary obtained, the tidal phases along with the flow modes at the salt tip 2.5 tidal cycle ( $2.5 < t/T \leq 4.0$ ) are respectively determined.

Fig. V-2(a) shows that the flow at the salt tip for the contraction case (case 4) includes two tidal phases that are flood and ebb, and the exchange flow mode

exists during flood phase. From slack after ebb to slack after flood ( $2.76 < t/T \leq 3.28$ ), the flow appears in exchange flow mode since the  $u$ -current near bottom is negative while the  $u$ -current near the surface is positive (Fig. V-2(a)). When the near-bottom  $u$ -current becomes positive from  $t/T = 3.28$ , the flow changes to the uni-directional flow mode for ebb. The uni-directional flow exists for 0.47 tidal cycle, and ends at  $t/T = 3.75$  when the surface  $u$ -current changes the sign to negative (Fig. V-2(a)).

Similar to the bottom slope case (Fig. IV-8, Fig. IV-9(g), (h), (i)), the flow structure and the sedimentary processes between two flow modes in the contraction (case 4) are absolutely different. Those differences are found from the comparisons between the horizontal vectors of the currents along with the sediment concentration near the bottom at  $t/T = 2.99$  for exchange flow mode (time ( $C_1$ )) and  $t/T = 3.6$  for uni-directional mode (time ( $C_2$ )) (Fig. V-2(b), (c)). At time ( $C_1$ ), the directions of saltwater flows are opposite to the directions of the freshwater flows (Fig. V-2(b)). In contrast, the vectors of the horizontal currents at time ( $C_2$ ) shows that the both flows of the saltwater and the freshwater are in the same direction for ebb (Fig. V-2(c)). Besides, the salt flows near the bottom are laterally to middle in flood but are to the sidewall in ebb (Fig. V-2(b)-(c)). However, for both two flow modes, the lateral mixing, which is normally driven by the lateral flows developing in upstream or the downstream of the rapid contraction/expansion sections (Hager, 1992; Chant and Wilson, 1997), don't exist in both the two side-walls (Fig. V-2(b)-(c)). Instead, in the gradual contraction case (case 4), the mixing in vertical direction seems to be more significant than that in the lateral direction.

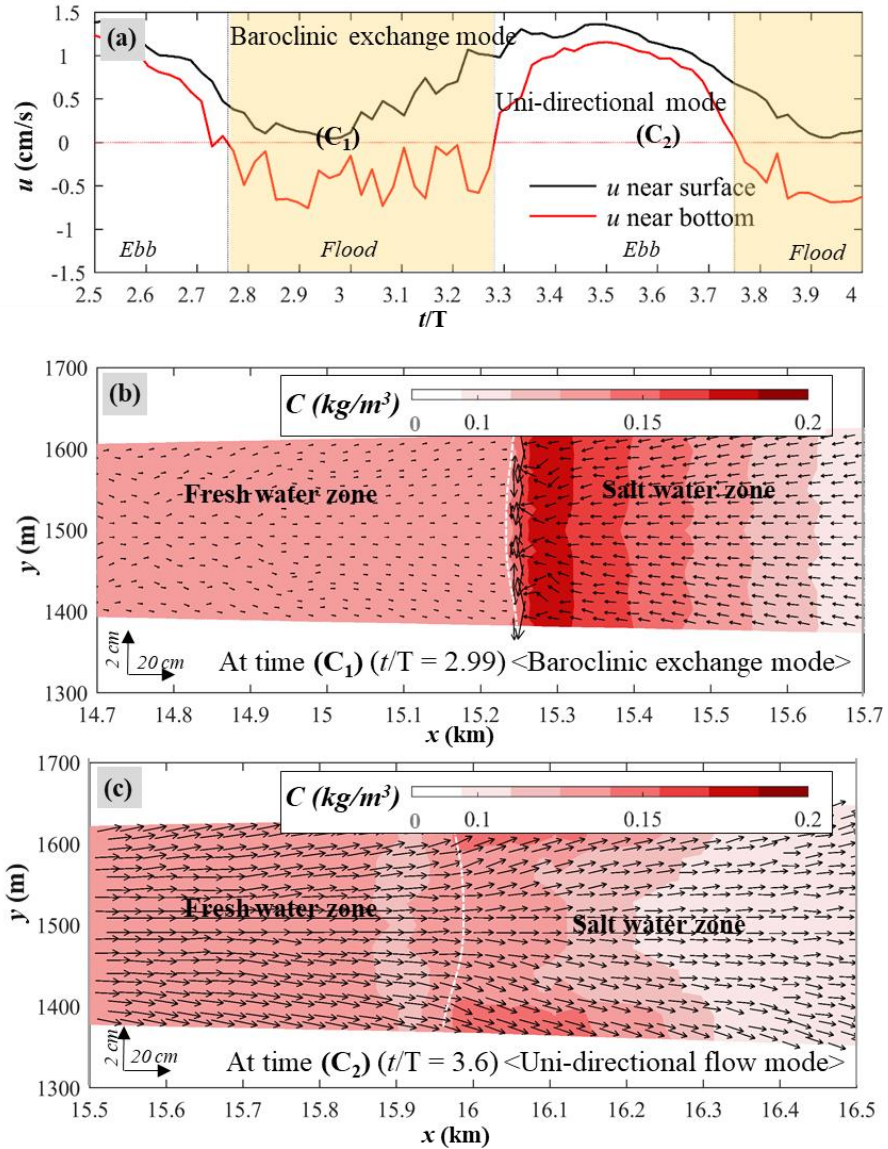


**Fig. V-2** The profile of the streamwise-velocity near the free surface and near the bottom boundary at the salt tip, the horizontal distribution of the sediment concentration and the velocity vectors ( $u \times v$ ) from 2.0 m distance from bottom at time  $(C_1)$  and  $(C_2)$  for case 4 (the contraction case). (a) The profile of the streamwise velocity near the free surface and near the bottom boundary at the salt tip used to determine the exchange flow mode and uni-directional mode. (b), (c) The top view of the sediment concentration and horizontal current in 1.0 km distance around the salt tip at time  $(C_1)$  and  $(C_2)$ . In (a), the  $u < 0$ : flood and  $u > 0$ : ebb. In (b), (c), the small white dotted line is the contour of 0.005 psu salinity as the location of the salt tip, separating the domain into two zones, the left side of the salt tip is the freshwater zone, the other side is the saltwater zone. Yellow background in (a) show the periods of the exchange mode.



For constant of the width (case 1), the suspended sediment in the saltwater layer near the end of the salt tip normally is trapped by the strong stratification (Fig. IV-3(a)), but Fig. V-2(b) show that much higher sediment concentration is observed around the salt tip ( $15.28 \text{ km} < x \leq 15.32 \text{ km}$ ) at time ( $C_1$ ) when the flow is in the exchange mode (Fig. V-2(a)). The results in chapter IV show that the sediment near the bottom may be strongly resuspended by the vertical mixing driven by the overturn (Fig. IV-9(h)) and therefore, similar to in the mild bottom slope region, the significant vertical mixing by the overturn seems to exist and promote the resuspension process of the sediment in the gradual contraction region.

In order to clarify whether or not the existence of the overturn in the mild contraction and in order to explain why the sediment concentration around the salt tip at time ( $C_1$ ) is higher than that at time ( $C_2$ ), the flow and salinity structures of the salt tip at two time moments are respectively investigated and compared. In which, the salt tip at time ( $C_1$ ) is located at  $x = 15.2 \text{ km}$ , and from that location to the downstream, the water column has the two-layer flows (Fig. V-3(a)). Both upper flow and lower flow at the salt head have a slight increase in the magnitude of the streamwise currents ( $|u| > 10 \text{ cm/s}$ ). Besides, the maximum of the  $w$ -current at this time is significant ( $|w| > 0.5 \text{ cm/s}$ ) (Fig. V-3(b)). Fig. V-3(a) and (b) illustrate that there is a vertical circulation existing near the end of the salt tip, and this circulation evenly appears at the same location with the internal bore structure (Fig. V-3(c)). The distribution of the salinity around the salt tip show for the existence of the bore structure (Fig. V-3(c)), similar to the internal bore observed in Fig. IV-6 for the bottom slope case.

Besides, the structure of the salt flow in the uni-directional mode in the contraction case is mostly similar to that in the bottom slope case for the same flow mode (Fig. IV-5(a<sub>1</sub>), (b<sub>1</sub>) and Fig. IV-8(a<sub>1</sub>), (b<sub>1</sub>)). In the uni-directional mode for ebb (time (C<sub>2</sub>)), the fresh water and salt water flows quickly to mainly upstream (Fig. V-3(d)) and the vertical flow is very slow ( $|w| < 0.04$  cm/s) (Fig. V-3(e)). Moreover, the thickness of the salt layer in this period gradually decreases to zero in from the downstream to the end of the salt tip (Fig. V-3(e)).

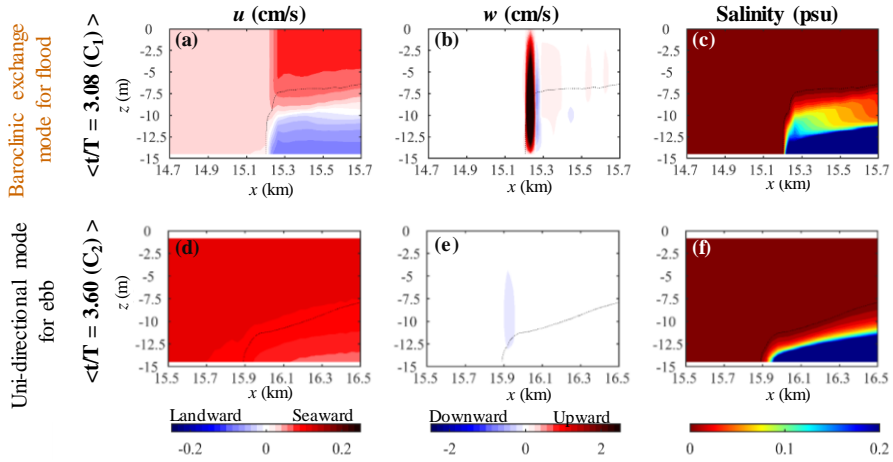


**Fig. V-3** Distribution of the two velocity components and distribution of the salinity concentration. Streamwise velocity ( $u$ ), vertical velocity ( $w$ ), salinity concentration ( $s$ ) in the 1.0 km longitudinal cross-section of the salt tip for the case in experiment 2(a) (Case 3) (the contraction case) at time ( $C_1$ ) and time ( $C_2$ ). The small black dotted line is the contour of 0.005 psu salinity, separating the domain into two zones, the left side of the figure is the freshwater zone, the other side is the saltwater zone. Time ( $C_1$ ) and ( $C_2$ ) are depicted in Fig. V-2(a)

Fig. V-3 shows that the flow and salinity structures in the contraction in the uni-directional mode and the exchange flow mode are respectively similar to those in the bottom slope region or on the coastal region (Masunage et al., 2015). For the exchange mode, the internal bore along with the overturn occurs in the

gradual contraction (Fig. V-4), similar to the bottom slope case (Fig. IV-6(d) and (e)). The overturn develops from traveling of the salt layer in the downstream flow environment in the contraction or seems to show for a form of the hydraulic jump at the head of the density current (Fig. V-4), similar to the density current with supercritical head mentioned from previous researches (e.g., Benjamin, 1968; Xu, 1991; Baines, 1995). In the contraction region, the overturn occurs when the two-layer flow exists and interacts with the freshwater flow. Around the salt tip, the size of the magnitudes of longitudinal and vertical velocities at the internal bore for both two cases are about  $|u| > 10$  cm/s and  $|w| > 0.5$  cm/s, similar to the size of the velocity observed in the internal bore on the mild slope (Fig. IV-8(a<sub>2</sub>) and (b<sub>2</sub>)). Comparing to the vertical velocity in the exchange flow mode (Fig. V-3(b)), the vertical flow is in the unidirectional mode in both cases are too small ( $|w| < 0.04$  cm/s) (Fig. V-3(e)).

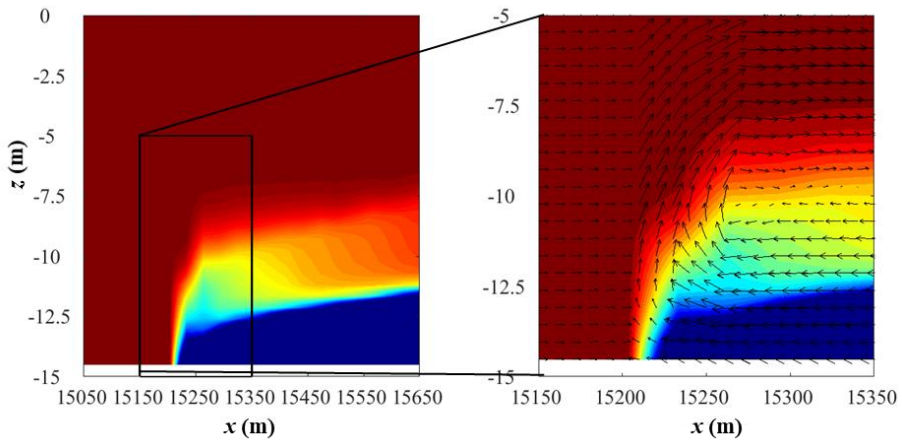


**Fig. V-4** The structure of the salt tip with an overturn for the contraction case (case 3) at time ( $C_1$ ). Time ( $C_1$ ) is depicted in Fig. VI-2(a)

Further, although both the geometry of bottom and the geometry of the plan view (contraction) can lead to the development of the overturn, their influences

on flow are not the same. For the same boundary conditions ( $\eta_0 = 0.5$  m and  $u_0 = 0.1$  m/s), the time for the exchange flow in the gradual bottom slope is much longer. For instance, the exchange flow in case 3 (the bottom slope case, 3D) just occurs in the several hours during slack before flood ( $0.15$   $t/T$ ) and slack before flood ( $0.06$   $t/T$ ) (Fig. IV-7(a)) but the exchange flow in the gradual contraction may exist in whole flood period ( $0.52$   $t/T$ ) (Fig. V-2(a)).

#### 5.4 The suspended sedimentary transport processes

In order to clarify the differences in the sedimentary processes between the two flow modes in case 4 (the contraction case), the distribution of the sediment concentration and the distribution of the sediment fluxes at two moments in case 4 (time ( $C_1$ ) and ( $C_2$ )) are investigated. The results of the sediment processes at two flow modes are presented in Fig. V-5. In which, the figure in the first column (Fig. V-5(a)) shows the result of the sediment for time ( $C_1$ ) (the exchange flow mode), and the figure in the second column (Fig. V-5(b)) shows the result of the sediment for time ( $C_2$ ) (the uni-directional flow mode).

At time ( $C_1$ ) when the flow is in the exchange mode, the sediments from the bed around the salt tip ( $x=15.18$  km) migrate significantly into the water column and entrance a lot at the interface of the two-layer flow (Fig. V-5(a)). At those moments when the high concentration is observed, the overturn is observed (Fig. V-4). The previous chapter found that the flows in the overturn causes the strong resuspension and play an important role in enhancing the bottom shear stress as well as the vertical advection and generating the strong mixing at the salt tip and

in the interface of the flow. Therefore, it can be concluded that the high sediment concentration in the water at time ( $C_1$ ) is driven by an overturn.

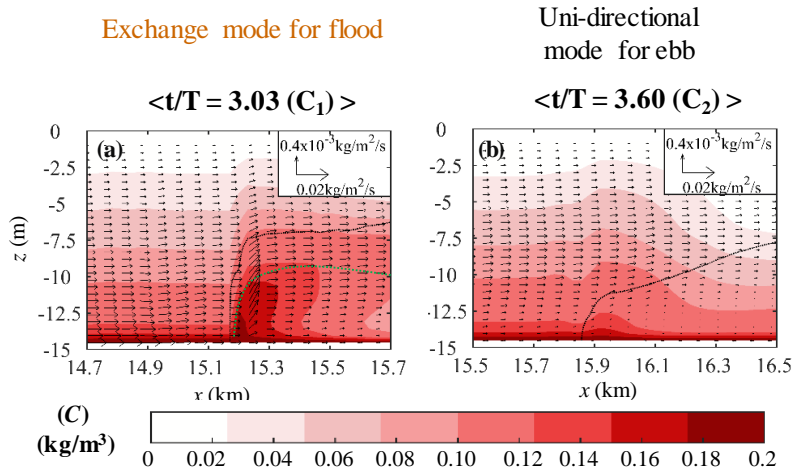


**Fig. V-5** The suspended concentration ( $C$ ) with the sediment flux vectors in a 1.0 km longitudinal cross-section of the salt tip for case 4 (Contraction case). The small black dotted line is the contour of 0.005 psu salinity, separating domain into two zones, the left side is freshwater zone, the right size is saltwater zone. The small blue dotted line show the locations of the interfacial flow layers. Time ( $C_1$ ) and time ( $C_2$ ) are depicted in Fig. V-2(a).

In contrast, the sediment at time ( $C_2$ ) is transported to the downstream and isn't been highly resuspended into the water column (Fig. V-5(b)), compared to that in time ( $C_1$ ) (Fig. V-5(a)). The results in the previous chapter (Fig. IV-9(a), (d), (g)) find that without the existence of the overturn, the sediments are significantly trapped by the stratification of the salt layer in the ebb and we observe similar process for time ( $C_2$ ). At time ( $C_2$ ), the concentration of the sediment from the salt tip to downstream is smaller than that in the fresh layer from the salt tip (Fig. V-5(b)) because the flow in the salt layer is in strong stratification in the ebb (Fig. IV-9(d)). The stratification work as a trap for the

resuspended sediment (Geyer, 1993). Therefore, in the uni-directional mode for ebb, the high concentrations of sediment are just observed only near the bottom because of trapping (Fig. V-5(b)).

Therefore, in the uni-directional mode, the sedimentary process in the contraction (case 4) or in the bottom slope regions (case 3) are mostly similar (Fig. V-5(b); Fig. IV-9(g); Fig. IV-3(b)). For the exchange mode, the vertical migration of the suspended sedimentary transport just is strong due to the overturns. However, the overturn which drives the vertical mixing of the sediment just is generated in the geometry regions such as bottom slope or the contraction (Fig. V-5(a); Fig. IV-9(h)). For the estuary with the flat bottom and constant width, the overturn is not observed (Fig. V-3(a)).

## **5.5 Discussion and summary**

The above results and comparisons shows that the gradual contraction may impact significant to the flow and density structure of the estuary. The exchange flows normally appear in the short time ( $> 0.03 t/T$ ) for the constant width estuary (Fig. IV-5(e)), but that may appear in longer time during the flood ( $0.52 t/T$ ) in the contraction region (Fig. V-2(a)). During the flood period, the salinity structure at the head of salt flow significantly varies due to the variations of the flows (Fig. V-3(c)). Therefore, the time for the existence of the exchange flow as the baroclinicity, which initiales the development of frontogenesis (density fronts) in the throat region of the constrictions in Hudson river (Geyer and Ralston, 2015), seems to be strengthened because it exist in the upstream contraction of the width in the downstream constrictions.

Although the width of the estuary investigated in case 4 is contracted gradually, we found that the gradual contraction of the width significantly affects to the presence time for the exchange flow and the mixing process at the salt tip. In the gradual contraction, the upstream traveling of the salt tip front may lead to the development of the overturn (Fig. V-4) which is supposed to be important in inducing the significant vertical mixing (Masunaga et al., 2005). Therefore, under effect of the overturn, the size of mixing in the gradual contraction in the vertical direction is larger than that in the lateral direction. The lateral mixing is normally observed the rapid contraction (Hager, 1992; Chant and Wilson, 1997).

ETMs are frequently observed in the contraction/expansion of estuary such as in the Columbia River (Jay & Musiak, 1994) and Delaware (Sommerfied & Wong, 2011), Hudson River estuary (e.g., Ralston et al., 2012; Burchard et al., 2018; Geyer and Ralston, 2015) (Fig. I-13). Normally, the investigations for the development of the ETMs in the contraction/expansion mostly focus on two processes that are the tidal asymmetry and gravitation circulation (e.g., Burchard et al., 2018; Sommerfied & Wong, 2011; Jay & Musiak, 1994). However, the results from the sediment fluxes show that the vertical mixing driving by the overturn induce the vertical immigration of the sediment around the salt tip region (Fig. V-5-(a)). For the middle of the salt wedge regions such as around the frontogenesis in Hudson river (Geyer and Ralston, 2015), the suspended sediments from the bed may not migrate a lot to water column as in the salt tip region by cause of the presence of the strong stratification. However, the increasing the strength and duration of the exchange from the gradual contraction

may affect directly to the tidal asymmetry and gravitation circulation processes which drive the sedimentary processes in the estuaries.

According to the results obtained, we illustrate the vertical mixing and sedimentary process in the contraction (for the same boundary condition with the case 3) in Fig. V-6.

(a) During ebb, the salt front travels to the downstream in the same direction movement of the flows. Sediments seem to be strongly resuspended in the freshwater layer and is trapped by stratification in the saltwater layer.

(b) From slack before flood to slack after flood (during flood), the density front of the salty water travel landward in the seaward flow of the freshwater. The salinity and flows structures at the salt tip show for the existence of the internal bore with an overturn. That overturn seems to induce the significant migration of the suspended sediment from the toe of the salt tip.

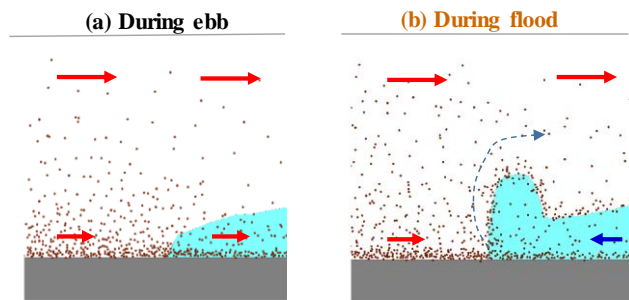


**Fig. V-6** Schematic image of the variations of the salt head regime through the tidal cycle in the contraction case. (a) During ebb (uni-directional mode), (b) During flood (exchange flow mode).



## CHAPTER SIX

### VI. THE MECHANISM OCCURRING THE OVERTURN AS THE TERMS OF THE HYDRAULIC JUMP IN THE SALT TIP UNDER THE GRAGUAL EFFECTS OF THE GEOMETRY

#### 6.1 Introduction

The previous sections show that the mixing may be generated at the salt tip when the flow is stratified as the two-layer flow. Unlike the general two-layer system, the vertical mixing as overturning may occur at the salt tip without the geometric critical point ( $dW/dx = 0$  or  $dz_b/dx = 0$ ) (Armi and Farmer, 1986) or Armi, 1986)) or the steep bottom slope (Masunaga et al., 2015; Wang et al. 2008). The significant interaction between the saltwater flow and fresh water flow under the support of the geometry features such as the mild slope or even the gradual contraction of the width may lead to development of the strongly vertical mixing. The exchange flows without upstream depth, which are generated in during slacks, are essentially an arrested the density current. However, in order to the intense turbulence and turbulent mixing is generated, the density current should has a jump at the front of its head as Simpson, (1982) or Benjamin, (1968) mentioned. The hydraulic jumps developed from the interaction between river currents and tidal currents are frequently observed on the free surface of the river mouths rather than around the end of the salt wedge on the bottom (Simpson, 1982; Nash and Moum, 2005). However, the result from the previous sections for investigating the mild slope or in the contraction region show that the hydraulic jump seems to exist at the head of salt tip.

Therefore, in order to find out the mechanism for the development of the overturn, we try to determine the presence of the jump at the salt tip. Both composite Froude number ( $G^2$ ) and Froude number method ( $Fr_f$ ) are used in our investigation. Besides, the role of the geometric features as well as the fresh flow are clarified by investigating the variation of the momentum fluxes. In this chapter, we use the simulation results from the four studied cases for discussions. Characteristics and the results over the four study cases from previous chapters are shortly presented in the table 3.

**Table 3** The statistics table of the information about four study cases for investigate the development of the hydraulic jump used in chapter VI

Name of study case	Boundary condition for $\eta_0$	Boundary condition for $u_0$	Name of the experiment	Model	Results of the flow and salinity structure	Results of sedimentary processes
Case 1	0.5 m	0.1 m/s	Non-geometry effect	3D	Overturn and internal bore are not observed	Without significant vertical immigration of the sediment
Case 2	0.5 m	0.1 m/s	Bottom slope effect, 2D model	2D	Vertical mixing driven by the overturn, and internal bore are observed	Sediment is significantly resuspended by the overturn flow
Case 3	0.5 m	0.1 m/s	Bottom slope effect, 3D model	3D		
Case 4	0.5 m	0.1 m/s	The contraction of the width	3D		

Four cases in table 3 computes for the river currents ( $u_0$ ) with 0.1 m/s and the tidal wave with 0.5 m of the average amplitude ( $\eta_0$ ). In fact, in the upstream of the Chesapeake Bay, the size of the river flows may vary from zero to 0.17 m/s (Sanford et al., 2001) and the tidal amplitude varies between 0.25 m to nearly 1.0 m (North et al., 2004). According to Ficher et al., (1979), the structure and movement of salt wedge is decided by interaction between tide flow and river flow. Studying about estuarine processes, North et al., (2004) show that river inflows affect not only for salt wedge upstream movement but also for sediment suspended processes.

Therefore, we try to compute processes in the estuary for more several level of the tide and river inflow rate. Since the overturn may exist in the exchange flow and therefore, to determine the existence of the overturn for other flow condition cases, we investigate the time for the presence of the exchange flow at the salt tip and determine existence of the overturn in during this time. In the experiment 4, there are five levels of  $\eta_0$  (0.25 m, 0.35 m, 0.5 m, 0.75 m, 1.0 m) and five levels of  $u_0$  (0.05 m/s, 0.075 m/s, 0.1 m/s, 0.135 m/s, 0.17 m/s) are respectively investigated. There are totally thirty scienarios are simulated.

Excepting the tidal amplitude and river current at the boundaries, the other parameters setup in the study cases in experiment 4 are similar that in the previous experiments (experiment 1-3) (section 3.1). The three types of the domains are used for simulations in experiment 4, that are the flat bottom-constant width domain (Non-geometry group), the bottom slope domain (Bottom slope group) and the contraction of the width domain (Bottom slope group). The

information about the tidal amplitudes and freshwater runoff in experiment 4 are listed in table 4.

**Table 4** The information about the thirty scenarios used for investigating the dependence of the presence time for the exchange flow on the tidal amplitudes and the river inflow rate (experiment 4).

Name of group	Number of the scenarios in each group	For investigating the effect of the tidal amplitude ( $\eta_o$ )	For investigating the effect of the freshwater runoff ( $u_o$ )
Non-geometry group	10	$u_o = 0.1$ m/s $\eta_o = 0.25$ m, 0.35 m, 0.5 m, 0.75 m, 1.0 m	$u_o=0.05$ m/s, 0.075 m/s, 0.1 m/s, 0.135 m/s, 0.17 m/s $\eta_o = 0.5$ m
Bottom slope group	10		
Contraction group	10		

## 6.2 The effects of the geometry on the flow around the salt tip

### 6.2.1 The time for the existence of the exchange flow in the salt tip under the geometric features.

The results in the previous sections provide that the overturn plays an important role in driving the mixing and the sedimentary processes around the salt tip. However, the overturns just seem to appear when the exchange flow exists for a long time enough. Fig. VI-1 shows that without the effects of the geometry (case 1), the exchange flow just exists in the short time in the slacks ( $t/T < 0.03$ ). For the bottom slope case (case 3, 3D model), the exchange flow

may exist for  $0.13 \ t/T$  during the slack before flood and for  $0.06 \ t/T$  during the slack before ebb (Fig. VI-1). Similarly, in the contraction region (case 4), the exchange flow may remain from the slack before flood to slack before ebb for  $0.52 \ t/T$  (Fig. VI-1). Therefore, for a tidal cycle, the total time for the existence of the exchange flow in the non-geometry region is shortest, and is just about 20% of that in the bottom slope region and no more than 4 % than in the contraction region (Fig. VI-1). Besides, the overturns are not observed in the exchange flow mode for the non-geometry case (Fig. IV-2(a)-(b)) but are observed in the other cases (Fig. IV-8(a<sub>2</sub>)-(b<sub>2</sub>), Fig. V-4). Therefore, the overturn could not develop when the exchange flow in the very short time, and the time for existence of the exchange flow is enhanced under effects of the geometry.

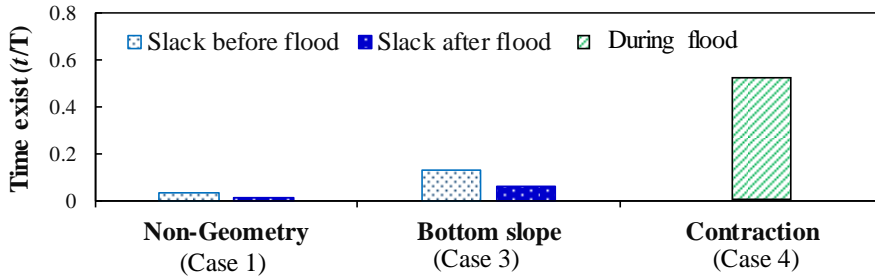


**Fig. VI-1** The summarize of the time for the existence of the exchange flow in the salt tip over a tidal cycle for three study cases (case 1, case 3 and case 4).

### 6.2.2 *The effects of the geometry on the momentum fluxes*

In order to explain why the time for exchange flow increases in the slope bottom or in the contraction region, we investigate and compare the variation of the energy of the water along the estuary over three cases: bottom slope (case 3, 3D), the contraction (case 4) to case 1 (without the existence of the bottom slope and contraction). In which, we use the tidally averaged total momentum flux for

whole a cross section ( $MF_1$ ,  $MF_2$ ) to represent for the energy existing in fresh and salt layer shown by following equations:

$$MF_1 = \overline{\int_{y=-W/2}^{W/2} (Mf_{1u} + Mf_{1p}) dy}, \text{ (Fresh layer)} \quad (6.1)$$

$$MF_2 = \overline{\int_{y=-W/2}^{W/2} (Mf_{2u} + Mf_{2p}) dy}, \text{ (Salt layer)} \quad (6.2)$$

where the bars in the formula indicates the tidally averaged of each value.

The formula used to compute each component of the momentum flux are presented in equation (2.8) and (2.9), and the results of the  $MF$  for three study cases (case 1, case 3 and case 4) are respectively illustrated in three figures of Fig. VI-2.

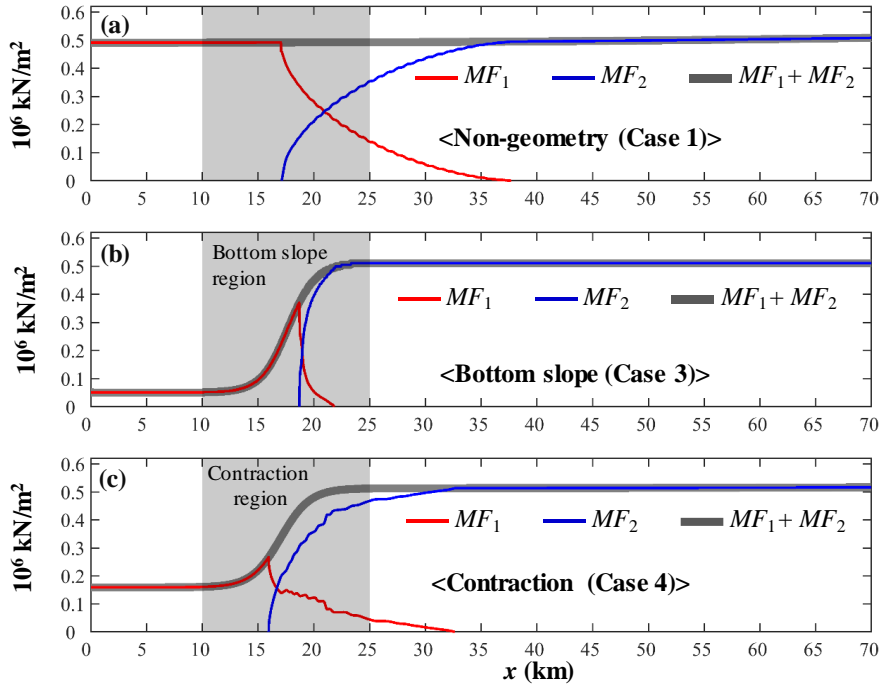


**Fig. VI-2** The variations of the tidally averaged of the momentum flux for fresh layer ( $MF_1$ ) and for salt layer ( $MF_2$ ) through whole lateral cross section in 70 km distance around salt tip for three study cases. The formula computed  $MF_1$  and  $MF_2$  are presented in equation (6.1) and (6.2).

Fig. VI-2(a)-(c) shows that the momentum fluxes much vary in the slope region or the contraction region than those in the non-geometry case. Without the existence of the geometric feature (case 1), the  $MF_1$  and  $MF_2$  of each layer mostly be constant until the fresh layer meets the salt layer (Fig. VI-2(a)). For case 1, the total momentum flux ( $MF_1 + MF_2$ ) of for whole domain is mostly constant at  $0.52 \times 10^6 \text{ kN/m}^2$  for 70 km of the upstream. Hence, there is not much large the variation in the total momentum of the fluid without the effects of the geometry.

In contrast, for bottom slope case (case 3), the momentum flux of the fresh layer ( $Mf_1$ ) is just at about  $0.05 \times 10^6 \text{ kN/m}^2$  in the 10 km distance from the river boundary, but it increases over ten times in the bottom slope region (Fig. VI-2(b)). However, between  $x = 17 \text{ km}$  and the end of the slope ( $x = 25 \text{ km}$ ),  $MF_1$  gradually decrease due to the presence of the salt layer on the bottom. The momentum flux of the salt layer is mostly constant  $0.52 \times 10^6 \text{ kN/m}^2$  between 25 km to downstream boundary, but from  $x = 25 \text{ km}$  to the end of the salt wedge, the  $MF_1$  gradual decrease to zero. The total momentum flux for whole water column ( $MF_1 + MF_2$ ) changes significantly in the distance from  $x = 10 \text{ km}$  to  $x = 25 \text{ km}$  (Fig. VI-2(b)). Especially, the momentum flux of the fresh layer (before meets the salt layer) is significantly induced due to the slope.

The two components of the momentum fluxes ( $MF_1 + MF_2$ ) for case 4 varies in similar trend to that of case 3 (Fig. VI-2(b) and (c)). For case 4 (the contraction case), in the upstream of the contraction ( $0 < x \leq 10 \text{ km}$ ), the  $Mf_1$  is mostly constant at  $0.17 \times 10^6 \text{ kN/m}^2$ , and in downstream of the contraction from  $x = 25$  to  $x = 70 \text{ km}$ ,  $Mf_1$  remains at  $0.52 \times 10^6 \text{ kN/m}^2$ . In two above regions, the

bottom is flat and the width is constant. Between  $x = 10$  km to  $x = 25$  km where the width is contracted,  $MF_1$  of case 4 varies from  $0.17 \times 10^6$  kN/m<sup>2</sup> to  $0.52 \times 10^6$  kN/m<sup>2</sup> while  $Mf_2$  decrease from  $0.52 \times 10^6$  kN/m<sup>2</sup> to zero (Fig. VI-1(c)). Therefore, the energy of the fresh layer (represented by the  $MF_1+MF_2$ ) increase by 50% in the contraction region, compared with that at the river boundary ( $x = 0$  km).

Therefore, Fig. VI-2 show that the contraction or the slope causes the change of the energy in the channel. As a results, the energy of the fresh water is enhanced when the freshwater is transported to downslope or over the expansion region (the width is expanded seaward). Besides, the energy of the salt water become weaker on the positive slope or in the contraction region. Hence, the time the fresh flow over the salt flow in the contraction/bottom region is longer, compared to the case without the effect of the geometry.

### ***6.2.3 The effects of the geometry on the flows, the friction and the existence of the overturn***

The presence time of the exchange flow in the mild bottom slope or the gradual contraction regions seem to be prolonged in the geometric region because the geometry makes the variations in flow. In generally, the variations of the flow under effects of the bottom slope are the contraction region are presented in the equations (1.1) – (1.4) (Chaudhry, 2008; Armi, 1986; Zhu and Lawrence, 2000). In specific, for the bottom slope case with the constant with (Fig. I-3(a)), the equation for the salt layer (equations (1.2) and (1.4)) are rewritten as



$$\frac{\partial u_2}{\partial x} = \underbrace{\frac{1-Fr_1^2}{1-G^2} \frac{u_2}{D_2} \frac{dz_b}{dx}}_{\langle \text{Bottom effect} \rangle} + \underbrace{f_2 \frac{dE_1}{dx}}_{\langle \text{Friction effect} \rangle}, \quad (6.3)$$

$$\frac{\partial D_2}{\partial x} = - \underbrace{\frac{1-Fr_1^2}{1-G^2} \frac{dz_b}{dx}}_{\langle \text{Bottom effect} \rangle} + \underbrace{f_4 \frac{dE_2}{dx}}_{\langle \text{Friction effect} \rangle}, \quad (6.4)$$

and the equation for the salt layer (equations (1.2) and (1.4)) for the variation of the width with the flat bottom (Fig. I-3(b)) are rewritten as:

$$\frac{\partial u_2}{\partial x} = - \underbrace{\frac{1-Fr_1^2 \left(1 + \rho_1 D_2 / \rho_2 D_1\right)}{1-G^2} \frac{u_2}{W} \frac{dW}{dx}}_{\langle \text{Width effect} \rangle} + \underbrace{f_2 \frac{dE_1}{dx}}_{\langle \text{Friction effect} \rangle}, \quad (6.5)$$

$$\frac{\partial D_2}{\partial x} = \underbrace{\frac{G^2 - Fr_1^2 \left(1 + \rho_1 D_2 / \rho_2 D_1\right)}{1-G^2} \frac{D_2}{W} \frac{dW}{dx}}_{\langle \text{Width effect} \rangle} + \underbrace{f_4 \frac{dE_2}{dx}}_{\langle \text{Friction effect} \rangle}, \quad (6.6)$$

and after some rearrangement, the equation (6.4) and equation (6.6) become

$$1-G^2 = - \frac{\left(1-Fr_1^2\right) \frac{dz_b}{dx} + f_4' \frac{dE_2}{dx}}{\frac{\partial D_2}{\partial x}}, \quad (\text{for bottom slope}) \quad (6.7)$$

$$1-G^2 = \frac{G^2 - Fr_1^2 \left(1 + \rho_1 D_2 / \rho_2 D_1\right)}{\frac{\partial D_2}{\partial x}} \frac{D_2}{W} \frac{dW}{dx} + f_4' \frac{dE_2}{dx}. \quad (\text{for variation of the width})$$

(6.8)

The equations (6.3)-(6.6) could not be solved directly to tell how much the velocity or the depth change due to the bottom slope or the contraction. However, these equations demonstrate that the velocity ( $u_2$ ) and the thickness of the salt layer ( $D_2$ ) should be changed due to the bottom slope/the contraction of the width and the friction. That's why the flow and salinity structure ( $u, w$ ) at each flow mode for the bottom slope and the contraction regions (Fig. IV-4; Fig. V-3) are

far different from those for the non-geometry regions (Fig. IV-1). Especially, among three kind of the estuary, the well mixing as the overturns are just observed for the contraction or the bottom slope (Fig. IV-8(a<sub>2</sub>)-(b<sub>2</sub>), Fig. V-4, Fig. V-2).

Normally, the flow of the two-layer fluid is strongly mixed when the hydraulic jump occurs ( $G^2 = 1$ ) (Armi, 1986). According to Armi, (1986), hydraulic jump may exist since the flow get the geometrical critical condition such as the  $dz_b/dx = 0$  or  $dW/dx = 0$ . For the mild slope or the gradual contraction as in experiment 2 and experiment 3 (Fig. III-1(b)-(d)), the  $dz_b/dx$  and  $dW/dx$  could not be zero in order to the hydraulic jump occurs. However, the equations (6.7) and (6.8) show that another way for development of the hydraulic jump ( $G^2 = 1$ ) is that  $\partial D_2/\partial x$  is infinity. The infinity of  $\partial D_2/\partial x$  may be observed at the overturn of the mild slope (Fig. IV-1(e)) or the overturn in the gradual contraction (Fig. V-1) and therefore, the overturns at the salt tip are the signal for the hydraulic jump.

In order to the mass from salt flow is discharged into the fresh flow by an overturns, the freshwater flow and the salt flow should in the opposite direction. For this reason, the overturns are just observed in at near slacks (Fig. IV-8(a<sub>2</sub>)-(b<sub>2</sub>) and Fig. IV-8(a<sub>5</sub>)-(b<sub>5</sub>)) on the mild slope or in the flood (Fig. V-3(a)-(b)) in the gradual contraction because at those instants, the flows are in the exchange mode. Further, the overturning flow could not occur near full ebb (Fig. IV-8(a<sub>1</sub>)-(b<sub>1</sub>)) or full flood (Fig. IV-8(a<sub>4</sub>)-(b<sub>4</sub>)) because during those times, the flows at the salt tip are in uni-directional mode.

### 6.3 The process for the development of the hydraulic jump in the salt tip

#### 6.3.1 *The convergence of the energy under effects of the geometry and the fresh water.*

Many works (e.g., Klymak et al., 2007; Masunaga et al., 2015, Lamb, 1997) found that under the effects of the significant shear flow during the shoaling process of the density front or the front of tide, the energy is much converged in both mass and velocity at troughs of the fronts (Klymak et al., 2007; Masunaga et al., 2015). Therefore, in order to prove that the shear flow is able to make the similar process at the salt tip front during the propagating time of the exchange flow as the density current in the contraction/bottom regions, the pressure momentum flux ( $Mf_{2p}$ ) and kinetic momentum flux ( $Mf_{2u}$ ) around the salt layer over three study cases are compared. At each study cases, the both momentum flux for the exchange mode and uni-directional mode are respectively investigated.

In which, for case 1 (non-geometry effect), we investigate the kinetic momentum flux for salt layer at three moments including: time ( $N_1$ ), time ( $N_2$ ) and ( $N_3$ ). At time ( $N_1$ ) (at the slack before flood), the flow is in the exchange flow mode (Fig. IV-1(e)) but the overturn is not observed (Fig. IV-2(a)-(b)). At the last two time instants (time ( $N_2$ ) and ( $N_3$ )), the flow is in the uni-directional mode (Fig. IV-1(e)). For case 3 (bottom slope effect, 3D), we investigate momentum flux at three times that are: time ( $T_2$ ), time ( $T_4$ ) and time ( $T_5$ ). Among three moments, time ( $T_2$ ) is at the slack after flood and time ( $T_5$ ) is at the slack before flood, and the flows at both those moments are in the exchange flow mode (Fig. IV-7(a)). In contrast, time ( $T_4$ ) is at near full flood and at that time, the flow

is in the uni-directional mode (Fig. IV-7(a)). For last case (Width contraction effect, case 4), the  $Mf_2$  for the flows at the exchange flow mode and the uni-directional mode are investigated at time  $(C_1)$  and time  $(C_1)$ , respectively (Fig. V-2(a)). The variations of the pressure momentum fluxes ( $Mf_{2p}$ ) and the kinetic momentum fluxes ( $Mf_{2u}$ ) around the salt layer at eight time instances are shown in Fig. VI-3. Two components of the momentum fluxes are computed based on the equation (2.9) in section 2.1.

For the non-geometry case, Fig. VI-3(a)-(b) shows that the  $Mf_{2p}$  and  $Mf_{2u}$  at time instants gradually decreases from the downstream ( $x = 20$  km) to the end of the salt tip. The salt tip at time  $(N_1)$  ends at  $x = 15.80$  km and at time  $(N_2)$ , the salt tip ends at  $x = 15.85$  km. The end of the salt tip at time  $(N_3)$  is at  $16.9$  km. Especially, in  $0.5$  m distance from the salt tip, the  $Mf_{2p}$  and  $Mf_{2u}$  at time instants decrease without the existence of the any small bounce back. Then, it can be concluded that the momentum flux is not be accumulated at the salt tip at these time instants, and without the accumulation of the  $Mf$ , the increase in the thickness as well as the velocity are not observed at three time instants (Fig. VI-2).

For the bottom slope case (case 3), Fig. VI-3(b) and (c) shows that the both pressure momentum flux ( $Mf_{2p}$ ) and the kinetic momentum fluxes ( $Mf_{2u}$ ) for salt layer decrease in a distance from  $x = 20$  km to upstream for all three moments. However, at near the end of the salt layer for each time,  $Mf_{2p}$  has experienced a small bounce back before decrease to zero (Fig. VI-3(c)). At time  $(T_2)$  and  $(T_4)$ , the bounce back of the  $Mf_{2p}$  is observed in a small distance after  $x = 19.50$  km

and  $x = 18.0$  km, respectively, and the small bounce back of the  $Mf_{2p}$  at time ( $T_5$ ) is observed in a short distance from  $x = 16.95$  km (Fig. VI-3(c)).

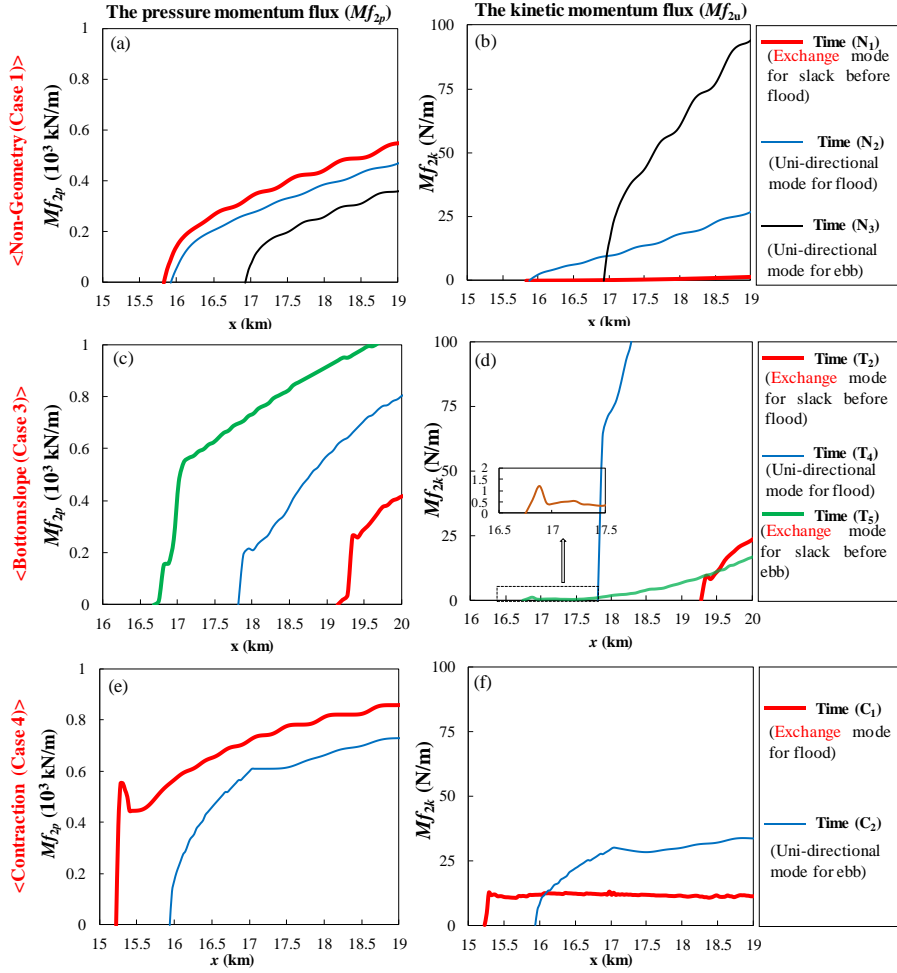


**Fig. VI-3** The variations of the pressure momentum flux and kinetic momentum flux for salt layer in a 4.0 km distance around salt tip over three study cases (case 1, case 3 and case 4). Two component of the momentum fluxes is computed based on the equation (2.9) in section 2.1. Time ( $N_1$ ), ( $N_2$ ) and ( $N_3$ ) are depicted in Fig. IV-1(e). Time ( $T_2$ ), ( $T_4$ ) and ( $T_5$ ) are depicted in Fig. IV-8(a). Time ( $C_1$ ) and ( $C_2$ ) are depicted in Fig. V-2(a).

Among three instants, the slight recovery of the  $Mf_{2p}$  around the salt tip at time (T<sub>4</sub>) in Fig. VII-3(c) is not able to show for the accumulation of the energy because that increase of the  $Mf_{2p}$  is not along with any the recovery of the  $Mf_{2u}$  observed at that time (Fig. VI-3(d)). Fig. VI-3(d) shows that at time (T<sub>4</sub>),  $Mf_{2u}$  significant decrease a distance from  $x = 18.2$  km to  $x = 17.7$  km. A small increase of the  $Mf_{2p}$  observed around the salt tip at that time (time (T<sub>4</sub>)) in Fig. VI-3(c) seems to be from an increase in the thickness of the salt tip from previous period (from time (T<sub>1</sub>) to (T<sub>3</sub>)) (Fig. IV-8(c<sub>2</sub>), (c<sub>3</sub>) and (c<sub>4</sub>)).

In contrast, the slight recovery of the  $Mf_{2p}$  and  $Mf_{2u}$  around the salt tip at time (T<sub>2</sub>) and (T<sub>5</sub>) in Fig. VII-3(c) and (d) show that in the time near the slacks, the energy is slightly accumulated. According to Friedrichs and Wright (1995) and Lamb (1997), the concentration of the energy in a small mass leads to rise of the height of the wave. Therefore, the rise of the salt tip thickness at time (T<sub>2</sub>) and (T<sub>5</sub>) (Fig. IV-8(c<sub>2</sub>) or (c<sub>5</sub>)) seems to result from the accumulation of pressure momentum flux (Fig. VI-3(c) and (d)).

For case 4 (the contraction case), the accumulation of the energy in the exchange flow mode is observed at time (C<sub>1</sub>) (Fig. VI-3(e) and (f)). At time (C<sub>1</sub>), both  $Mf_{2p}$  and  $Mf_{2u}$  has experienced a small bounce back before decrease to zero (Fig. VI-3(e)-(f)). Therefore, similar to case 3, a small recovery of the  $Mf_{2p}$  and  $Mf_{2u}$  observed at that time (time (C<sub>1</sub>)) around  $x = \text{km}$  seems shows for the accumulations of the energy at the salt tip which induces for a rise in the thickness and the size of the streamwise flows at the salt tip shown in Fig. V-3(a), (c). In contrast, the accumulation of the  $Mf_{2p}$  and  $Mf_{2u}$  could not be observed at

time ( $C_2$ ). At time ( $C_2$ ), from the  $x = 15.2$  km to  $x = 15.9$  km, the  $Mf_{2p}$  and  $Mf_{2u}$  gradually decrease to zero (Fig. VI-3(e)-(f)).

Therefore, the accumulations of the energy are observed at the exchange flow mode. Without the existence of the exchange flow mode, the energy could not be accumulated in the salt tip. The accumulation of the energy at the salt tip seem to be significantly affected by the freshwater. Masunaga et al., (2017) and Wallace and Wilkinson, (1988) reported that the convergence of the horizontal flow or the strong mixing can be induced from the interaction between the run-up bore or density front with the backflow from previous shoaling process. Although the salt tip doesn't have the backflow from previous shoaling process but it has the seaward river flow.

According to Gu & Lawrence, (2005), the friction between two-layer flow and the friction of the bottom are very important to the rate of the exchange flow (Gu & Lawrence, 2005). For the two-layer exchange without the upstream depth as the internal bore, Masunaga et al., (2017) noticed that the shear flow should exist long enough to the internal bore be generated. Among four time moments of the exchange flow mode presented in Fig. VI-3, the accumulation of  $Mf$  is not observed in the slack before flood for case 1 (time ( $N_1$ )) (Fig. VI-3(a), (b)). In case 1 (non-geometry effect), the time for the exchange mode is very short and even the shortest among three study case (Fig. VI-1). The exchange flow in case 1 just exist in few minutes ( $t/T < 0.03$ ) near slack before or after flood (Fig. VI-1). In contrast, the exchange flows in the other study cases exists from  $0.06$   $t/T$  to more than  $t/T = 0.52$  for a tidal cycle (Fig. VI-1).

### ***6.3.2 The existence of the hydraulic jump at the front of the salt tip***

Since the energy is accumulated at the salt front, the density currents observed salt tip seems to be a special limiting form of the density current that is the density jump by the significant rise in the thickness of the salt tip and velocity. Benjamin, (1968) and Baines, (1995) supposed that the energy and mass of the lower layer with supercritical head is dissipated into the upper layer by a passing through a jump. According to Lean & Whillock (1965), it is possible for the existence of the hydraulic jump at the density current head since the Froude number observed at the front of density current is larger than 1. Therefore, to determine the presence of the hydraulic jump at the front of the salt tip we investigate the energy state around the salt tip.

#### ***6.3.2.1 The comparison between the composite Froude number and the front Froude number methods***

In order to prove that the transfer of the energy from the salt layer to the fresh layer at the internal bore is through a jump as Benjamin, (1968) mentioned, both the Froude number ( $Fr_f$ ) (Equation (2.10)) and the composite Froude number ( $G^2$ ,  $Fr^2_1$ ,  $Fr^2_2$ ) (Equation (2.11)) are investigated. While the  $Fr_f$  is applied to quantify the state of internal bore front, the composite Froude number ( $G^2$ ,  $Fr^2_1$ ,  $Fr^2_2$ ) is applied to quantify the state of the energy for two-layer flow in the region from the salt head to the downstream. In our research, the elevation of the interface between the fresh layer and salt layer is determined in similar way to Geyer and Ralston (2015). In which, the interface of the two layers is the mid-point the locations between the averaged of the velocity and averaged of the



salinity. We investigate the state of the flow for four cases: case 1 (non-geometry effect, 3D model), case 2 (Bottom slope effects, 2D model), case 3 (Bottom slope effect, 3D model) and case 4 (the width contraction effect, 3D model). More information about the setup for four study cases is introduced in chapter II.

Firstly, we quantify the composite Froude number ( $G^2$ ,  $Fr^2_1$ ,  $Fr^2_2$ ) for 2D model (case 2) in 1.0 km distance around the salt tip (just for regions from the end of the salt tip to downstream where two-layer flow exists) at three moments that are: time ( $S_3$ ), time ( $S_5$ ) and ( $S_7$ ). In which, at time ( $S_3$ ) ( $t/T = 2.53$ ), the flows are in the slack before flood, and for the other times, the flows are in the uni-directional mode for flood or for ebb (Fig. IV-4(e)). Among three time instants, the internal bore along with overturn just is observed in the exchange flow mode at time ( $S_3$ ) (Fig. IV-5(a<sub>3</sub>)-(c<sub>3</sub>)). The results of the composite Froude number ( $G^2$ ,  $Fr^2_1$ ,  $Fr^2_2$ ) in at three moments are presented respectively in Fig. VI-4. Further, we quantify the maximum of the three Froude number components related to the composite Froude number ( $G^2$ ,  $Fr^2_1$ ,  $Fr^2_2$ ) and the Froude number of the front ( $Fr_f$ ) at the salt tip over 2.5 tidal cycles ( $1.5 \leq t/T < 4.0$ ). The results of the Froude numbers over 2.5 tidal cycles are presented respectively in Fig. VI-5.

Fig. VI-4(a) shows that at  $t/T = 2.96$  (time ( $S_3$ )), the salt wedge is end at  $x = 20.13$  km. Near the end of the salt tip the three components of the composite Froude number ( $G^2$ ,  $Fr^2_1$ ,  $Fr^2_2$ ) are far smaller than unity and therefore, meaning that the flow in the fresh layer and salt layer are in the subcritical state. In contrast, from the downstream near the end of the salt wedge at  $x = 19$  km for time ( $S_5$ ) (in flood) and at  $x = 18.87$  km for time ( $S_7$ ) (in ebb), both the internal Froude number for two layers ( $Fr^2_1$ ,  $Fr^2_2$ ) and composite Froude number ( $G^2$ )

significantly overcome the unity in 100 m distance near the end of salt tip (Fig. VI-4 (b)(c)). Therefore, by using the composite Froude number method, we can conclude that the flow are in the supper critical state for both two-layer flows around the salt tip at time ( $S_5$ ) and time ( $S_7$ ).

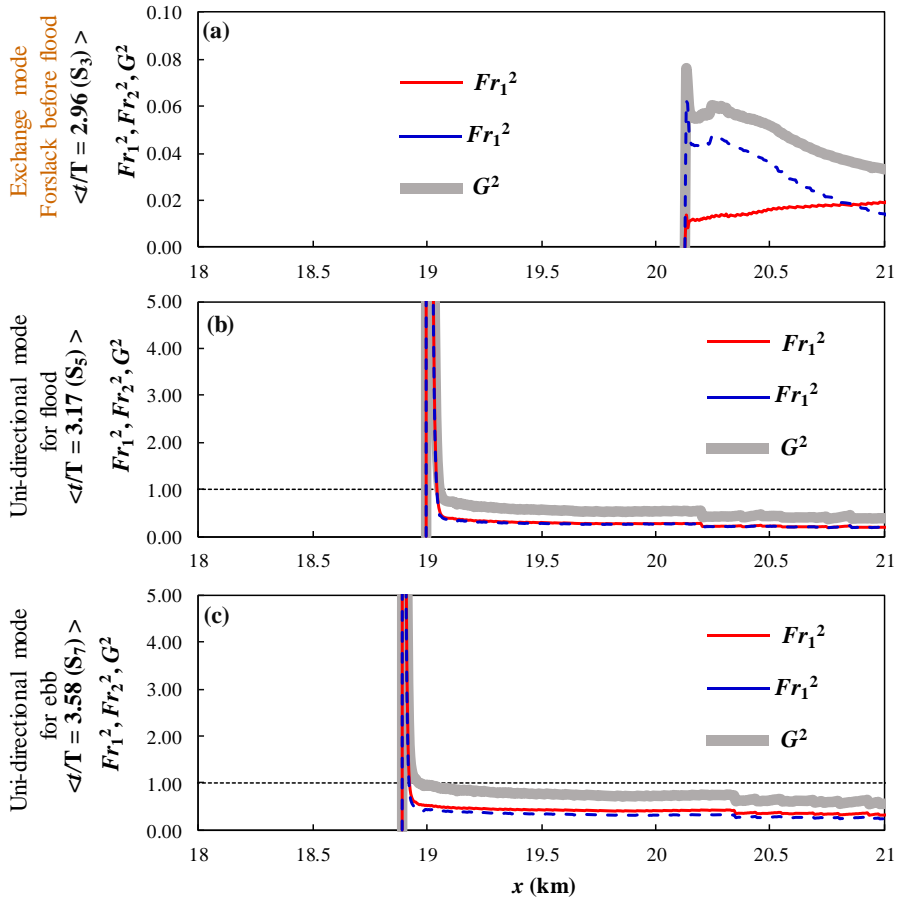


**Fig. VI-4** The internal Froude number of the freshwater layer ( $Fr_1^2$ ) and saltwater layer ( $Fr_2^2$ ) and the composite Froude number ( $G^2$ ) in the 3.0 km section around the salt tip for case 1 (the bottom slope for 2D model). Time ( $S_3$ ), time ( $S_5$ ) and time ( $S_7$ ) are depicted in Fig. IV-4(e).

Fig. VI-5(a) shows that the composite Froude number ( $G^2, Fr_1^2, Fr_2^2$ ) are bigger than unity in the time for the uni-directional flow mode and smaller than unity in the time for the exchange flow mode. Therefore, the composite Froude

numbers indicate the supercritical state for flows in flood or ebb but indicate the subcritical state for flow during the slacks (Fig. VII-5(a)). However, since the overturn as well as internal bore from the accumulations of the momentum flux are just observed in the slacks (Fig. IV-5(a<sub>3</sub>)-(c<sub>3</sub>); Fig. IV-5(a<sub>6</sub>)-(c<sub>6</sub>)), the composite Froude number seems to not predict (in accuracy) the state of the flow for the salt tip region. At the salt tip region, the density difference between the saltwater layer and the freshwater layer are not large and then, the reduced gravitational acceleration ( $g' = g \frac{\rho_2 - \rho_1}{\rho}$ ) near the end of the ebb is mostly equal zero. As a result, the composite Froude numbers near the end of the salt tip suddenly increase in the flood or ebb as illustrated in Fig. VI-4 and Fig. VI-5(a). Therefore, the composite Froude number ( $G^2, Fr^2_1, Fr^2_2$ ) seem to be not suitable for qualifying the state of the flow for low stratification region such as salt tip although the density of salt tip is composed by two-layer flow.

In contrast to composite Froude number, the results in Fig. VI. 5(b) shows that  $Fr_f$  may show obsoletely the difference in the state of the flow between the exchange flow mode and the uni-directional mode. For instance,  $Fr_f$  is mostly smaller or equal unity from  $2.93 \leq t/T < 3.35$  and during that period, the flow is in the uni-directional mode. During the exchange mode for ebb of  $2.87 \leq t/T < 2.93$  or for flood of  $3.35 \leq t/T < 3.41$ , the  $Fr_f$  is bigger than unity. Therefore, the variation of the  $Fr_f$  in the Fig. VI-5(b) is completely coincided with the time for the presence of internal bore and overturn at the salt tip as well as the hydraulic jump at the front of the density current in previous researches (e.g., Benjamin, 1968 and Baines, 1995).

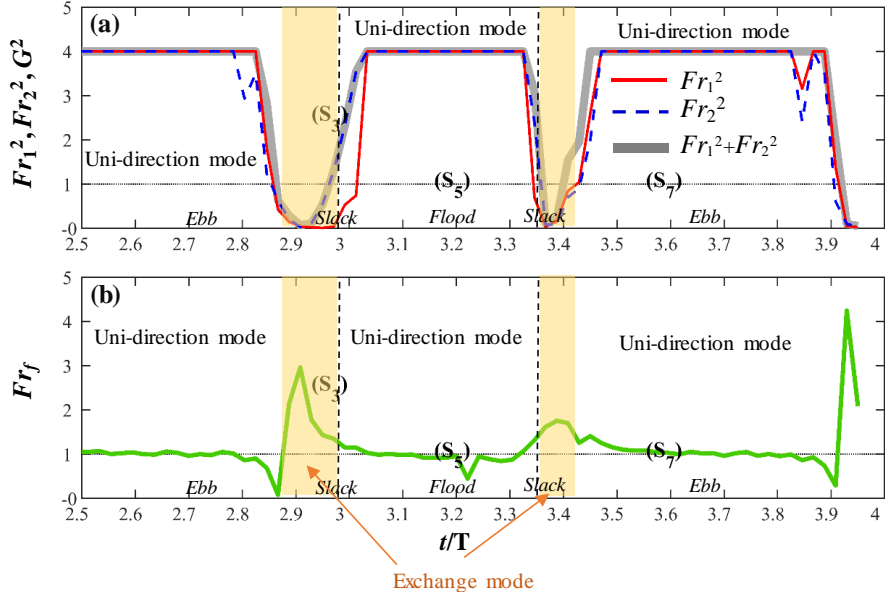


**Fig. VI-5** The variations of the Froude numbers at the salt tip for 2.5 tidal cycles for case 2 (the bottom slope for 2D model). (a) The maximum of the internal Froude number for the freshwater region ( $Fr_1^2$ ) and saltwater region ( $Fr_2^2$ ) and  $G^2$  around the salt tip. (b) The Froude number of the front ( $Fr_f$ ). Time ( $S_3$ ), time ( $S_5$ ) and time ( $S_7$ ) are depicted in Fig. V-1(e). Yellow area show the exchange flow mode depicted in Fig. V-1(e).

### 6.3.2.2 The hydraulic jump at the salt tip

Further, we apply the front Froude number method ( $Fr_f$ ), which already is applied to estimate the state of the front in Nash and Moum (2005) or Masunaga et al., (2015), to quantify the state of the energy at the salt front for three study cases simulating the processes in 3D model. Among three cases (case 1, case 3 and case 4), the existence of the internal bores with overturns are observed in the last two cases (Fig. IV-8(a<sub>2</sub>)-(c<sub>2</sub>) and Fig. V-3(a)-(c)). In the first case (the non-geometry case), the internal bore is not observed in even for the exchange mode (Fig. IV-2(a)-(c)). We use the Froude number of the front ( $Fr_f$ ) to identify the existence of the hydraulic jump. The results of the Froude number of the front for three study cases are shown in Fig. VI-6.

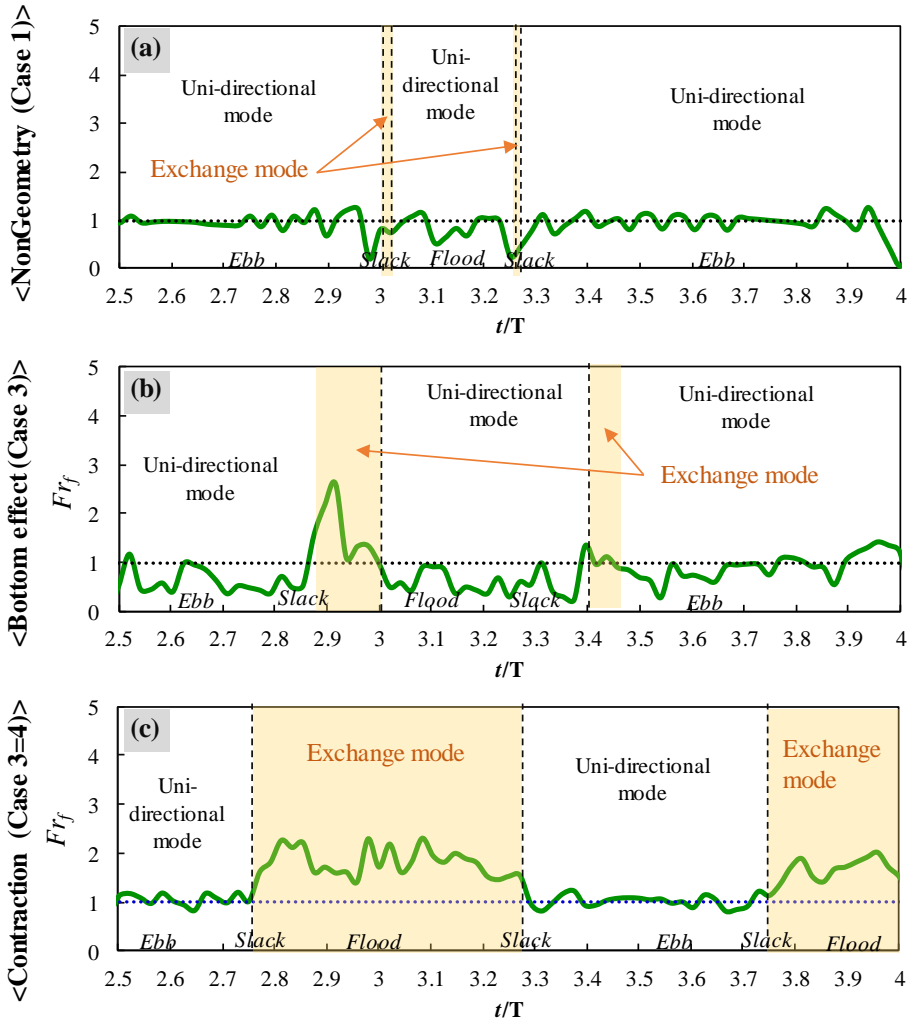


**Fig. VI-6** The variations of the front Froude number ( $Fr_f$ ) of the salt front over 2.5 tidal cycles for three study cases: case 1 (non-bottom slope and contraction), case 3 (bottom slope case, 3D), case 4 (contraction case, 3D) and Yellow area show the exchange mode.

For the non-geometry case (case 1), Fig. VI-6(a) show that  $Fr_f$  is nearly equal unity over 1.5 tidal cycle. Evenly, during the slack before flood or during slack after flood,  $Fr_f$  is far smaller unity (Fig. VI-6(a)) and therefore the density current exists during that time seem to be a density current with the subcritical head (Fig. IV-2(a)-(c)). Without the existence of the hydraulic jump, the internal bore could not develop at the salt tip in case 1 (Fig. IV-2(c)).

For the bottom slope case (case 3), Fig. VI-6(b) shows that the flow at the front is in the supercritical state ( $Fr_f > 1$ ) during the slack after ebb ( $2.87 < t/T \leq 3.0$ ) and slack after flood ( $3.4 < t/T \leq 3.46$ ). For the uni-directional flow mode for ebb ( $2.5 < t/T \leq 2.87$ ) or flood ( $3.0 < t/T \leq 3.4$ ), the  $Fr_f$  number varies between zero to unity implying for the existence of the subcritical state. Similarly, the  $Fr_f$  for case 4 (the contraction case) fluctuates around the unity during the uni-directional mode ( $3.28 < t/T \leq 3.75$ ) (Fig. VI-6(c)). In the exchange flow mode ( $2.76 < t/T \leq 3.28$ ), the  $Fr_f$  number is bigger than 1 (Fig. VI-6(c)). Therefore, since the  $Fr_f > 1$ , the results in Fig. VI - 6(b) and (c) shows that the hydraulic jump may occur in the exchange flow mode on the mild bottom slope or in the gradual contraction. Therefore, during that time for presence of the hydraulic jump, the density currents exist with the super critical head (Benjamin, 1968; Xu, 1991). For the super critical head, the head of the density front exists as the breaking of the head wave (Benjamin, 1968).

#### **6.4 The existence of the overturns under the effects of the tide amplitude and the river discharge**

The presence time for the hydraulic jumps changes due to the tidal amplitude and the river inflow rate. The results in the experiment 4 shows that the presence time for the exchange flows in the geometric regions are much affected from the changes in size of the tidal amplitude ( $\eta_0$ ) or the size of the river inflow rates change ( $u_0$ ). However, in the regions with flat bottom and constant width, when the variations in the tidal amplitude or the river inflow at the boundary conditions could not result in the rise in the presence time for the

exchange flow. Fig. VI-7(a)-(b) show that in the non-geometric region, the exchange flow appears two times in the tidal cycles that are slack before flood (SBF) and after flood (SAF). Both the presence time for the exchange flow of slack before flood ( $t_{\text{SBF}}$ ) and of the slack after flood ( $t_{\text{SAF}}$ ) are very short ( $t/T \leq 0.03$ ) and during that time, the overturns are not observed (Fig. VI-7(a)-(b)).

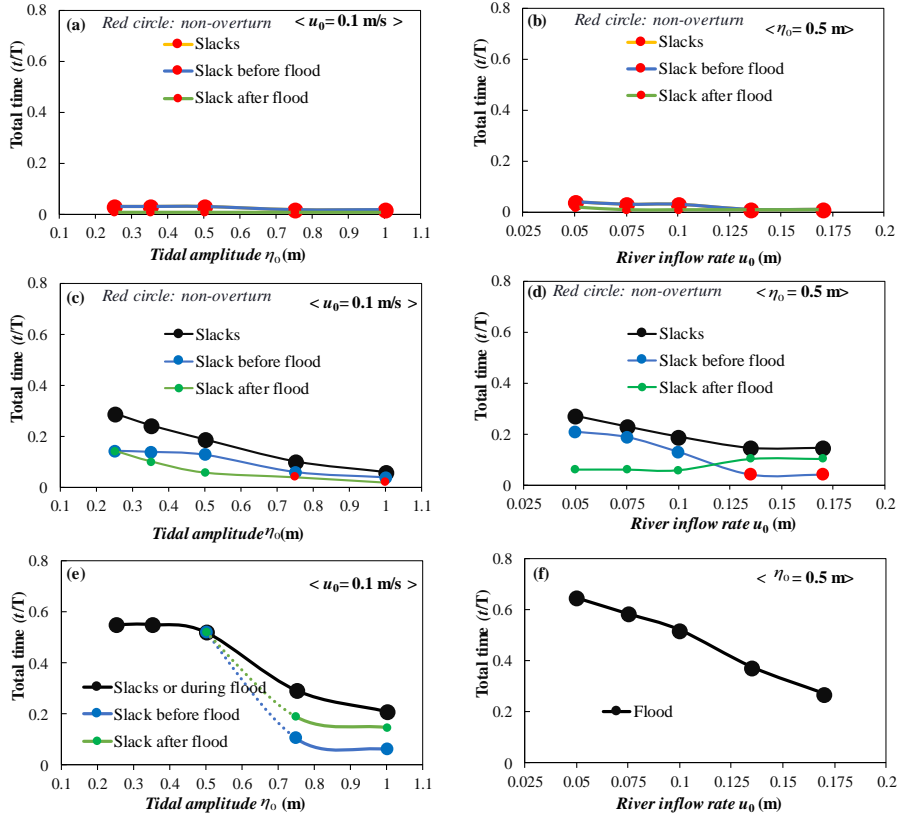


**Fig. VI-7** The total presence time for the existence of the exchange flow in the each slack or in the flood (experiment 4). (a) For the case with the river boundary current  $u_0 = 0.1$  m/s. (b) For the case with the tidal boundary amplitude  $\eta_0 = 0.5$  m/s. Red circle show for the overturn doesn't exist during this period.

In contrast, Fig. VI-7(c)-(f) show that increased tidal amplitude or river flow rate resulted in the lesser time for the exchange flow for the geometric region. For the bottom slope, both  $t_{\text{SBF}}$  and  $t_{\text{SAF}}$  decreases due to increasing in the

$\eta_0$  (Fig. VI-7(c)). For the scenarios with the 0.25 m of  $\eta_0$ ,  $t_{SBF}$  or  $t_{SAF}$  equals approximately 0.15  $t/T$  but they are smaller than 0.05  $t/T$  for the scenarios with 1.0 m of  $\eta_0$ . Especially, for the scenario of 0.75 m  $\eta_0$  and of 1.0 m  $\eta_0$ , the overturn is not observed during the slack after flood (Fig. VI-7(c)).

For the effects of the river inflow rate, Fig. VI-7(d) show that the total time for the exchange flow in the slacks decreases between 0.27  $t/T$  and 0.15  $t/T$  due to the increase in the river inflow rate in the range from  $u_0 = 0.05$  m/s to  $u_0 = 0.17$  m/s and the overturn are observed in the tidal cycle for whole five levels of the flow rate. The  $t_{SAF}$  slightly increases but the  $t_{SBF}$  decreases over five levels of the  $u_0$  (Fig. VI-7(d)). The overturn could not be observed for the scenarios of 0.135 m of  $u_0$  and of 0.17 m of  $u_0$  since the time for the exchange flow is are very small ( $t_{SBF} \leq 0.05$   $t/T$ ).

Similar to the bottom slope region, the existence time of the exchange flow in the contraction decreases when the river inflow rate or the tidal amplitude at the boundary increases (Fig. VI-7(e), (f)). At the first three levels of  $\eta_0$  ( $\eta_0 = 0.25$  m; 0.35 m; 0.5 m), the exchange flow may exist during the flood ( $t/T \leq 0.52$ ) (Fig. VI-7(e)). However, at two last levels of the  $z_0$  ( $z_0 = 0.75$  m; 1.0 m)), the exchange flow just exists during the slack before flood or after flood (Fig. VI-7(e)).

For the scenarios with  $\eta_0 = 0.5$  m, the increase in the river inflow rate results in the decreasing in the time for the exchange flow (Fig. VI-7(f)). Fig. VI-7(f) shows that, the exchange flow mode may exist up to 0.64  $t/T$  for the scenarios with  $u_0 = 0.05$  m/s, but, the time for existence of the exchange flow for



the scenarios with this river flow rate is about  $0.27 \text{ t/T}$ . The decrease of the presence time for exchange increase doesn't affect to the existence of the overturn since the overturns at each the scenarios still observed (Fig. VI-7(f)).

Therefore, with any tidal amplitude or the river inflow rate, the overturn as terms of the hydraulic jump could not be observed in the no-geometry (Fig. VI-7(a)(b)). In the bottom slope or the contraction region, the overturns may appear and exist for a long time for the weak tidal amplitude (Fig. VI-7(c)(e)). River flow affect directly to the time for presence of the overturn, when overturns seem to be exist longer for the small river flow magnitude than for the large river flow magnitude (Fig. VI-7(d)(f)).

## **6.5 Summary**

Therefore, the hydraulic jumps occur not only around the narrowest region of the constrictions or at the crest of the sills (Armi and Farmer, 1986), but also occur on the mild slope or the gradual contraction. The gradual slope or the gradual variation of the width may induce the increase in the momentum flux for the freshwater layer and reduce in the momentum flux for the saltwater layer. As a results, the ability of the fresh to interfere with the upstream movement of the flood flow is enhanced. For detail, under effect of the river flow and the support of the geometry features, the time for the existence of the shear flow at the salt tip becomes longer.

Similar to the observation of the previous works for the shoaling process of the density front on the large slope (e.g., Lamb, 1997, Masunaga et al., 2017; Klymak et al., 2007), the upstream propagation for the shear flow at the salt tip

may lead to the convergence of the energy at the front of the salt tip in the mass and the velocity. As a result, the thickness of the salt tip increase and the form of the salt tip is similar to the form internal bore observed on the coastal region (Masunaga et al., 2015). Besides, since the energy is converged as the velocity for a long time enough, the state of the energy may change to the supper critical state ( $Fr_f > 1$ ) and then the energy is dissipated. The dissipation of the energy from the salt water to the fresh water at the salt tip lead to the generation of the vertical mixing as the overturn, similar to the mixing as the overturn form observed on the coastal region (Masunaga et al., 2015). The effects of the freshwater flow and the geometry as well the processes for the development of hydraulic jump are summarized in Fig. VI-8.

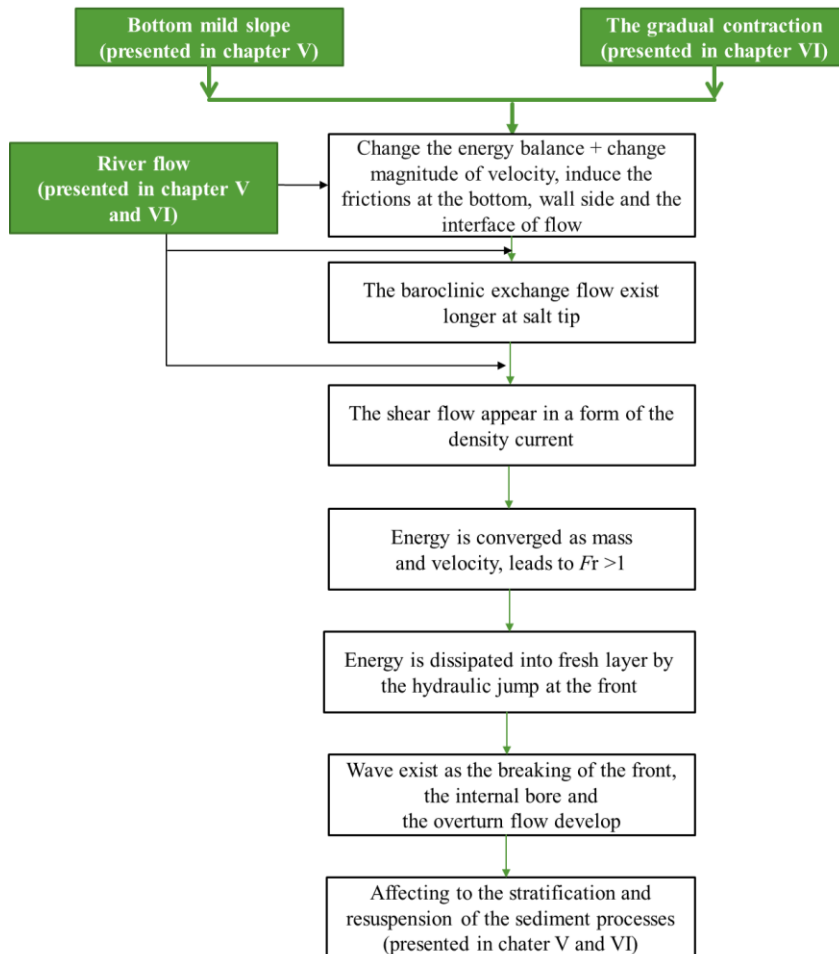


**Fig. VI-8** The sketch of effects of the contraction and bottom slope as well as the process for development of the overturn as a hydraulic jump in translation.

Further, the impacts of the overturn as a hydraulic jump in the mixing and stratification and the sedimentary process at the salt tip are partly similar to the impacts of tidal straining which normally observed in many partially mixed zones. According to Simpson et al. (1990), the stratified process in partially mixed zones may be driven by the vertically shear flow along with the longitudinal salinity gradient and that process is called the strain-induced periodic stratification (SIPS). However, while tidal straining and stratification limits mixing during ebb and reduces the stratification in flood (Geyer et al.,

2000; Rippeth et al., 2001; Burchard & Hofmeister, 2009), the overturn from the hydraulic jump observed at the salt tip raises mixing during the slack before flood or slack before ebb. Besides, similar to the tidal straining, the mixing in those periods may promotes the resuspension of the sediment. As the results, the sediment is significantly resuspended (Monismith et al. 1996; Nunes et al. 1989).

## CHAPTER SEVEN

### VII. SUMMARY AND RECOMMENDATIONS

#### 7.1 Summary

The thesis clarified the stratification and the sedimentary processes in the salt tip region under the effects of the two geometry features. One is the mild bottom slope, and the other is the gradual contraction of the width. The present study applies both 2D and 3D numerical models to simulate the hydrodynamic and the sediment transport. In first numerical experiment, the mild slope was set up as like as in the upstream Chesapeake Bay where the bottom elevation increases by 10 m in a 10 km distance (Sanford et al., 2001). In the last experiment, the bottom is set up as the lateral contraction instead of the vertical contraction as the mild bottom slope case. From the results of the two experiments, the main finding that is the overturns as the hydraulic jump may develop in the mild slope or the gradual contraction regions and theses processes generate the mixing and reduce the stratification at the salt tip. Results in more detail are as follows:

1. We found that the overturn may appear in the slack before flood ( $2.87 < t/T \leq 3.0$ ) or after flood ( $3.4 < t/T \leq 3.46$ ) (3D model) in the mild slope region. Similar to the flows in the upstream Chesapeake Bay where the salt tip is observed on the bottom slope (Sanford et al., 2001; North-Houde, 2001), the flows during the slacks are in the exchange mode as the form of the density currents with overturn at the head. In both 2D and 3D model, the overturn appears with accompanying by the increase in the thickness of the salt head

as the internal bore, similar to the internal bores observed on the coastal regions (Masunaga et al., 2015). The maximum thickness of the internal bores observed in 2D model is about 5.0 m and in 3D mode is about 4.0 m. In contrast to Sanford et al., (2001), we found that the overturn generates the mixing and reduces the stratification of the flow at the salt tip where the flows are normally in the strong stratification (Geyer, 1993). During the presence time of the overturn, the flows at the internal bore and the interface of the flow are well mixed ( $Ri < 0.25$ ) and the energy are highly dissipated ( $\epsilon > 10^{-6.0}$ ).

2. Not only in the mild bottom slope region, we found that the overturn may appear in but also the region where the width is gradually contracted. For similar setup to the mild bottom slope case, the overturn observed in the gradual contraction region may exist during flood ( $2.76 < t/T \leq 3.28$ ). During the flood, the streamwise currents and the vertical currents at the overturn may reach 10 cm/s and 0.5 cm/s, respectively.
3. Under effects of the vertical mixing, the sediment from the bottom is highly resuspended. We found that sediment is strongly resuspended by the overturns in both the gradual contraction and the mild slope regions. When the overturn exists, the sedimentary process at the salt tip is mostly driven by the size of the vertical mixing instead of driven by the tidal pumping or the estuarine circulation as the observations of the previous works (Jay & Musiak, 1994; Geyer, 2001; North & House, 2001). During the slack before flood, the sediment concentration has the good correlation with the vertical turbulent diffusive flux ( $R^2 = 0.70$ ) and the less correlation with the total sediment flux

( $R^2 = 0.058$ ).

4. We found that under effects of the river flow and the mild bottom slope or the gradual contraction of the width, the two-layer flows at the salt tip exist as the density currents with the hydraulic jump at the head, similar to the density currents observed in previous researches (e.g., Benjamin, 1968; Baines, 1995). The effects of the above geometric features and the development of the hydraulic jump are as follow:

(i) In the contraction of the width or the bottom slope, the size of the fresh flow and the salt flow should be changed. Especially, the river flow seems to be strengthen by the increase in the momentum flux. River flow and the bottom slope or the contraction induce the friction at the interface of the flow and the presence time of two-layer flow as the density current at the salt tip. The presence time of the density currents for a tidal cycle in the mild slope or the gradual contraction are at least six times larger than that in the non-geometry effects.

(ii) The results observation of the momentum fluxes at salt layer for the pressure components ( $Mf_{2p}$ ) and the kinetic components ( $Mf_{2u}$ ) show that the energy is converged in mass and velocity at head of the salinity flow during the propagating time of the salt flow in the sheared environmental fresh flow. From the convergence of the energy, the state flow at the front of the head of the density current turn to supper critical ( $Fr_f > 1$ ) and then the energy from the lower layer (salt water layer) be dissipated to the upper layer (freshwater layer) as a hydraulic jump. The internal bore along with the intensive mixing are therefore generated.

## **7.2 Recommendations**

The present research applied the modelling method to study the hydrodynamic and sedimentary processes of the estuary in the ideal conditions. Studying for the ideal conditions will eliminate the confounding effects and make the obtained conclusions very clear to be observed, but this method leads results may be out of reality. In fact, beside the geometric features, the development of the density front and the vertical mixing are affected by other processes such as the wind, the cohesion of the sediment or the complex change in the bottom roughness, etc. Therefore, we recommend further study include the above effects in the research.



## References

- Allen, G.P., Salomon, J.C., Bassoullet, P., Du Penhoat, Y. and De Grandpre, C., 1980. Effects of tides on mixing and suspended sediment transport in macrotidal estuaries. *Sediment transport Geology*, 26(1-3), pp.69-90.
- Arita, M., & Jirka, G. H. (1987). Two-layer model of saline wedge. I: Entrainment and interfacial friction. *Journal of Hydraulic Engineering*, 113(10), 1229-1246.
- Armi, L. and Farmer, D.M., 1986. Maximal two-layer exchange through a contraction with barotropic net flow. *Journal of Fluid Mechanics*, 164, pp.27-51.
- Armi, L., 1986. The hydraulics of two flowing layers with different densities. *Journal of Fluid Mechanics*, 163, pp.27-58.
- Baines, P.G., 1997. *Topographic effects in stratified flows*. Cambridge university press.
- Bartsch-Winkler, S. and Lynch, D.K., 1988. *Catalog of worldwide tidal bore occurrences and characteristics (Vol. 1022)*. US Government Printing Office.
- Benjamin, T.B., 1968. Gravity currents and related phenomena. *Journal of Fluid Mechanics*, 31(2), pp.209-248.
- Boegman, L. and Ivey, G.N., 2009. Flow separation and resuspension beneath shoaling nonlinear internal waves. *Journal of Geophysical Research: Oceans*, 114(C2).
- Bonnin, J., Van Haren, H., Hosegood, P. and Brummer, G.J.A., 2006. Burst resuspension of seabed material at the foot of the continental slope in the Rockall Channel. *Marine Geology*, 226(3-4), pp.167-184.
- Bormans, M. and Garrett, C., 1989. The effects of nonrectangular cross section, friction, and barotropic fluctuations on the exchange through the Strait of Gibraltar. *Journal of Physical Oceanography*, 19(10), pp.1543-1557.

- Broenkow, W.W. and McKain, S.J., 1972. Tidal oscillations at the head of Monterey Submarine Canyon and their relation to oceanographic sampling and the circulation of water in Monterey Bay. Annual report, Part 6, September 1972.
- Burchard, H. and Hetland, R.D., 2010. Quantifying the contributions of tidal straining and gravitational circulation to residual circulation in periodically stratified tidal estuaries. *Journal of Physical Oceanography*, 40(6), pp.1243-1262.
- Burchard, H. and Hofmeister, R., 2008. A dynamic equation for the potential energy anomaly for analysing mixing and stratification in estuaries and coastal seas. *Estuarine, coastal and shelf science*, 77(4), pp.679-687.
- Burchard, H., & Schuttelaars, H. M. (2012). Analysis of tidal straining as driver for estuarine circulation in well-mixed estuaries. *Journal of physical oceanography*, 42(2), 261-271.
- Burchard, H., Schuttelaars, H.M. and Ralston, D.K., 2018. Sediment trapping in estuaries. *Annual review of marine science*, 10, pp.371-395.
- Burchard, H., Schuttelaars, H.M. and Ralston, D.K., 2018. Sediment trapping in estuaries. *Annual review of marine science*, 10, pp.371-395.
- Cacchione, D.A., Pratson, L.F. and Ogston, A.S., 2002. The shaping of continental slopes by internal tides. *Science*, 296(5568), pp.724-727.
- Carter, G.S., Gregg, M.C. and Lien, R.C., 2005. Internal waves, solitary-like waves, and mixing on the Monterey Bay shelf. *Continental Shelf Research*, 25(12-13), pp.1499-1520.
- Chanson, H. (2010). Undular tidal bores: basic theory and free-surface characteristics. *Journal of Hydraulic Engineering*, 136(11), 940-944.
- Chanson, H., 2004. *Hydraulics of open channel flow*. Elsevier.
- Chanson, H., 2012. Tidal bores, aegir, eagre, mascaret, pororoca: Theory and observations. World Scientific.
- Chaudhry, M.H., 2007. *Open-channel flow*. Springer Science & Business Media.

- Chua, V.P. and Fringer, O.B., 2011. Sensitivity analysis of three-dimensional salinity simulations in North San Francisco Bay using the unstructured-grid SUNTANS model. *Ocean Modelling*, 39(3-4), pp.332-350.
- CIMAS (The Cooperative Institute for Marine and Atmospheric Studies)  
**Ocean surface currents, glossary (2001–2008)**  
<http://oceancurrents.rsmas.miami.edu/glossary.html> (2012), Accessed September 2, 2012
- de Nijs, M.A., Winterwerp, J.C. and Pietrzak, J.D., 2010. The effects of the internal flow structure on SPM entrapment in the Rotterdam Waterway. *Journal of Physical Oceanography*, 40(11), pp.2357-2380.
- Doxaran, D., Froidefond, J.M., Castaing, P. and Babin, M., 2009. Dynamics of the turbidity maximum zone in a macrotidal estuary (the Gironde, France): Observations from field and MODIS satellite data. *Estuarine, Coastal and Shelf Science*, 81(3), pp.321-332.
- Farmer, D.M. and Denton, R.A., 1985. Hydraulic control of flow over the sill in Observatory Inlet. *Journal of Geophysical Research: Oceans*, 90(C5), pp.9051-9068.
- Farmer, D.M. and Denton, R.A., 1985. Hydraulic control of flow over the sill in Observatory Inlet. *Journal of Geophysical Research: Oceans*, 90(C5), pp.9051-9068.
- Ferziger, J.H., Perić, M. and Street, R.L., 2002. Computational methods for fluid dynamics (Vol. 3, pp. 196-200). Berlin: springer.
- Fischer, H.B., List, J.E., Koh, C.R., Imberger, J. and Brooks, N.H., 2013. *Mixing in inland and coastal waters*. Elsevier.
- Friedrichs, C.T. and Wright, L.D., 1995. Resonant internal waves and their role in transport and accumulation of fine sediment in Eckernförde Bay, Baltic Sea. *Continental Shelf Research*, 15(13), pp.1697-1721.

- Fringer, O.B., Gerritsen, M. and Street, R.L., 2006. An unstructured-grid, finite-volume, nonhydrostatic, parallel coastal ocean simulator. *Ocean modelling*, 14(3-4), pp.139-173.
- Fugate, D.C. and Friedrichs, C.T., 2002. Determining concentration and fall velocity of estuarine particle populations using ADV, OBS and LISST. *Continental Shelf Research*, 22(11-13), pp.1867-1886.
- Gerdes, F., Garrett, C., & Farmer, D. (2002). On internal hydraulics with entrainment. *Journal of physical oceanography*, 32(3), 1106-1111.
- Gerrity Jr, J. P., Black, T. L., & Treadon, R. E. (1994). The numerical solution of the Mellor-Yamada level 2.5 turbulent kinetic energy equation in the Eta model. *Monthly weather review*, 122(7), 1640-1646.
- Geyer, W.R. and MacCready, P., 2014. The estuarine circulation. *Annual review of fluid mechanics*, 46, pp.175-197.
- Geyer, W.R. and Ralston, D.K., 2015. Estuarine frontogenesis. *Journal of Physical Oceanography*, 45(2), pp.546-561.
- Geyer, W.R. and Ralston, D.K., 2015. Estuarine frontogenesis. *Journal of Physical Oceanography*, 45(2), pp.546-561.
- Geyer, W.R., 1993. The importance of suppression of turbulence by stratification on the estuarine turbidity maximum. *Estuaries*, 16(1), pp.113-125.
- Geyer, W.R., Trowbridge, J.H. and Bowen, M.M., 2000. The dynamics of a partially mixed estuary. *Journal of Physical Oceanography*, 30(8), pp.2035-2048.
- Geyer, W.R., Woodruff, J.D. and Traykovski, P., 2001. Sediment transport and trapping in the Hudson River estuary. *Estuaries*, 24(5), pp.670-679.
- Giddings, S. N., Fong, D. A., & Monismith, S. G. (2011). Role of straining and advection in the intratidal evolution of stratification, vertical mixing, and longitudinal dispersion of a shallow, macrotidal, salt wedge estuary. *Journal of Geophysical Research: Oceans*, 116(C3).

- Gill, M. A. (1980). Effect of boundary roughness on hydraulic jump. *Water Power & Dam Construction*, 32, 22-24.
- Griffies, S.M. and Hallberg, R.W., 2000. Biharmonic friction with a Smagorinsky-like viscosity for use in large-scale eddy-permitting ocean models. *Monthly Weather Review*, 128(8), pp.2935-2946.
- Hager, Willi H. *Energy dissipators and hydraulic jump*. Vol. 8. Springer Science & Business Media, 2013.
- Hamblin, P.F., 1989. Observations and model of sediment transport near the turbidity maximum of the Upper Saint Lawrence Estuary. *Journal of Geophysical Research: Oceans*, 94(C10), pp.14419-14428.
- Hazel, P. (1972). Numerical studies of the stability of inviscid stratified shear flows. *Journal of Fluid Mechanics*, 51(1), 39-61.
- Helfrich, K.R., 1992. Internal solitary wave breaking and run-up on a uniform slope. *Journal of Fluid Mechanics*, 243, pp.133-154.
- Henderson, F.M., 1966. Open channel flow (No. 532 H4).
- Holleman, R., Fringer, O. and Stacey, M., 2013. Numerical diffusion for flow-aligned unstructured grids with application to estuarine modeling. *International Journal for Numerical Methods in Fluids*, 72(11), pp.1117-1145.
- Hosegood, P., Bonnin, J., & van Haren, H. (2004). Solibore-induced sediment resuspension in the Faeroe-Shetland Channel. *Geophysical Research Letters*, 31(9).
- Huijts, K.M.H., Schuttelaars, H.M., De Swart, H.E. and Valle-Levinson, A., 2006. Lateral entrainment of sediment in tidal estuaries: An idealized model study. *Journal of Geophysical Research: Oceans*, 111(C12).
- Huppert, H.E. and Simpson, J.E., 1980. The slumping of gravity currents. *Journal of Fluid Mechanics*, 99(4), pp.785-799.

- Jay, D.A. and Musiak, J.D., 1994. Particle trapping in estuarine tidal flows. *Journal of Geophysical Research: Oceans*, 99(C10), pp.20445-20461.
- Jay, D.A. and Musiak, J.D., 1996. Internal tidal asymmetry in channel flows: Origins and consequences. *Coastal and Estuarine Studies*, pp.211-249.
- Jay, D.A., 1991. Internal asymmetry and anharmonicity in estuarine flows. *Progress in tidal hydrodynamics*, pp.521-543.
- Kim, N. H., Hwang, J. H., & Hyeon, K. D. (2018). Evaluation of Mixing and Stratification in an Estuary of Korea. *Journal of Coastal Research*, 85(sp1), 96-100.
- Kirby, R. and Parker, W.R., 1982. A suspended sediment front in the Severn Estuary. *Nature*, 295(5848), pp.396-399.
- Klymak, J. M., & Gregg, M. C. (2001). Three-dimensional nature of flow near a sill. *Journal of Geophysical Research: Oceans*, 106(C10), 22295-22311.
- Klymak, J. M., Moum, J. N., Nash, J. D., Kunze, E., Giron, J. B., Carter, G. S., ... & Gregg, M. C. (2006). An estimate of tidal energy lost to turbulence at the Hawaiian Ridge. *Journal of Physical Oceanography*, 36(6), 1148-1164.
- Klymak, J. M., Pinkel, R., & Rainville, L. (2008). Direct breaking of the internal tide near topography: Kaena Ridge, Hawaii. *Journal of Physical Oceanography*, 38(2), 380-399.
- Klymak, J.M. and Moum, J.N., 2003. Internal solitary waves of elevation advancing on a shoaling shelf. *Geophysical Research Letters*, 30(20).
- Koch, C., & Chanson, H. (2008). Turbulent mixing beneath an undular bore front. *Journal of Coastal Research*, 999-1007.
- Lamb, K.G., 1997. Particle transport by nonbreaking, solitary internal waves. *Journal of Geophysical Research: Oceans*, 102(C8), pp.18641-18660.
- Lang, G., Schubert, R., Markofsky, M., Fanger, H.U., Grabemann, I., Krasemann, H.L., Neumann, L.J.R. and Riethmüller, R., 1989. Data interpretation and

- numerical modeling of the mud and suspended sediment experiment 1985. *Journal of Geophysical Research: Oceans*, 94(C10), pp.14381-14393.
- Lean, G.H. and Whillock, A.Z., 1965. The behaviour of a warm water layer flowing over still water. In *Proc. 11th Congress Int. Assoc. of Hydr. Res* (Vol. 2, pp. 1-2).
- Ledwell, J. R., Montgomery, E. T., Polzin, K. L., Laurent, L. S., Schmitt, R. W., & Toole, J. M. (2000). Evidence for enhanced mixing over rough topography in the abyssal ocean. *Nature*, 403(6766), 179-182.
- Lee, W.D., Mizutani, N. and Hur, D.S., 2018. Behavior Characteristics of Density Currents Due to Salinity Differences in a 2-D Water Tank. *Journal of Ocean Engineering and Technology*, 32(4), pp.261-271.
- Li, Y., Pan, D.Z., Chanson, H. and Pan, C.H., 2019. Real-time characteristics of tidal bore propagation in the Qiantang River Estuary, China, recorded by marine radar. *Continental Shelf Research*, 180, pp.48-58.
- Lubin, P. and Chanson, H., 2017. Are breaking waves, bores, surges and jumps the same flow?. *Environmental Fluid Mechanics*, 17(1), pp.47-77.
- Lubin, P., & Chanson, H. (2017). Are breaking waves, bores, surges and jumps the same flow?. *Environmental Fluid Mechanics*, 17(1), 47-77.
- Lucas, L.V., Cloern, J.E., Koseff, J.R., Monismith, S.G. and Thompson, J.K., 1998. Does the Sverdrup critical depth model explain bloom dynamics in estuaries?. *Journal of Marine Research*, 56(2), pp.375-415.
- MacDonald, D.G. and Geyer, W.R., 2005. Hydraulic control of a highly stratified estuarine front. *Journal of physical oceanography*, 35(3), pp.374-387.
- Masunaga, E., Arthur, R.S., Fringer, O.B. and Yamazaki, H., 2017. Sediment resuspension and the generation of intermediate nepheloid layers by shoaling internal bores. *Journal of Marine Systems*, 170, pp.31-41.
- Masunaga, E., Homma, H., Yamazaki, H., Fringer, O.B., Nagai, T., Kitade, Y. and Okayasu, A., 2015. Mixing and sediment resuspension associated with

- internal bores in a shallow bay. *Continental Shelf Research*, 110, pp.85-99.
- Mauritsen, T., Svensson, G., Zilitinkevich, S. S., Esau, I., Enger, L., & Grisogono, B. (2007). A total turbulent energy closure model for neutrally and stably stratified atmospheric boundary layers. *Journal of the atmospheric sciences*, 64(11), 4113-4126.
- Mellor, G.L. and Yamada, T., 1982. Development of a turbulence closure model for geophysical fluid problems. *Reviews of Geophysics*, 20(4), pp.851-875.
- Miles, J.W. and Howard, L.N., 1964. Note on a heterogeneous shear flow. *Journal of Fluid Mechanics*, 20(2), pp.331-336.
- Mohamed Ali, H. S. (1991). Effect of roughened-bed stilling basin on length of rectangular hydraulic jump. *Journal of Hydraulic Engineering*, 117(1), 83-93.
- Nash, J.D. and Moum, J.N., 2005. River plumes as a source of large-amplitude internal waves in the coastal ocean. *Nature*, 437(7057), pp.400-403.
- Nashta, C.F. and Garde, R.J., 1988. Subcritical flow in rigid-bed open channel expansions. *Journal of hydraulic research*, 26(1), pp.49-65.
- Nidzieko, N.J., 2010. Tidal asymmetry in estuaries with mixed semidiurnal/diurnal tides. *Journal of Geophysical Research: Oceans*, 115(C8).
- North, E.W. and Houde, E.D., 2001. Retention of white perch and striped bass larvae: biological-physical interactions in Chesapeake Bay estuarine turbidity maximum. *Estuaries*, 24(5), pp.756-769.
- North, E.W., Chao, S.Y., Sanford, L.P. and Hood, R.R., 2004. The influence of wind and river pulses on an estuarine turbidity maximum: Numerical studies and field observations in Chesapeake Bay. *Estuaries*, 27(1), pp.132-146.



- Park, K., Wang, H.V., Kim, S.C. and Oh, J.H., 2008. A model study of the estuarine turbidity maximum along the main channel of the upper Chesapeake Bay. *Estuaries and Coasts*, 31(1), pp.115-133.
- Peregrine, D. H., & Svendsen, I. A. (1978). Spilling breakers, bores, and hydraulic jumps. In *Coastal Engineering 1978* (pp. 540-550).
- Perot, B., 2000. Conservation properties of unstructured staggered mesh schemes. *Journal of Computational Physics*, 159(1), pp.58-89.
- Petruncio, E.T., Rosenfeld, L.K. and Paduan, J.D., 1998. Observations of the internal tide in Monterey Canyon. *Journal of Physical Oceanography*, 28(10), pp.1873-1903.
- Polzin, K. L., & Firing, E. (1997). Estimates of diapycnal mixing using LADCP and CTD data from I8S. *International WOCE Newsletter*, 29, 39-42.
- Polzin, K. L., Toole, J. M., Ledwell, J. R., & Schmitt, R. W. (1997). Spatial variability of turbulent mixing in the abyssal ocean. *Science*, 276(5309), 93-96.
- Postma, H., 1967. Sediment transport and sedimentation in the estuarine environment. *American Association of Advanced Sciences*, 83, pp.158-179.
- Rajaratnam, N. (1968). Hydraulic jumps on rough beds. *Trans. Eng. Inst. Canada*, 11(A-2), 1-8.
- Ralston, D.K., Geyer, W.R. and Warner, J.C., 2012. Bathymetric controls on sediment transport in the Hudson River estuary: Lateral asymmetry and frontal trapping. *Journal of Geophysical Research: Oceans*, 117(C10).
- Richards, C., Bourgault, D., Galbraith, P. S., Hay, A., & Kelley, D. E. (2013). Measurements of shoaling internal waves and turbulence in an estuary. *Journal of Geophysical Research: Oceans*, 118(1), 273-286.
- Rippeth, T.P., Fisher, N.R. and Simpson, J.H., 2001. The cycle of turbulent dissipation in the presence of tidal straining. *Journal of Physical Oceanography*, 31(8), pp.2458-2471.

- Sanford, L.P., Suttles, S.E. and Halka, J.P., 2001. Reconsidering the physics of the Chesapeake Bay estuarine turbidity maximum. *Estuaries*, 24(5), pp.655-669.
- Savenije, H.H., 2005. Salinity and tides in alluvial estuaries. Gulf Professional Publishing.
- Schmidt, W., 1911. Zur mechanik der boen. *Z. Meteorol*, 28, pp.355-362.
- Scully, M.E. and Friedrichs, C.T., 2003. The influence of asymmetries in overlying stratification on near-bed turbulence and sediment suspension in a partially mixed estuary. *Ocean Dynamics*, 53(3), pp.208-219.
- Scully, M.E. and Friedrichs, C.T., 2003. The influence of asymmetries in overlying stratification on near-bed turbulence and sediment suspension in a partially mixed estuary. *Ocean Dynamics*, 53(3), pp.208-219.
- Scully, M.E. and Friedrichs, C.T., 2007. Sediment pumping by tidal asymmetry in a partially mixed estuary. *Journal of Geophysical Research: Oceans*, 112(C7).
- Simpson, J.E. and Linden, P.F., 1989. Frontogenesis in a fluid with horizontal density gradients. *Journal of Fluid Mechanics*, 202, pp.1-16.
- Simpson, J.E., 1982. Gravity currents in the laboratory, atmosphere, and ocean. *Annual Review of Fluid Mechanics*, 14(1), pp.213-234.
- Simpson, J.H., Brown, J., Matthews, J. and Allen, G., 1990. Tidal straining, density currents, and stirring in the control of estuarine stratification. *Estuaries*, 13(2), pp.125-132.
- Simpson, J.H., Williams, E., Brasseur, L.H. and Brubaker, J.M., 2005. The impact of tidal straining on the cycle of turbulence in a partially stratified estuary. *Continental Shelf Research*, 25(1), pp.51-64.
- Sommerfield, C.K. and Wong, K.C., 2011. Mechanisms of sediment flux and turbidity maintenance in the Delaware Estuary. *Journal of Geophysical Research: Oceans*, 116(C1).

- Spitz, Y.H. and Klinck, J.M., 1998. Estimate of bottom and surface stress during a spring-neap tide cycle by dynamical assimilation of tide gauge observations in the Chesapeake Bay. *Journal of Geophysical Research: Oceans*, 103(C6), pp.12761-12782.
- Staalstrøm, A., Arneborg, L., Liljebladh, B., & Broström, G. (2015). Observations of turbulence caused by a combination of tides and mean baroclinic flow over a fjord sill. *Journal of Physical Oceanography*, 45(2), 355-368.
- Stacey, M.T., Monismith, S.G. and Burau, J.R., 1999. Observations of turbulence in a partially stratified estuary. *Journal of Physical Oceanography*, 29(8), pp.1950-1970.
- Thompson, D.M., Wohl, E.E. and Jarrett, R.D., 1999. Velocity reversals and sediment sorting in pools and riffles controlled by channel constrictions. *Geomorphology*, 27(3-4), pp.229-241.
- Umeyama, M. and Shintani, T., 2006. Transformation, attenuation, setup, and undertow of internal waves on a gentle slope. *Journal of waterway, port, coastal, and ocean engineering*, 132(6), pp.477-486.
- Uncles, R.J., Stephens, J.A. and Law, D.J., 2006. Turbidity maximum in the macrotidal, highly turbid Humber Estuary, UK: Floccs, fluid mud, stationary suspensions and tidal bores. *Estuarine, Coastal and Shelf Science*, 67(1-2), pp.30-52.
- Valle-Levinson, A., 1995. Observations of barotropic and baroclinic exchanges in the lower Chesapeake Bay. *Continental Shelf Research*, 15(13), pp.1631-1647.
- van Haren, H., 2009. Using high sampling-rate ADCP for observing vigorous processes above sloping [deep] ocean bottoms. *Journal of Marine Systems*, 77(4), pp.418-427.
- Van Rijn, L.C., 1993. Principles of sediment transport in rivers, estuaries and coastal seas (Vol. 1006, pp. 11-3). Amsterdam: Aqua publications.

- Venayagamoorthy, S. K., & Fringer, O. B. (2006). Numerical simulations of the interaction of internal waves with a shelf break. *Physics of Fluids*, 18(7), 076603.
- Viero, D.P. and Defina, A., 2018. Consideration of the mechanisms for tidal bore formation in an idealized planform geometry. *Water Resources Research*, 54(8), pp.5670-5686.
- Wallace, B.C. and Wilkinson, D.L., 1988. Run-up of internal waves on a gentle slope in a two-layered system. *Journal of Fluid Mechanics*, 191, pp.419-442.
- Walter, R.K., Woodson, C.B., Arthur, R.S., Fringer, O.B. and Monismith, S.G., 2012. Nearshore internal bores and turbulent mixing in southern Monterey Bay. *Journal of Geophysical Research: Oceans*, 117(C7).
- Wang, B., Fringer, O.B., Giddings, S.N. and Fong, D.A., 2009. High-resolution simulations of a macrotidal estuary using SUNTANS. *Ocean Modelling*, 28(1-3), pp.167-192.
- Wang, B., Giddings, S.N., Fringer, O.B., Gross, E.S., Fong, D.A. and Monismith, S.G., 2011. Modeling and understanding turbulent mixing in a macrotidal salt wedge estuary. *Journal of Geophysical Research: Oceans*, 116(C2).
- Wang, Y.H., Lee, I.H. and Liu, J.T., 2008. Observation of internal tidal currents in the Kaoping Canyon off southwestern Taiwan. *Estuarine, Coastal and Shelf Science*, 80(1), pp.153-160.
- West, J. R., & Oduyemi, K. O. K. (1989). Turbulence measurements of suspended solids concentration in estuaries. *Journal of Hydraulic Engineering*, 115(4), 457-474.
- West, J. R., & Shiono, K. (1985). A note on turbulent perturbations of salinity in a partially mixed estuary. *Estuarine, Coastal and Shelf Science*, 20(1), 55-78.
- Xu, Q. and Moncrieff, M.W., 1994. Density current circulations in shear flows. *Journal of the atmospheric sciences*, 51(3), pp.434-446.

- Yu, Q., Wang, Y., Gao, J., Gao, S. and Flemming, B., 2014. Turbidity maximum formation in a well-mixed macrotidal estuary: The role of tidal pumping. *Journal of Geophysical Research: Oceans*, 119(11), pp.7705-7724.
- Zhang, Z., Fringer, O.B. and Ramp, S.R., 2011. Three-dimensional, nonhydrostatic numerical simulation of nonlinear internal wave generation and propagation in the South China Sea. *Journal of Geophysical Research: Oceans*, 116(C5).
- Zhu, D.Z. and Lawrence, G.A., 2000. Hydraulics of exchange flows. *Journal of Hydraulic Engineering*, 126(12), pp.921-928.

## ABSTRACT IN KOREAN

### 다양한 하구 지형 영향에 따른 salt tip에서의 역전과 혼합에 대한 연구

유사를 포함한 밀도류는 염수썰기 끝단에서 하상 경사와 하폭이 심하게 변하는 등 지형이 급격하게 변화하는 곳 인근에서 자주 관찰된다. 그러나 지금까지 이러한 지형변화에 의해서 유사를 포함한 퇴적물의 거동에 대한 연구가 많이 수행되지 않았다. 반면에 급격하게 경사가 변하는 해안지역에서는 내부파 혹은 내부 조석의 처오름 현상에 의해서 밀도의 위아래가 부분적으로 뒤집히는 현상을 만들고 이것이 유사의 수직 혼합과 재부유를 야기시키는 것을 발견하였다. 특히 Masunaga et al. (2015)가 연안에서 관측한 내부파에 의한 자연현상은 밀도, 흐름을 함께 비교한 Froude 수의 결과로 볼 때 밀도류의 수력도약으로 볼 수 있다. 따라서 본 연구의 주요 목표는 하구 연구에 있어 지형적 효과에 대해 이해하고, 특히 흐름에서 도수발생으로 인하여 역전현상이 진행되는 과정에 대해 이해하고자 한다. 이에 대해서 바닥 경사가 완만하게 하상 경사가 변하는 지형과 폭이 점진적으로 수축하는 두 가지 지형에 대해서 연구를 수행하였다.

본 연구는 전술한 대로 유사이동의 수송과정 이전에 먼저 염수와 담수의 혼합 이송과정에 대해서 수치적 실험을 수행하였다. 도출된 결과는 성층과 유사 이동의 과정을 좀 더 상세하게 파악하기 위해서 Richardson 수, 난류 소산율등을 이용하였다. 또한 모멘텀 해석법과 Froude 수를 이용하여 지형적 변화가 도수 발생에 미치는 영향을 좀 더 상세하게 파악하고자 하였다.

결론적으로 완만한 경사가 있는 경우에도 충분히 염수 빼기의 전단부에서 밀도역전현상이 발생할 수 있고, 지형이 수축되는 경우에도 상당히 오래 유지되는 것을 알 수 있었다. 이로 인해서 이 위치에서는 강한 수직혼합이 발생하며 유사도 재부유가 크게 발생하게 된다. 이것은 역학적으로 볼 때는 내부 수력 도약 혹은 도수로 인해 역전현상과 강한 전단을 갖는 밀도류가 발생하게 되는 것을 알 수 있었다.

키워드: 염수빼기, 완만한 경사, 하폭 축소, 내부 수력도약, 도수, 성층과 혼합

## ACKNOWLEDGEMENT

First and foremost, I would like to express my heartfelt gratitude and appreciation for my advisor Professor Jin Hwan Hwang who accepted and gave me a chance to study in Korea. Thank you very much for your patience, motivation, enthusiasm and immense knowledge. My professor has patiently taught me a lot of skills related to the study. Without your support and patience, I could not finish my study.

I wish to express my sincere thanks to my dissertation committee, including Professor Yong Sung Park, Professor Ho Kyung Ha, Professor Jungkyu Ahn and Professor Yong Hoon Kim for valuable comments and suggestions.

My sincere thanks also go to my lab members at Flow Physics and Informatics Laboratory: Seogeun Choi, Donghyeon Kim, Jaeyoung Jung, Houyng-Chul Park, Jisu Kim, Bokyoung Kim, Nam-Hoon Kim, Pham Van Sy and the other members. Thank you very much for your precious time, for the kindness and the enthusiastic support, especially the works related to the Korean language. I will cherish your supports forever.

Many thanks to my Vietnamese friends: Nguyen Thi Hong Ha, Nguyen Thanh Chuyen, Tran Xuan Nghiem and other Vietnamese students in SNU for the invaluable assistance that you all provided during my study, for chatting with me. Special thanks to Tran Quoc Viet for his valuable and promptly support on the problems relative to SUNTANS and for the comments on directly numerical model.

Finally, thank you very much to my husband for his patience, supports and quiet sacrifices. Thank you for loving me unconditionally.